UNIVERSITÀ DEGLI STUDI DI PADOVA

Dipartimento di Fisica e Astronomia "Galileo Galilei"

Master Degree in Astrophysics and Cosmology

Final Dissertation

Low surface-brightness galaxy population in the Centaurus cluster from the VEGAS survey

Supervisor

Prof. Enrico Maria Corsini

Co-supervisor

Dr. Enrichetta Iodice

Student

Nicola Bellucco

Accademic year 2021/22

Contents

Abstract

Low surface-brightness (LSB) dwarf galaxies in galaxy clusters are an interesting class of objects as their contribution to the galaxy luminosity function and their evolutionary paths are not yet clear. A subgroup of dwarf LSB galaxies called ultra-diffuse galaxies (UDGs) has been studied in several environments because their formation scenarios and dark matter content are still poorly constrained. The study of LSB galaxies allows to test the galaxy formation theories in a so far unexplored and unique parameter space. It also allows to test gravity models because LSB galaxies have the lowest stellar mass content and are strongly affected by tidal forces. In addition, a complete census of LSB galaxies is needed to test cosmological models and, in particular, to investigate the missing satellite problem.

I aimed at detecting the LSB galaxies and UDGs of Centaurus cluster using wide-field deep-imaging data from the VST Early-type Galaxy Survey (VEGAS), to study how their scaling relations interface with the current formation scenarios from cosmological hydrodynamical simulations.

I applied straightforward and easily installable tools to develop a semi-automatic algorithm for the detection of LSB galaxies in the g'-band image of the inner 1.4×1.6 deg^2 (1 Mpc^2) region of the Centaurus cluster centered on NGC 4696. I identified 136 LSB galaxies measuring their surface brightness radial profile at $\mu_g \lesssim 30$ mag arcsec^{-2}, five of them are UDGs.

I fitted their surface brightness distribution and performed the isophotal analysis. Finally, I circularized the isophotes to obtain the radial surface-brightness profiles that I fitted with a 1D-Sérsic model to obtain the structural parameters of the sample LSB galaxies. I find that the sample LSB galaxies are on average redder than dwarf elliptical galaxies and have a comparable slope of the color-magnitude relation. The Kormedy relation is valid in the LSB regime too. The correlations between cluster-centric distance and surface brightnesses are in favour of an ex-situ formation of LSB galaxies, whereas the number of UDGs, which is in agreement with the UDG abundance-halo mass relation, is in favour of the in-situ formation scenario.

Chapter 1

Introduction

In this chapter I introduce the low surface-brightness dwarf galaxies and I give an overview of their properties, formation scenarios, and importance in the broader context of our knowledge of the mass assembly process of the universe in Sec. 1.1. Then, I describe the ultra-diffuse galaxies in Sec. 1.2. Finally, I summarise the aims of this thesis and the content of its chapters in Sec. 1.3.

1.1 Low surface brightness galaxies

The low surface-brightness (LSB) dwarf galaxies are an interesting class of objects, as their contribution to the galaxy luminosity function and evolutionary path are not yet clear (Pérez-Montaño et al. 2022). The LSB galaxies have a central surface brightness $\mu_{g,0} > 23$ mag arcsec^{-2}. The existence of LSB galaxies was first speculated by Disney (1976) and the first catalog of LSB galaxies came from the study of Palomar photographic plates by Schombert & Bothun (1988).

These galaxies, having an extremely diffuse structure and existing in dense environments, allow to test the galaxy formation theories in a so far unexplored and unique parameter space (e.g., Pérez-Montaño et al. 2022). Ultimately, addressing the number and properties of LSB galaxies will allow to probe their formation mechanisms and to have a benchmark for cosmological models. In particular, the Λ Cold Dark Matter (ΛCDM) model predicts that a large number of low mass DM halos should populate the outskirts of giant galaxies. The baryons associated with these small DM halos should be detected as dwarf galaxies. In the past twenty years astronomers tried without success to fill the gap between the predicted and observed abundance of low-mass dwarf galaxies, (e.g., Müller & Jerjen 2020). This issue is known as the "missing satellites" problem.

Hence, a complete census and in-depth study of LSB galaxies is needed to understand if the missing satellite issue is either due to a detection threshold due to our limited depth or a main problem of the ΛCDM. In order to have a complete census of LSB galaxies, it is fundamental to develop automated softwares specifically designed for such extreme surface brightnesses. Some pivotal trials to perform automatic detection and analysis of LSB galaxies with high detection efficiency have been performed in the last five years (e.g., Venhola et al. 2022; Yi et al. 2022).

Moreover, the deployment of wide-field imaging facilities with large collecting areas has improved our ability to study LSB galaxies. Several deep surveys, such as the Next Generation Virgo Survey (NGVS; Ferrarese et al. 2012), the Kilo Degree Survey (KiDS; de Jong et al. 2013), VST Early-type Galaxy Survey (VEGAS; Capaccioli et al. 2015), and the Fornax Deep Survey (FDS; Iodice et al. 2016) have gathered large amounts of data and revealed previously unseen LSB galaxies (Muñoz et al. 2015; Koda et al. 2015; van der Burg et al. 2016; La Marca et al. 2022b; Venhola et al. 2022).

In addition, the new imaging facilities, such as the Large Synoptic Survey Telescope (LSST; Ivezić et al. 2019) and Euclid (Laureijs et al. 2012), will provide a huge amount of data products making the LSB regime even more easily accessible. On the other hand, up to date we do not have the softwares to deal with such an expected overwhelming quantity of data.

Exploring the LSB universe to map the mass assembly of galaxies in all environments is one of the most challenging tasks in modern astrophysical research. So far, we have not reached any lower limit in surface brightness where we stop finding new galaxies (e.g., Fattahi et al. 2020), hence there is still a possibility to solve the missing satellite problem increasing our depth. In addition to not knowing how many galaxies we fail to detect, spectroscopy cannot reach similar depths as effectively as imaging. The confirmation of galaxy cluster membership by radial velocities is challenging due to the LSB nature of the targets. In addition, the contribution of the LSB galaxies to the luminosity function and their properties are in general not well known. The LSB galaxies do not share the same morphology, suggesting they are not a unique class of objects with the same formation channel. Many formation scenarios have been proposed for LSB galaxies. They include internal processes such as stellar feedback and external processes, in particular ram-pressure stripping (RPS), harassment and tidal heating (Pérez-Montaño et al. 2022). The external processes are expected to be the main channel for the formation of LSB galaxies in clusters. Nevertheless, a fraction of LSB galaxies found in clusters could have been formed in less dense environments and successively infallen into the cluster.

Encounters are the main process that changes the morphology of galaxies in clusters. If an encounter happens with sufficiently low velocity, then the galaxies merge. The merging of two galaxies of similar masses is called major merger, whereas it is a minor merger if the masses have a different order of magnitude. If the encounter happens with sufficiently high velocity the resulting process is called harassment. Harassment quenches the star formation (Moore et al. 1998; Mastropietro et al. 2005) and only partially removes the stars from galaxy outskirts (Smith et al. 2015), increasing the concentration index of the galaxy. Moreover, harassment can dynamically heat up the stellar population of a galaxy changing its morphology from late into early types (Mastropietro et al. 2005). Another drastic consequence of galaxy encounters is the threshing: tidal forces can be so strong that the dwarf galaxies are disrupted (Koch et al. 2012). Galaxy threshing has been invoked for the formation of small satellite galaxies, such as the ultra-compact dwarf galaxies (Drinkwater et al. 2003), as the denser remnants of tidal disrupted dwarf galaxies. RPS is a process affecting the interstellar matter in galaxies: when a galaxy falls into a cluster of galaxies, its cold gas component interacts with the hot gas of the cluster and the pressure between the two gas components removes the cold gas from the galaxy potential well (Gunn & Gott 1972). The effect is called partial RPS if the galaxy is massive enough to retain part of its gas. The partial RPS has been invoked to explain the existence of red LSB galaxies with blue centers (Lisker et al. 2006; Hamraz et al. 2019). Both RPS and harassment cause the quenching of star formation. After that, the color evolution of the galaxy follows that of the preexisting stellar population becoming redder with age.

Thus encounters change galaxy morphology and their effect is enhanced in high-density environments where the encounter timescale is smaller. The morphology-density relation (Dressler 1980) was firstly discovered for early type galaxies (ETGs). The main processes involved in the transformation of galaxies from blue star-forming late-type galaxies (LTGs) to red quiescent ETGs in clusters are RPS and galaxy harassment. LSB dwarf galaxies follow the morphology-density relation too, such that the red LSB dwarf galaxies are mostly found in dense environments and blue LSB dwarf galaxies in sparse ones (e.g., Román & Trujillo 2017b). LSB dwarf galaxies could form from dwarf galaxies with high surface-brightness affected by RPS and harassment during their infall into the cluster (Tremmel et al. 2020). This process also leads to the surface brightness-age relation predicted by simulations (Tremmel et al. 2020) according to which higher surface-brightness dwarf galaxies are younger. In addition, galaxies are dragged toward the center of the cluster over time due to tidal friction, so older galaxies are on average more clustered near the cluster center and they are expected to be fainter due to the surface brightness-age relation. Then a cluster-centric trend in surface brightness is expected (Tremmel et al. 2020). In the same way, the fraction of LSB dwarf galaxies with respect to non LSB dwarf galaxies should increase toward the cluster center (Tremmel et al. 2020). Unfortunately, the cluster center is the densest region in terms of objects and in terms of spurious sources that have to be modeled and subtracted before searching for LSB galaxies.

Most of the LSB galaxies are low-mass dwarf galaxies, but massive LSB galaxies also exist (e.g., Impey & Bothun 1997). More massive LSB galaxies are typically blue, slowly star-forming spiral galaxies (McGaugh & Bothun 1994), whereas less massive LSB galaxies are both blue star-forming and red quiescent dwarf galaxies (Román & Trujillo 2017b). In addition, a tidal dwarf galaxy is a galaxy that is formed in tidal tails during a merger or interaction between massive galaxies (e.g., Duc et al. 2014). Unfortunately, after the dissolution of the tidal feature, it is very difficult to distinguish tidal dwarf galaxies from normal dwarf galaxies. They should
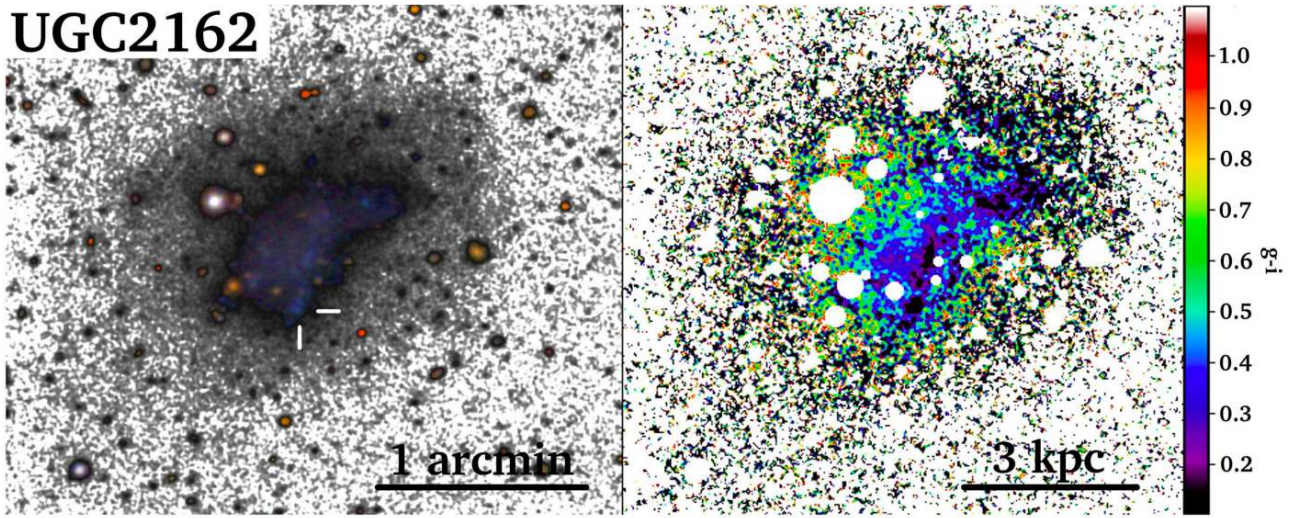
FIGURE 1.1: Example of UDG by Trujillo et al. (2017). Left panel: g', r', and i' band composite image centered on UGC 2162. The spatial location of the SDSS spectrum of this galaxy is indicated with white ticks, which correspond to RA= $02^h40^m23^s$ and DEC= $1°13'45''$ (J2000.0). Right panel: (g'-i') color map of UGC 2162. The central irregular region is located on top of a more rounded and extended disk-like structure.

lack in DM and have a higher metallicity for their masses (Duc et al. 2007), but both properties require high resolution spectroscopy with long integration times to be proved.

Clusters of galaxies grow in mass with time due to the continuous accretion of groups of galaxies. While in-falling the external processes (harassment, RPS, threshing, and major/minor mergers) become stronger and more frequent due to the higher density environment. Environments of different masses have different galaxy populations, according to the morphology-density relation. Most low-mass LSB galaxies in clusters are expected to be quiescent and gas poor because in a cluster environment RPS and harassment should quench their star formation.

In-situ stellar-mass build up of a galaxy is the formation of new stars caused by the gravitational collapse of the cold and dense gas component of the interstellar medium. Ex-situ stellar-mass build up of a galaxy is the accretion of already formed stars from outside the galaxy. It mainly consists of galaxy mergers and accretion of small satellites, whereas in the case of harassment the vast majority of stripped stars are expected to wander in the intra-cluster medium due to the high velocity of the encounter. Satellite galaxies are expected to sink to the center of the potential well of their host galaxies due to dynamical friction (Ostriker & Tremaine 1975).The stellar-mass build up mostly goes from in-situ to ex-situ having from the low to high galaxy mass regimes (e.g., Clauwens et al. 2018).

Satellites with long dynamical friction timescales are still found orbiting their hosts. The satellites suffer from tidal disruption as they orbit in the host galaxy DM halo. Therefore, the kinematic and morphological properties of LSB galaxies are particularly susceptible to tidal forces due to their low stellar mass content. The expected degree of disturbance depends on the assumed gravity law and whether they have a dominant DM halo. This makes simulations of LSB galaxies useful not only for testing different formation scenarios but also to investigate the structure of the gravitational potential well and different gravity models (e.g., McGaugh & Bothun 1994).

1.2 Ultra-diffuse dwarf galaxies

A subgroup of LSB dwarf galaxies called ultra-diffuse galaxies (UDGs; Sandage & Binggeli 1984; van Dokkum et al. 2015; Lim et al. 2020), which are empirically defined to be faint ($\mu_{g,0} \geq 24$ mag arcsec^{-2}) and diffuse ($R_e \geq 1.5$ kpc) objects, has been studied in several environments in order to understand what causes their large sizes and low surface brightnesses (Fig. 1.1).

With stellar masses similar to dwarf galaxies ($10^7 - 10^8$ M$_\odot$), UDGs could be "failed" galaxies having lost
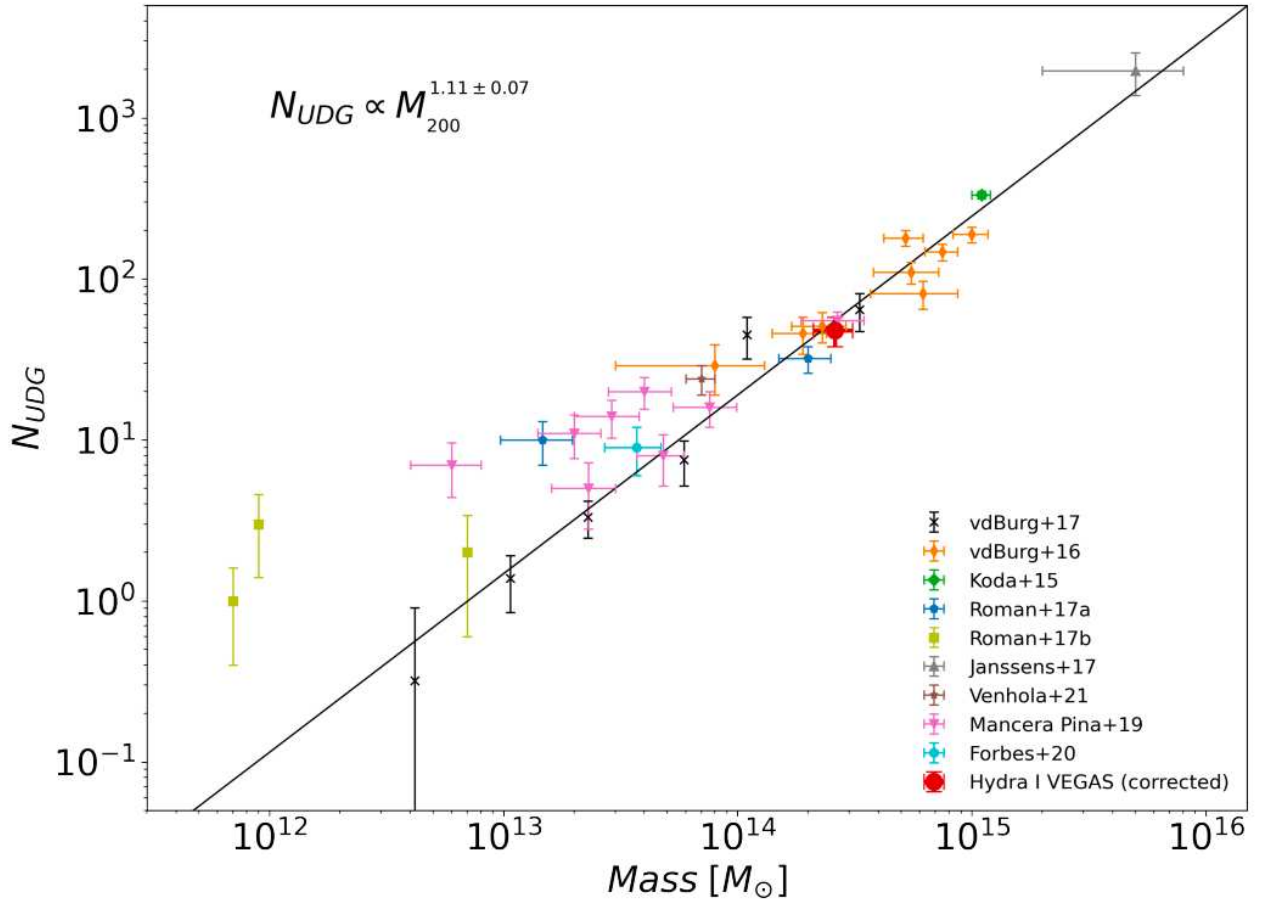
$$N_{UDG} \propto M_{200}^{1.11 \pm 0.07}$$

FIGURE 1.2: Abundance of UDGs as a function of the halo mass by La Marca et al. (2022a).

their gas supply at an early epoch and they should have an extremely dense DM halo to survive in galaxy clusters (van Dokkum et al. 2015). UDGs with stellar masses and DM content consistent with dwarf galaxies could form as a consequence of anomalous high spins of DM halos (Amorisco & Loeb 2016; Tremmel et al. 2019). Recent IllustrisTNG cosmological hydrodynamical simulations suggested that two classes of UDGs might exist (Sales et al. 2019): one found in the field and defined as "genuine" UDGs, the other near the cluster center, which shaped their large size and low surface brightness by the tidal forces. These tidal UDGs are characterised by a lower velocity dispersion, higher metallicity, and lower DM content than the "genuine" UDGs. Tidal forces during galaxy interactions were also invoked to explain the formation of the DM-free tidal dwarf galaxies (Montes et al. 2020)

A significant population of UDGs has been found in dense environments as well as in the field (e.g., Koda et al. 2015; van der Burg et al. 2016, 2017; Mancera Piña et al. 2019; Venhola et al. 2022).

The concentration of the UDGs light distribution and their projected shapes are very similar to those of dwarf galaxies of the same mass but higher surface brightness (Mancera Piña et al. 2019). They also have a bimodal color distribution similar to the other dwarf galaxies (Román & Trujillo 2017b). From spectroscopic studies of small samples of UDGs, we know that their stellar populations and kinematics are similar to those of other dwarf galaxies (Ruiz-Lara et al. 2018; Chilingarian et al. 2019).

It is crucial to understand how UDGs fit into the broader context of the LSB galaxy population and whether these galaxies have different formation paths as a function of physical properties (e.g., size, mass, and color) and environment. If UDGs are a new class of objects or not is still debated. Some studies found little evidence of UDGs constituting a distinct population of dwarf galaxies (e.g., van der Burg et al. 2016; Mancera Piña et al. 2018; Iodice et al. 2020a) In contrast, other studies point to UDGs being the diffuse end in the continuum of dwarf galaxy properties (e.g., Koda et al. 2015; Mancera Piña et al. 2019; Lim et al. 2020). .

Recently, Lim et al. (2020) have studied the UDGs in the Virgo cluster with a complete galaxy sample and

showed that they are the normal diffuse end tail of the cluster dwarf galaxy population. Contrary to previous studies (e.g., Mancera Piña et al. 2018), they have also found that the UDGs are more centrally clustered than other dwarf galaxies, in agreement with simulation predictions (Sales et al. 2020). This clearly demonstrates how important it is to place UDGs in the context of a complete census of galaxies.

Unfortunately, few spectroscopic datasets are available for UDGs (Emsellem et al. 2019), which strongly limit the estimate of DM content and stellar population content on a statistical basis. Nevertheless, these few studies reveal the existence of metal-poor ($-1.5 \leq [M/H] \leq -0.5$ dex) and old systems (about 9 Gyr, e.g., Fensch et al. 2019)as well as of younger star-forming UDGs (Martín-Navarro et al. 2019).

It is generally accepted that a multiple scenario for the UDG formation is in act. Hence, the measure of UDG properties through photometry leads to the measure of the tail of size-luminosity distribution of LSB dwarf galaxies without giving insight to the star formation history of them.

Despite the variety of the structural properties observed for UDGs, the super-linear relation found between the abundance of UDGs N_{UDG} and halo mass M_{200} (van der Burg et al. 2017; Janssens et al. 2017) of the host environment strongly suggests an internal formation mechanism (Fig. 1.2). The N_{UDG}-M_{200} relation can be reproduced by theoretical simulations assuming that the physical mechanism that is responsible for the properties of UDGs is independent of environment and that the majority of satellite UDGs have low-mass halos (Amorisco & Loeb 2016). Under these assumptions, Amorisco (2018) showed that UDGs are a consistent fraction of the galaxy population in all environments.

1.3   Aim and content of the thesis

The aim of this thesis is to detect and study the LSB galaxies and UDGs of Centaurus cluster using wide-field, deep-imaging data from the VEGAS. In order to understand how the scaling relations of the sample LSB galaxies and UDGs interface with their current formation theories from cosmological hydrodynamical simulations. I also test the possibility of building an automatic tool for the data analysis, which starting from deep imaging data gives as output the catalog of galaxies that includes their main properties.

The thesis is organized as follows:

- In Chapter 2, I present my dataset. I describe the setup and scientific purposes of the VLT Survey Telescope (VST) and its imaging camera OmegaCAM in Sec. 2.1. Then I provide an overview of the scientific purposes and outcomes of the VST surveys in Sec. 2.2, with a particular focus on VEGAS in Sec. 2.3. Finally, I provide a description of the images of the Centaurus cluster from VEGAS survey, that I analyse in this thesis, in Sec. 2.4.

- In Chapter 3, I describe the data analysis. I explain how I detect LSB galaxies in Sec. 3.1. Then, I apply a statistical method to distinguish cluster members from background sources in Sec. 3.2. I fit the light distribution with bidimentional models in order to retrieve the azimuthally-averaged light profile that I fit in Sec. 3.3. Finally, I retrieve the total magnitude from the growth curve in Sec. 3.4.

- In Chapter 4, I discuss the physical properties of the LSB galaxies that I found in the Centaurus cluster. I compare my new catalog of dwarf galaxies with another catalog available in the literature in Sec. 4.1. Then, I present the spatial distribution of the sample of LSB galaxies in Sec. 4.2 and their scaling relations in Secs. 4.3 and 4.4. I introduce the UDGs in Sec. 4.5 and discuss their abundance in Sec. 4.6. Finally, I discuss the trends of the properties of the LSB galaxies with cluster-centric distance in Sec. 4.7. I summarize the results in Sec. 4.8.

- In Chapter 5, I discuss my results and present my conclusions. I compare the properties of the LSB galaxies in the Centaurus with the LSB populations of other clusters in Secs. 5.2 and 5.3. Then, I discuss the implication of the number of detected UDGs and I compare two different definitions of UDGs in Sec. 5.4. Finally, I give my conclusions and future perspectives in Secs. 5.5 and 5.6, respectively.

Chapter 2

Data acquisition

In this chapter I present my dataset. I describe the setup and scientific purposes of the VLT Survey Telescope (VST) and its imaging camera OmegaCAM in Sec. 2.1. Then I provide an overview of the scientific purposes and outcomes of the VST surveys in Sec. 2.2, with a particular focus on VEGAS in Sec. 2.3. Finally, I provide a description of the images of the Centaurus cluster from VEGAS survey, that I analyse in this thesis, in Sec. 2.4.

2.1 Very Large Telescope Survey Telescope

The Very Large Telescope (VLT) Survey Telescope (VST) is located at European Southern Observatory (ESO) Paranal Observatory, a perfect site for ground-based astronomical observations, where the VST operates since 2011 (Arnaboldi et al. 1998). It is one of the largest telescopes in the world designed for surveying the sky in visible light. The seeing at Paranal is typically smaller than 1 arcsec, with more than 70% of photometric nights (Dali Ali et al. 2010).

The VST (Fig. 2.1) comprises two mirrors, a primary mirror (M1) with a diameter of 2.61 m and a smaller secondary mirror (M2) with a diameter of 93.8 cm. The optical system is based on Ritchey-Chrétien configuration with mirrors designed in order to cancel each other as much aberration as possible, the coma in particular.

The telescope is equipped with an Atmospheric Dispersion Corrector (ADC), which is an optical system made of four rotating prisms that counterbalances the spectral dispersion introduced by the atmosphere. The overall effect of atmospheric chromatic aberration depends on the zenith angle of the target, and it varies with environmental conditions, such as altitude, temperature, pressure, and humidity at the observation site. The rotating angle of the prisms is computed through an atmospheric model that takes into account the pointing position of the telescope and environmental conditions (Schipani et al. 2010).

The VST optics also includes a field corrector which is required to deliver a good optical quality over the whole field of view (FoV). It is composed of three lenses, two hosted in the telescope and one within the camera.

The alt-azimuthal mount supports and points the telescope maintaining the sidereal tracking speed. A derotator can compensate for image rotation due to the apparent field rotation of the alt-azimuthal mount, thus, the telescope works in field stabilized mode.

Celestial sources located outside the Solar System are considered point sources that emit isotropically. On our planet, the spherical wave fronts have such a great curvature radius that can be considered flat. Thermal and gravitational gradients inside the telescope change the flatness of the wave front and these deformations are seen in the point spread function (PSF) as aberrations. The telescope optics are specifically shaped in order to reduce the aberration.

In addition, the VST implements an active optics system (AO) in M1, which is made of 81 actuators that push and pull the mirror in order to modify its shape.Part of the light collected by the telescope is sent to a curvature wave front sensor (WFS) that computes the wave front shape with a frequency $\leq 1\,$Hz and an adequate resolution to the degrees of freedom of the AO (Noethe 2002). M2 is equipped with a hexapod that
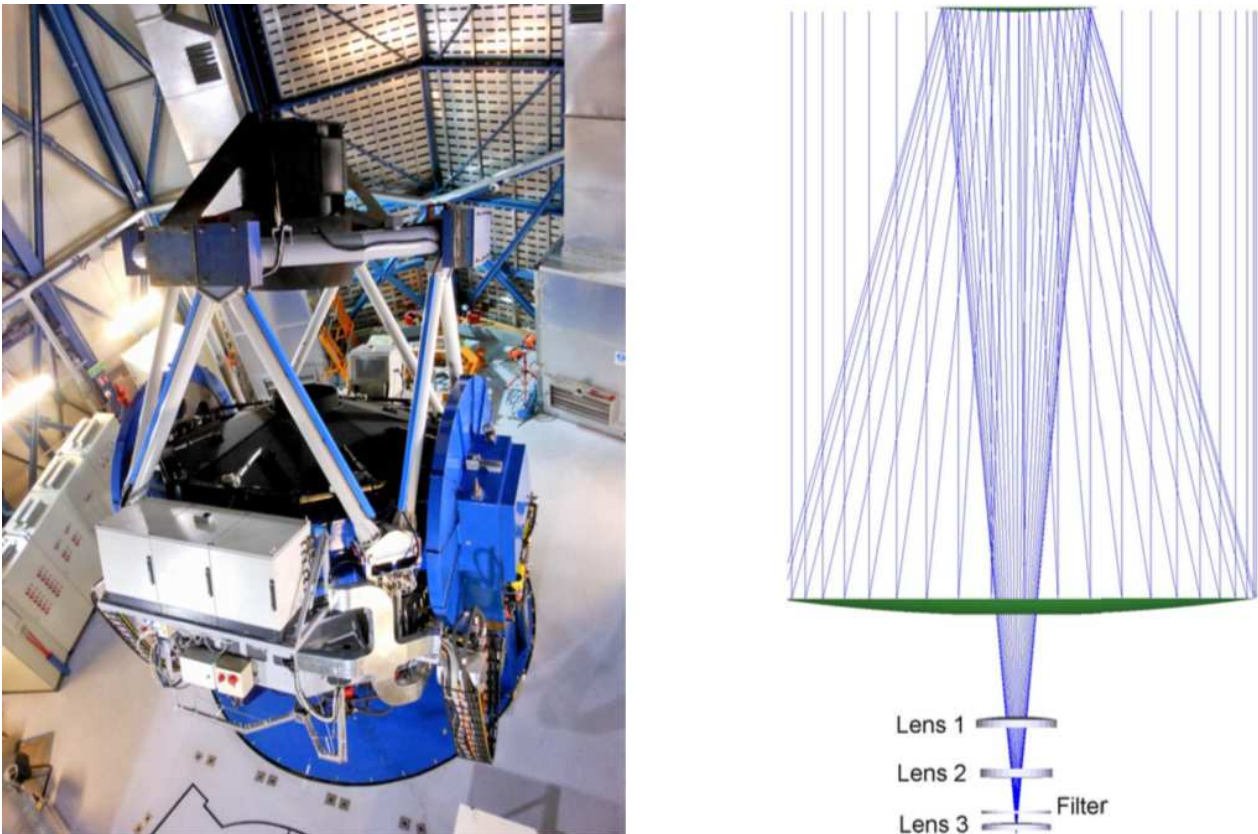
FIGURE 2.1: The VST telescope. Left panel: The VST in its dome at Paranal Observatory. Right panel: The optical design of VST. The three lenses compose the field corrector and the filter wheel is placed between Lens 2 and Lens 3 (Schipani et al. (2012)).

keeps the focus position constant while M1 shape changes. The hexapod is a robot composed of six legs driven by motors, linking a fixed platform connected to the telescope structure to a mobile platform connected to M2. The motors adjust the length of the legs, driving the mirror to the desired position and orientation (Schipani et al. 2006). The VST hexapod mechanics is based on the Telescopio Nazionale Galileo (TNG) implementation (Bortoletto et al. 1999).

The VST has a total FoV of 1×1 deg^2 which is twice as wide as the full Moon. It supports the VLT with wide-angle imaging by detecting and pre-characterising sources, which the VLT can further observe.

The VST is a joint project between the ESO and Capodimonte Astronomical Observatory (OAC), part of the Italian National Institute for Astrophysics (INAF). The Italian centre designed the telescope, while ESO was responsible for the civil engineering works at the site and the telescope operations until 2022. Since 2021 the telescope is owned by INAF.

The VST is equipped with the 770 kg OmegaCAM camera, made of 4×8 mosaic CCD (Fig. 2.2), sealed in vacuum, that together create an of 268-megapixel images with a pixel size of 15 μm. It is a visible-light camera that perfectly complements ESO Visible and Infrared Survey Telescope for Astronomy (VISTA; Sutherland et al. 2015). Since 2011, OmegaCAM is the wide-field imager for the Cassegrain focus of the VST (Kuijken et al. 2002; Kuijken 2011). OmegaCAM was built by a consortium of institutes, which in turn coordinate the contributions of more institutes in the following countries:

- The Netherlands: NOVA, Kapteyn Instituut Groningen, OmegaCEN.

- Germany: Universitäts-Sternwarte München.

- Italy: Osservatorio Astronomico di Padova (INAF-OAPd).

- ESO.

OmegaCAM samples the 1×1 deg^2 FoV with 32-CCD, $16\,\mathrm{k} \times 16\,\mathrm{k}$ pixel detector mosaic at 0.21 arcsec pix^{-1}. Image quality is specified such that in the absence of seeing 80% of the energy from a point source should
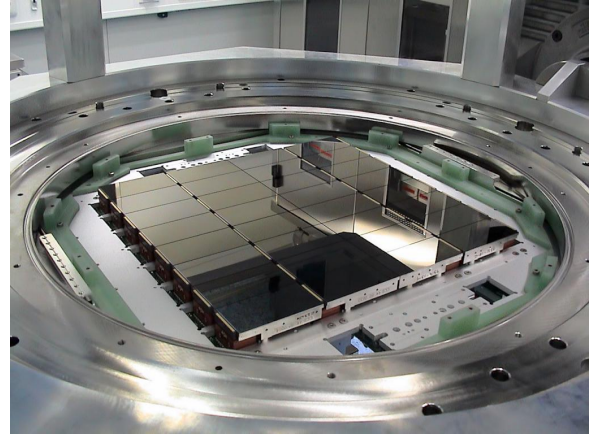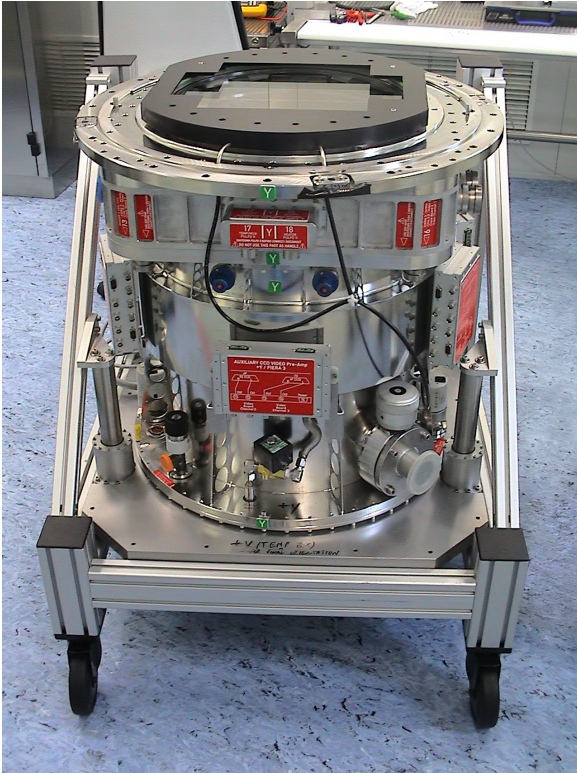
FIGURE 2.2: Left panel: OmegaCAM. Credits: ESO. Right panel: The 32 CCDs of OmegaCAM. Credits: ESO

fall within a 2×2 pixel area over the full FoV. The field distortion is very small, so that the image scale is virtually constant over the whole FoV. There are narrow gaps of 25 arcsec and 85 arcsec between the CCDs. The overall geometric filling factor of the array is 91.4%. In addition to the 32 CCDs making up the science array, OmegaCAM also contains four auxiliary CCDs beyond the edges of the field. Two of these are used for autoguiding, so that both field position and rotation can be accurately tracked. The other two auxiliary CCDs are mounted 2 mm outside the focal plane (one in front, one behind), and are used for recording defocused star images for curvature wavefront sensing and controlling the AO of the VST.

A filter exchange mechanism permits observations through any one of the filters. OmegaCAM has the broad Sloan u', g', r', i', and z' filters, as well as the Johnson-Cousin B and V, Strömgren v, and several narrow-band filters. A special calibration filter, segmented in four quadrants with u', g', r', and i', for extinction measurements is also part of the set. Figure 2.3 shows the combined throughputs of the VST, OmegaCAM and Sloan filters[1].

2.2 VST surveys

The primary function of the VST is to support the VLT by providing surveys regarding the Milky Way, extra-galactic targets, and cosmology.

The VST is making important discoveries in a variety of areas of astrophysics and cosmology. The Galactic plane is extensively studied providing astronomers with crucial data for understanding the structure and evolution of our Galaxy. Moreover, the VST is exploring nearby galaxies, extragalactic and intracluster planetary nebulae and it is performing surveys of faint objects and micro-lensing events. In the field of cosmology, the VST is targeting medium-redshift supernovae to help pin down the cosmic distance scale and to understand the expansion of the universe. The VST is also looking for cosmic structures at medium-high redshift, active galactic nuclei and quasars to improve our understanding of galaxy formation and the early history of the universe. A brief description of the main surveys carried out at the VST is provided below:

---

[1]The throughputs of the full set of filters can be found at `http://www.eso.org/observing/etc/bin/simu/calibdisp?INS.NAME=OMEGACAM+INS.MODE=none`
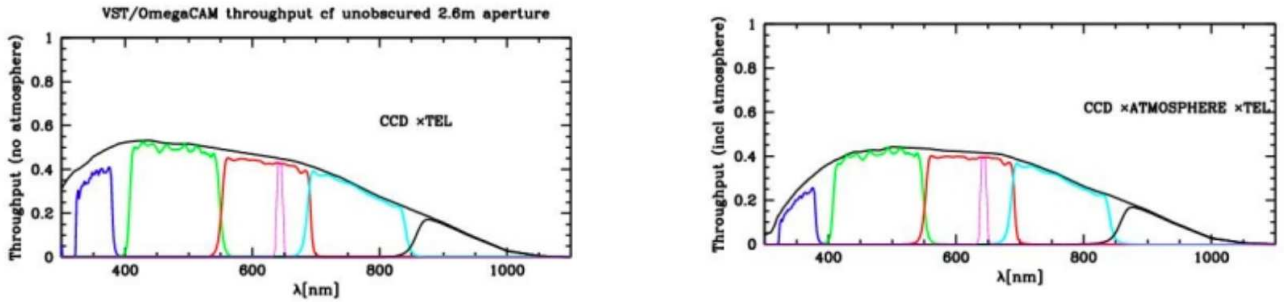
11

FIGURE 2.3: The throughput of OmegaCAM Sloan filters. Left panel: Combined throughput of the CCD and u' (blue), g' (green), r' (red), H_α (pink), i' (light blue), and z' (black) filters. Right panel: Combined throughput of the CCD, telescope, and u' (blue), g' (green), r' (red), H_α (pink), i' (light blue), and z' (black) filters.

- The VST Photometric H_α Survey of the Southern Galactic Plane (VPHAS+; Drew et al. 2014), is covering about 1800 deg^2 using five bands (u', g', H_α, r', and i'). VPHAS+ is studying around 500 million objects including many rare star types such as Be and T-Tauri stars. The survey is also eployed to map the structure of the Galactic disk and to understand the star-formation history of the Milky Way. The survey reached the 24% completion with Data Release 2 (DR2), and the 96% with DR4[2] available at ESO database but not published yet.

- The VST ATLAS (Shanks et al. 2013) covers about 5000 deg^2 of the Southern sky in five filters (u', g', r', i', and z') to depths comparable to those of the Sloan Digital Sky Survey (SDSS, Ahnet al. 2012). This survey is also complemented by near-infrared data from the VISTA Hemisphere Survey (VHS; McMahon et al. 2013). The primary aim is to examine "baryon wiggles" (small-amplitude oscillations observed in the power spectrum of galaxies) by looking at luminous red galaxies in order to determine the dark energy equation of state.

- The Kilo Degree Survey (KIDS; de Jong et al. 2013) is mapping the large-scale mass distribution in the universe and constraining its expansion history by means of weak gravitational lensing and photometric redshift measurements. These goals put stringent requirements on image quality and stability, photometric depth and calibration accuracy. This survey is imaging about 1500 deg^2 in four bands (u', g', r', and i'). The data collected is complemented by near-infrared observations from the VISTA Kilo-Degree Infrared Galaxy survey (VIKING; Edge et al. 2013) that observes the same area in z', Y, J, H, and K_s. KIDS science goals include studying dark matter halos and dark energy with weak lensing, hunting for high-redshift quasars and galaxy clusters, and studying galactic evolution. In 2019 the team published the DR4 saying that the upcoming DR5 should be the last one (Kuijken et al. 2019).

In addition to the three public surveys described above, a set of projects are being carried out under the Guaranteed Observing Time (GTO) agreement between ESO and INAF-OAC. The GTO was the 10% of total observing time for the first four years, 20% for the next two, and 20% for the last four. From 2022 the VST will be fully operated by INAF. The GTO surveys include:

- the VST survey of the Small Magellanic Cloud and Magellanic Bridge (STEP; Ripepi et al. 2014);

- Structure and Evolution of the Galaxy (STREGA; Marconi et al. 2014);

- the study of the NIR luminosity function and stellar mass function of galaxies in the Shapley supercluster environment (ACCESS; Merluzzi et al. 2010);

- the study of the fundamental plane of ETGs in nearby clusters (WINGS; D'Onofrio et al. 2008);

- the study of the Galaxy evolution, AGN variability and supernova host galaxies (SUDARE/VOICE P.I. M. Vaccari);

- VEGAS (Iodice et al. 2021b).

---

[2]https://www.vphasplus.org/vphasplus-dr4-release-description.pdf

2.3   VEGAS project

In this section I describe in detail VEGAS project (P.I. E. Iodice), since this thesis is based on such a data-set. The VST early-type Galaxy Survey is a deep multi-band (u', g', r', and i') imaging survey carried out with the VST using the GTO assigned at the INAF-OAC. Using about 500 hours of observing time between 2016 and 2022, VEGAS has collected data on 35 groups and clusters of galaxies, covering a total area on the sky of ~ 70 deg^2. About 30% of the VEGAS observing time was dedicated to the Fornax Deep Survey (FDS; Peletier et al. 2020). The FDS covers the Fornax cluster out to the virial radius (~ 0.7 Mpc), taking in an area of 26 deg^2 around the central galaxy NGC 1399 and including the SW subgroup centred on NGC 1316.

2.3.1   VEGAS science goals

Exploring the LSB universe is one of the most challenging tasks in the era of deep imaging and spectroscopic surveys. It is a crucial ingredient to map the mass assembly of galaxies at all scales and all environments, and thus constrain their formation within the Λ Cold Dark Matter (ΛCDM) paradigm. In this framework, clusters of galaxies are expected to grow over time by accreting smaller groups. During the infall process, the material stripped from the galaxy outskirts builds up the stellar halos and the intracluster light (ICL; e.g. Contini et al. 2014; Cui et al. 2014; Pillepich et al. 2018). These are diffuse and very faint ($\mu_g > 26$ mag arcsec^{-2}) components made of stars stripped from satellite galaxies, also in the form of streams and tidal tails, with multiple stellar populations and complex kinematics, which are still growing at the present epoch.

The main science goals of VEGAS are: i) mapping the light distribution and colors out to $8-10\,R_e$ and down to the faint surface brightness levels of $\mu_g = 31$ mag arcsec^{-2}, $\mu_r = 28$ mag arcsec^{-2}, and $\mu_i = 27$ mag arcsec^{-2}; ii) studying the galaxy structure and its faint stellar halo, including the diffuse light component, inner substructures as signatures of recent cannibalism events, inner disks and bars; iii) detecting the external ICL and the LSB structures in galaxies, like tidal tails, stellar streams and shells and study the connection with environment; and iv) studying the globular clusters and galaxy satellites in the outermost regions of galaxies in the local universe ($D < 50$ Mpc). Finally, the full sample proposed by VEGAS is providing essential statistical constraints on theoretical models and enabling discrimination among competing galaxy formation theories (Capaccioli et al. 2015; Iodice et al. 2021a).

VEGAS is playing a pivotal role in exploring the properties of galaxies as a function of the environment down to the LSB regime. Based on the analysed data, VEGAS and FDS have allowed us to i) trace the mass assembly process in galaxies by estimating the accreted mass fraction in the stellar halos and provide results that can be directly compared with the predictions of galaxy formation models (Spavone et al. 2020); ii) provide the largest size- and magnitude-limited catalogue of dwarf galaxies in the Fornax cluster (Venhola et al. 2018) and detect UDGs (Forbes et al. 2020; Iodice et al. 2020a); iii) study the outskirts of the galaxies and detect the ICL and LSB features in the intracluster/group space (Iodice et al. 2016, 2020b; Spavone et al. 2018); and iv) trace the spatial distribution of candidate GCs (Cantiello et al. 2020).

The first data release (DR1; Iodice et al. 2021b) of VEGAS has provided the reduced VST mosaics of 10 targets. After eight years, the full sample has been almost observed and the science goals have been successfully achieved. However, the VEGAS sample can be considered as a gold mine to deeper investigate the LSB regime. In particular, there are three main still ongoing VEGAS projects are: i) studying of the large-scale structure around groups and clusters, including the unexplored regions of voids and filaments down to the LSB regime (ELATE; P.I. M. Raj); ii) studying the amount of intra-group light (IGL) as well as studying the light and colour distributions in order to address the main formation process of the IGL component in groups of galaxies. (P.I. R. Ragusa; Ragusa et al. 2021, 2022); and iii) identifying and studying a large number (~ 1300) of UDGs in a wide range of environments (UltraVEGAS project, P.I. E. Iodice).

2.3.2   Observing strategies

VEGAS data were collected with two different observing strategies: the step-dither and standard mode. Regardless of the strategy, VEGAS images are mosaics of multiple dithered frames, thus they can be much larger than the 1×1 deg^2 FoV of OmegaCAM. The dither technique consists in slightly changing the telescope pointing from frame to frame. The dithers are used not only to cover the CCD gaps, but also to reduce the spatial

noise, to have better sky estimates (Anderson 2020), and to increase the FoV.

Step-dither mode: This technique mimics the ON-OFF procedure devised in infrared astronomy. It is typically used when the FoV is saturated by the sources, thus it is not possible to identify a void region to estimate the sky. It consists of a cycle of short exposures of 150 sec on the target (science frames) and 150 sec on the sky (sky frames). This process is done repeatedly until the desired exposure time is reached. In order to reach the depth of $27 - 30$ mag arcsec^{-2}, the sky frames have to be taken as close as possible, in space (≤ 0.3 deg) and time, to the science ones (Iodice et al. 2021b).

Standard mode: For less extended objects, the sky background can be estimated on the science frame by using a polynomial surface fit over the entire mosaic. In this case, the adopted observing strategy is the standard diagonal dithers to cover the CCD gaps (Capaccioli et al. 2015).

2.3.3   Data reduction

VEGAS observations performed between 2014 and 2016 were processed with the VST-tube pipeline designed for the VST-OmegaCam observations (Grado et al. 2012; Capaccioli et al. 2015). Since 2018, the VEGAS data are reduced with the Astro-WISE data-reduction pipeline (Begeman et al. 2013; McFarland et al. 2013b); Valentijn & Kuijken 2004.

Astro-WISE is a data-centric survey handling system based on object-oriented programming (OOP). In OOP, is a programming paradigm that relies on the concept of `objects` and `classes`. In Astro-WISE, all survey handling is implemented as operations by data `objects` on other data `objects`. It means that any type of survey product, from raw to final, is represented by a `class` of data `objects`. The pipeline performs the standard pre-reduction steps, gain harmonisation of the 32 CCDs, illumination correction and defringing for the i' band. Relative and absolute astrometric and photometric calibrations are applied before creating the final co-added image mosaics. Astro-WISE is maintained by Astro-WISE Consortium[3], which is a data center hosting data for various astronomical projects. It is a private pipeline but publicly available to the members of the consortium or under request by single users. Astro-WISE was conceived to handle the vast amount of astronomical data generated by all-sky surveys, particularly those to be observed with OmegaCAM on the VST, but it has been also used for several other instruments.

The instrumental corrections applied to each frame include overscan correction, removal of bias, flatfielding, illumination correction, masking of the bad pixels, and subtraction of the background. The data is overscan corrected.

The detailed description of the data reduction procedure followed by the VEGAS collaboration is described in Venhola et al. (2018). The main data reduction steps are shortly described below.

Bias correction: The read-out noise (RON) is the noise introduced in the data by the read-out process of the CCDs. It is measured from pairs of bias exposures. The read noise in Analog-to-Digital Unit (ADU) is the root mean square (RMS) of the difference between two bias exposures divided by $\sqrt{2}$. In VEGAS, the bias frames are taken and the bias subtraction is done in two steps for each CCD. First, for the row-wise median value of the overscan area is subtracted to the data (overscan correction). Then, the overscan-corrected bias frames, that are typically $10 - 15$ frames, are stacked to create a master bias which is subtracted to the data. Data corrected for bias are said to be debiased.

Flat-fielding: A flat-field is the response of the telescope-camera system to a source of uniform radiation. There are different ways to construct a flat-field. Dome flat-fields are created by pointing the telescope at a screen inside of the dome which is illuminated by lamps. It is obtained through an average with sigma-clipping procedure (Sec. 3.2.1) on a stack of raw dome flats, intended to reduce photon shot noise and remove cosmic rays.

---

[3]The Astro-WISE Consortium is a partnership of OmegaCEN-NOVA at the Kapteyn Institute in Groningen, INAF, Terapix at IAP in Paris, ESO, Universitäts-Sternwarte München, and Argelander-Institut für Astronomie in Bonn.http://www.astro-wise.org/consortium.shtml

The procedure to make a `DomeFlatFrame` starts with $5 - 10$ overscan corrected, trimmed of the overscan region and debiased raw dome flat-fields. These are normalized to the median, taking into account hot and cold pixels, and averaged rejecting 5σ outliers. The median of the stack is used to determine the σ levels. The computed mean of the stack is the final `DomeFlatFrame` image. Lastly, sub-window image statistics are determined for quality control purposes (McFarland et al. 2013a).

Twilight flat-fields are created by pointing the telescope to the sky at the twilight. A `TwilightFlatFrame` is made following the same procedure described below for the `DomeFlatFrame`.

Dome flat fields have the advantage (over twilight flat fields) that it is easy to repeatedly obtain a high signal-to-noise (S/N) level. Disadvantages are that the direction in which light enters the telescope may be different than that of night time observations, color of the dome lamp differs from the color of the night sky and that it is very difficult to illuminate a screen in such a way that it is a source of uniform radiation. A dome flat-field is useful for tracing small scale structure variations. A disadvantage for twilight-flat fields is that they can already contain objects like stars during exposures, which should be corrected for by dithering the twilight flat-fields. Twilight flat fields thus are better in tracing large scale structure variations. To study the LSB universe it is necessary to increase the exposure time and, at the same time, have a good S/N. The main limiting factor of this is the spatial noise which is reduced by flat-fielding. Thus, to study the LSB universe it is fundamental to trace both the large- and the small-scale sensitivity variations of the CCDs. These considerations result in the need to combine dome flats and twilight flats by spatially filtering the two types of flat fields.

In VEGAS, `Flatfielding` is done after bias correction using a `MasterFlatFrame` which is combined from eight twilight flat-fields and eight dome flat-fields. Before combining the different flat-fields, the high spatial frequencies are filtered out from the twilight flat-fields, and the low frequency spatial Fourier frequencies from the dome flatfields. This approach is adopted, since the dome flatfields have better S/N to correct for the pixel-to-pixel sensitivity variations, whereas the twilight flatfields have more similar overall illumination with the science observations.

Weight maps: Hot pixels are pixels which have high count rates despite not being illuminated. These pixels are detected from bias images which have an exposure time of $0\,\text{s}$. More precisely, 5σ outliers in bias are defined as hot pixels. Cold pixels are broken pixels which have low or zero ADU even when they are illuminated. These pixels are determined from dome flat-field exposures. More precisely, a smoothed flat-field is used to normalize the flat-field to eliminate large deviations from flatness that could erroneously cause entire regions to be marked as "cold". In this flat-field image, pixels that are outside a given range ($\pm 4\%$) are taken to be cold pixels. This also identifies pixels that are brighter relative to their neighbours as cold. Note, that pixels above the threshold are formally not cold, but they are flagged anyway. The hot and cold pixel detection is done with a `SExtractor` (Bertin & Arnouts 1996) command to estimate the background.

A weight map has the same size of an image and values that range from 0 to 1. A weighted image is the image multiplied by the weight map. During the instrumental reduction, weight maps are created for each individual frame. Weight maps carry information about the defects and contaminated pixels in the image and the expected noise associated to each pixel. These pixels are then set to zero in the weight maps. The flat-fielded and debiased images are also searched for satellite tracks and cosmic rays, and the values of the pixels in the weight maps corresponding to the contaminated pixels in the science images are then set to zero. The Hough transformation method (Vandame 2001) is applied to the images to pick up the satellite tracks, which are eliminated by masking the lines consisting of more than 1000 pixels that have intensity above the 5σ relative to the background and are located on the same line. Cosmic rays are detected using `SExtractor`, and the corresponding pixels are masked from the weight map.

The weight maps W_{ij} have values:

$$W_{ij} = \frac{1}{\sigma^2} B_{ij} \tag{2.1}$$

where σ is the standard deviation of the background noise and B_{ij} is the combined bad pixel map where the bad pixels have been set to zero and other pixels to one.

Defringing in i' band:　　Fringing in a solid state detector chip is due to interference of incident photons with photons reflected in the detector chip substrate. The photons causing the strongest fringes are those of several skylines, mostly apparent at the long wavelengths, that can vary with filters. Normally, after flat-fielding, the background can be expected to be flat over the entire image and a median of the image, excluding 5σ outliers, would in principle be sufficient to subtract the background.

In images that suffer from fringing, we have to deal with a background that is variable on small (< 60 arcsec) scales within the image, and can not be distinguished from sources. The image itself can, therefore, not be used to determine the background. However, the information of several images can be combined to determine the background. This average should include enough observations to properly exclude contamination from sources.

During the night the brightness of the emission lines will change, especially near evening and morning twilight. The result of this is that the amplitude of the observed fringes will change. Therefore, fringe maps should be scaled to fit the amplitude of the fringes in each science frame.

The observations contain also an additional smooth light component resulting from scattered light. A careful removal of this component is essential for studying the outskirts of the galaxies and the low surface brightness objects. A background model is created first by scaling a set of 12 consecutive exposures of the targets and calculating the median by averaging the stack. The scaling factor s between images A and C is defined by measuring median values within small boxes in image A, and in the same locations in image C, and then taking the median of their ratios.

For each image to be stacked, such a scaling factor is defined with respect to A and the images are multiplied with these factors before stacking. If there is a large scatter between the ratios of s, the chip medians of the exposures are scaled with each other. The scaled images are then median stacked to the background model and the model is subtracted from image A. This strategy also allows to remove the fringe patterns appearing in the OmegaCAM in i'-band images, and also removes all the possible residual patterns from the flatfielding.

Illumination correction:　　Systematic photometric residual patterns still remain in all bands and are corrected by applying an illumination correction model to the data. The models were made by mapping the photometric residuals across the OmegaCAM CCD array using a set of dithered observations of Landolt selected-area standard-star fields (Landolt 1992) and fitting a linear model to the residuals (Verdoes Kleijn et al. 2013). The images were multiplied with this illumination correction. The illumination correction is applied after the background removal to avoid producing artificial patterns into the background of images.

Astrometric calibration:　　The reduced images are calibrated to world coordinates system (WCS) through a two-step process using `SCAMP` (Bertin 2006). First, the rough coordinate transformation is obtained by applying the shifts and rotations according to the image headers. Then, the fine tuning of the astrometric calibration is obtained by associating the source lists extracted from the science images with the 2 Micron All-Sky Survey Point Source Catalog (2MASS PSC; Skrutskie et al. 2006) and fitting the residuals with a second order polynomial plane. This polynomial correction is then applied to the data coordinates, and the pixel size is sampled to 0.2 arcsec pix^{-1}. The error in the astrometric calibration is of the order of 0.1 arcsec (Venhola et al. 2018).

Photometric calibration:　　The absolute zero-point calibration is done by observing standard star fields each night and comparing their OmegaCAM magnitudes with the SDSS DR12 (Alam et al. 2015) catalog values. The OmegaCAM point source magnitudes are first corrected for the atmospheric extinction by subtracting a term $k\chi$, where χ is airmass and k is the atmospheric extinction coefficient. The zero-point for a given CCD is the difference between the corrected magnitude of the object measured from a standard star field exposure and the catalog value. The zero-points are defined only once per night, so that for each science observation only the varying airmass is corrected. The extinction coefficient is computed at least three times per night by observing the north pole with the calibration filter. Typical values of the extinction coefficients at the VST site are 0.515, 0.182, 0.102, and 0.046 for u', g', r', and i' bands, respectively (Peletier et al. 2020). On photometric nights the extinction coefficient k is constant in space and time with respect to each passband. It means that the atmospheric extinction depends only on the airmass. It is fundamental to observe during fotometric night to avoid the systematic error due to k fluctuations.
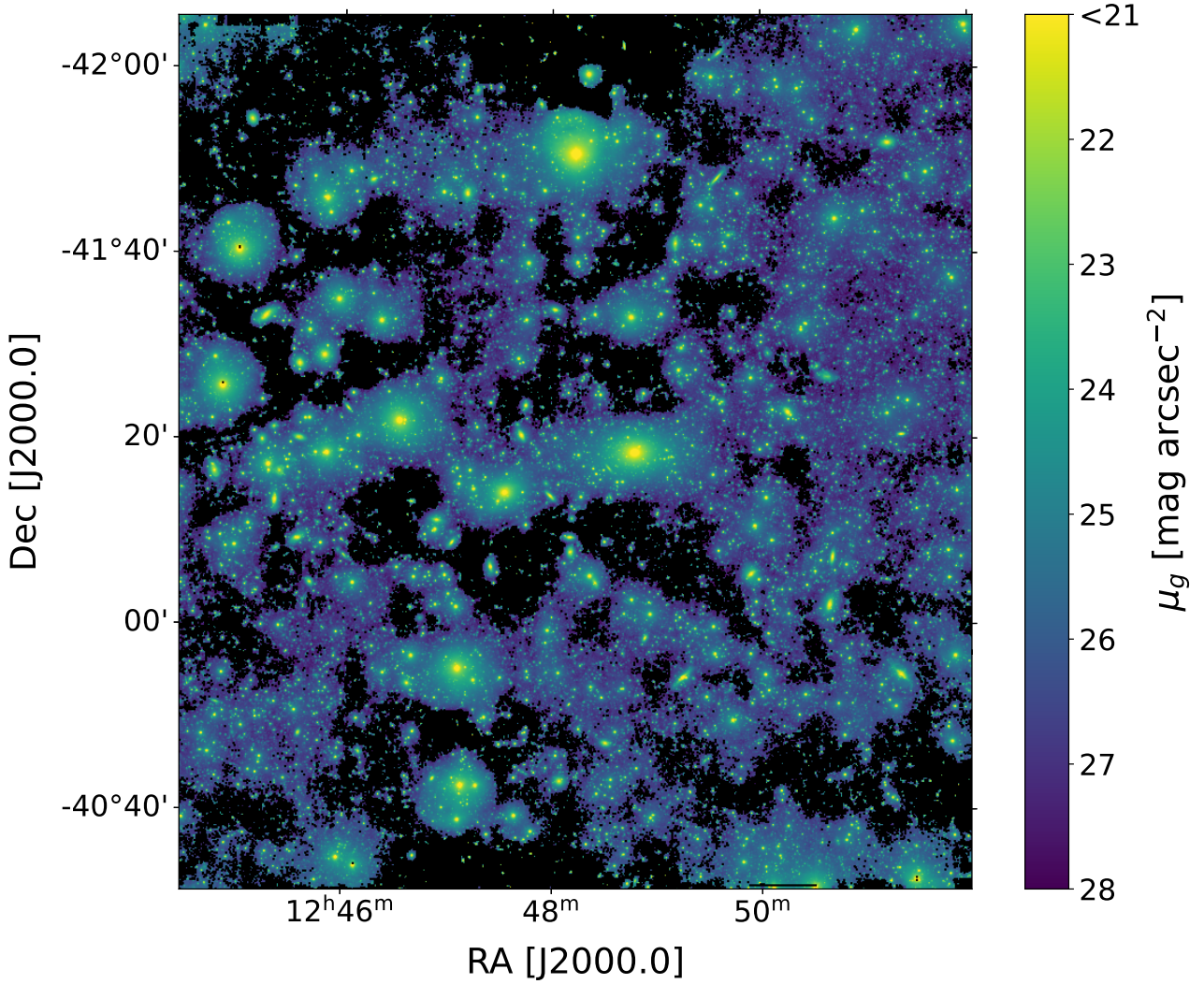
FIGURE 2.4: Image of Centaurus cluster in g' band from the VEGAS survey. The image is in log-scale with black pixels having negative ADU.

Mosaic: The calibrated exposures are median stacked into mosaic images using SWarp (Bertin 2010), and the contaminated pixels are removed using the weight maps. SWarp also produces a mosaic weight map for each mosaic using Eq. (2.1) where σ^2 is the variance associated to each pixel.

2.4 VEGAS imaging of the Centaurus cluster

In this thesis I present the search for LSB galaxies in the Centaurus cluster, which is one of the VEGAS fields not published yet. The total integration times of the two images which I analysed are 2.5 hours for each g' and r' bands. The VST mosaic covers an area of $1.4 \times 1.6 \ \mathrm{deg}^2$ (1 Mpc^2 at Centaurus distance) around NGC 4696 which is the brightest cluster galaxy (BCG).

The Centaurus cluster, also known as A3526, was classified as a cluster of richness class zero by Abell et al. 1989 and as a cluster of type I/II by Bautz & Morgan (1970). In X-rays it was extensively studied (Fukushima et al. 2022 and references therein). It has a bimodal temperature structure: an ancient cool core at $k_\mathrm{B}T = 4\,\mathrm{keV}$ (Fukazawa et al. 1994; Ikebe et al. 1999) and an hotter core at $k_\mathrm{B}T = 1\,\mathrm{keV}$ (Churazov et al. 1999) consistent with a major merger event. The cluster also shows an highly enriched intracluster medium ($1 - 2\,Z_\odot$) which is consistent with the bimodal temperature distribution and irregular X-ray isophotes (Furusho et al. 2001).

Using the Roentgen Satellite (ROSAT), Reiprich (2001) derived a total flux of $2.7 \times 10^{-10}\,\mathrm{erg\ s^{-1}\ cm^{-2}}$ in the energy range $0.1 - 2.4\,\mathrm{keV}$, corresponding to a bolometric luminosity of $0.6 \times 10^{44}\,h^{-2}\,\mathrm{erg\ s^{-1}}$ in the energy range $0.01 - 40\,\mathrm{keV}$.

The BCG NGC 4696 is located at RA = $12^{\mathrm{h}}48^{\mathrm{m}}49.25^{\mathrm{s}}$, DEC = $-41°18'40.0''$ (J2000.0) at a distance of $d = 36 \pm 3$ Mpc (Tully et al. 2016), which I assumed as the distance for all galaxies within the cluster. After Virgo, Fornax, and Hydra I clusters, Centaurus is the nearest cluster of galaxies and is still in an active phase of mass assembly process. Lucey et al. (1986) measured a bimodal velocity distribution of galaxies associated to the two sub-groups dominated by NGC 4696 and NGC 4709 and a velocity dispersion along the line of sight (LOS) of $\sigma_{\mathrm{LOS}} = 870\,\mathrm{km\,s^{-1}}$.

The stellar mass within the central 50 kpc of the Centaurus cluster is estimated to be 2×10^{12} M$_\odot$ (Ikebe et al. 1999). Reiprich (2001) used the X-ray mass-luminosity relation to retrieve the total mass of the cluster $M_{200} = 1.89^{+0.12}_{-0.09} \times 10^{14}\,h^{-1}$ M$_\odot$ enclosed in the radius $R_{200} = 0.935^{+0.020}_{-0.015}\,h^{-1}$ Mpc. From now on I assume $R_{200} = R_{\mathrm{vir}}$ in absence of other values in literature.

The step-dither strategy, coupled with the long integration times and large covered area, allows to study the Centaurus cluster down to $27 - 30$ mag arcsec^{-2} out to $\sim 0.7R_{200}$ (Iodice et al. 2021a). In addition, the large FoV of VST plays a crucial role in the study of a sufficiently large sample of LSB galaxies.

Wide-field, deep, and multiband photometric data allow to infer the properties of a large number of LSB galaxies. In particular, colors, total magnitude, central surface brightness, effective radius and Sérsic index are the most commonly used.

Figure 2.4 shows the g'-band VST mosaic of the sky area centered on NGC 4696. The image weighs 2.7 GB, so I applied a 8×8 rebinning for displaying purposes although decreasing its quality. I choose a specific color scale and range to enhance the LSB features on the image.

Chapter 3

Data analysis

In this chapter I describe the data analysis. I explain how I detect LSB galaxies in Sec. 3.1. Then, I apply a statistical method to distinguish cluster members from background sources in Sec. 3.2. I fit the light distribution with bidimentional models in order to retrieve the azimuthally-averaged light profile that I fit in Sec. 3.3. Finally, I retrieve the total magnitude from the growth curve in Sec. 3.4.

3.1   Detection of LSB galaxies

Part of the aim of this thesis is the detection of LSB galaxies. The method that I use is based on image segmentation, which is the main technique used by astronomical (and not) software to detect objects in an image. The most commonly used algorithm is `SExtractor` (Bertin & Arnouts 1996), which was designed for the detection of bright stars and galaxies. However, `SExtractor` has not proved particularly suitable for detection of faint sources such as LSB galaxies. For instance, Venhola et al. (2018) and La Marca et al. (2022b,a) applied `SExtractor` for the detection of dwarf galaxies and they had to complete their sample by visual detection. For LSB galaxies located near relatively bright objects, `SExtractor` tends to shred the LSB galaxy into multiple objects, or does not register a detection. `SExtractor` detection is far worse for dwarf LSB galaxies that appear as amorphous structures just visible above the background noise. In addition, `SExtractor` apertures are not adequate for the majority of very LSB galaxies (Hammer et al. 2010).

Soon visual detection will not be anymore an option, because current projects aim to produce a huge quantity of data. For instance The Legacy Survey of Space and Time (LSST) aims to produce around 15 TB of raw data per night (Ivezić et al. 2019). Hence, the motivation to develop new softwares for the detection of LSB features, such as `Max-Tree Objects` (MTO; Teeninga et al. 2015), `NoiseChisel` (Akhlaghi & Ichikawa 2015), and `ProFound` (Robotham et al. 2018), which are still under testing and implementation. `NoiseChisel` and `MTObjects` are capable of locating the faint outskirts of objects, whereas `SExtractor` is the faster. No tool has sufficient speed and accuracy to be well suited to perform large-scale automated segmentation in its current form (Haigh et al. 2021).

My thesis work is aimed at implementing an efficient detection algorithm using straightforward and easily installable tools. I use `photutils` (Bradley et al. 2020), which is a `python` package that contains some functions for image detection based on image segmentation that are easy to implement. It is based on `scikit-image` (van der Walt et al. 2014) which is the state-of-the-art algorithm for image processing in `python`.

The steps of my data analysis are similar to those of La Marca et al. (2022a). The pipeline applied is semi-automatic, which means that for each step of the data analysis I check for the results and, if necessary, I change some parameters to get it working.

Figure 3.1 shows the LSB galaxy LSB100, which is part of the catalog of LSB galaxies that I obtain in this thesis. In this chapter I adopt LSB100 as example to explain the steps of my data analysis.
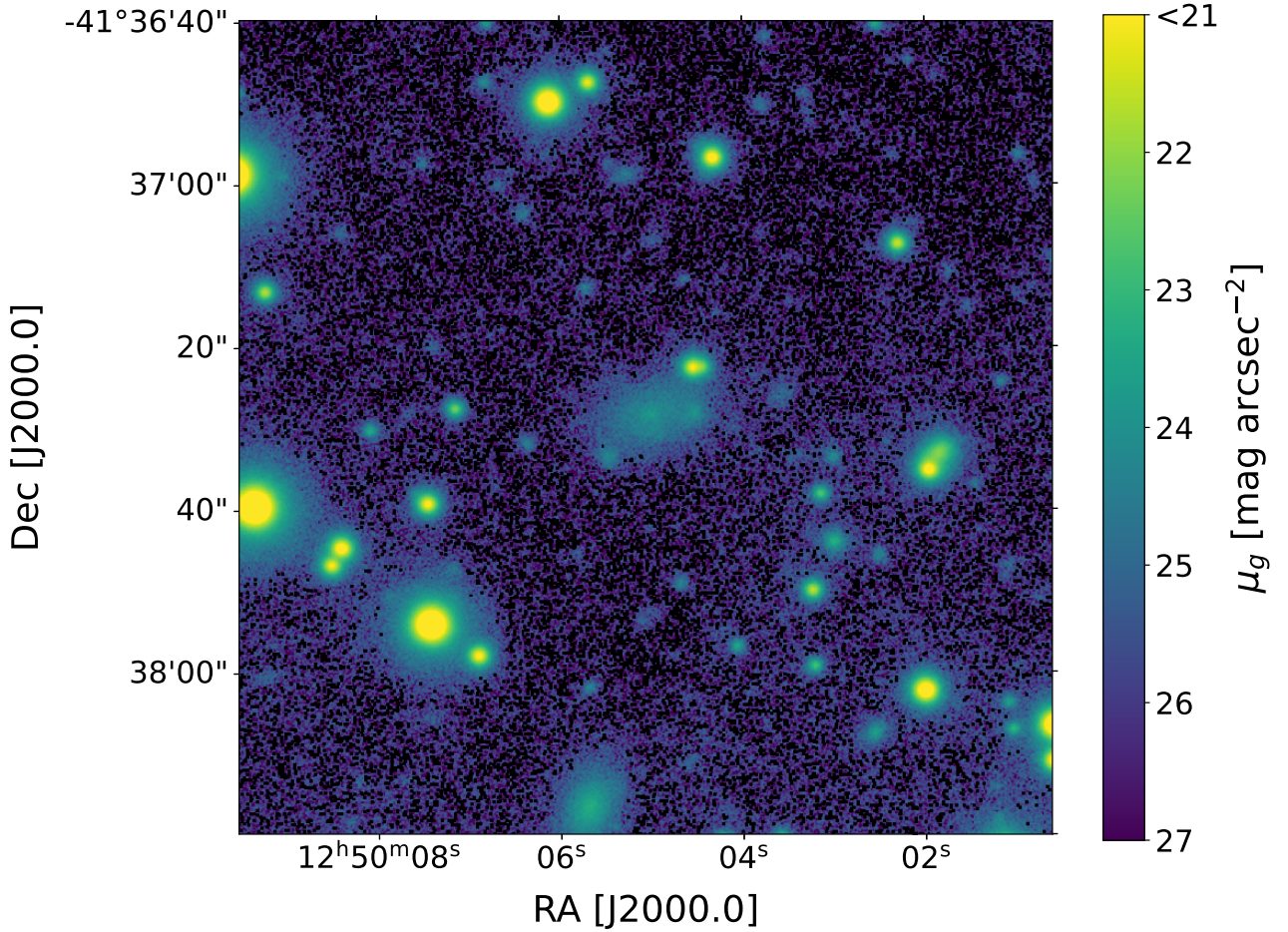
FIGURE 3.1: Example of an LSB galaxy. The galaxy LSB100 is the faint object at the center of the image.

3.1.1   Segmentation map

Image segmentation is a group of algorithms for image processing. The input is the image matrix and the output is a segmentation map, which is a set of sources, called segments, detected by the algorithm.

I first introduce the segmentation map definition and then I describe, from the mathematical point of view, how the adopted image segmentation algorithm works. This specific image segmentation algorithm exploits the pixel intensity to find the edges of each detected source. The algorithm that I use is `detect_sources` of `photutils` and the segmentation map that I describe is an object of `photutils.segmentation`

Let $I_{i,j}$ be the image matrix. The points (i, j) are then the pixel coordinates in the image. Let be $\mathbb{S} = \{s_1, s_2, ..., s_k\}$ a segmentation map made of M s_k segments.

A segment can be viewed as an ensamble of pixels. Then I say that $(i, j) \in s_k$ if the pixel (i, j) is part of the segment. Computationally, a segmentation map is an object. The attribute `data` of the object `SegmentationImage` returns a segmentation matrix $\mathbb{S}_{i,j}$ which is defined as follows:

- it has the same size and shape of $I_{i,j}$;

- $\mathbb{S}_{i,j} = k$ if $(i, j) \in s_k$;

- $\mathbb{S}_{i,j} = 0$ elsewhere.

If pixel (i, j) does not belong to the segmentation map $\mathbb{S}$ it is $\mathbb{S}_{i,j} = 0$. This reasoning works also for the segments. Indeed a segment has the attribute `data` too, which is a matrix similarly defined. So if $(i, j) \notin s_k$,it is $s_{k;i,j} = 0$. I note that in a segmentation map, each pixel (i, j) of the image uniquely belongs to either a single segment or to the background.

Two pixels are connected if they share one edge, so generally, one pixel has eight connected pixels. Let $I_{i\pm1,j\pm1}$

be the set of the eight connected pixels and I_{thr} the intensity threshold over which the pixel is considered part of a source instead of background. A segment is a set of connected pixels for which $I_{i,j} > I_{\text{thr}}$ and $I_{i\pm1,j\pm1} > I_{\text{thr}}$.

The algorithm defines the segments through matrix operations. I describe a more intuitive way to generate the output segment. The input/output files are equivalent to those of the algorithm, but my approach requires a multiple iteration over pixels, which is much slower than matrix operations. Intuitively, once the first pixel in the segment is found, the algorithm tries to see if the connected pixels are also part of the segment. If some of them are, the new connected pixels are also examined iteratively. In the end, the segment will have all the pixels at the edge connected with at least one pixel below I_{thr}, then the segment of the source is completed and the algorithm goes in search for a new segment.

Let A_k be the total number of pixels considered part of the k-segment s_k, thus the total number of connected pixels is:

$$A_k = \sum_{(i,j)\in s_k} 1 \ . \tag{3.1}$$

The segmentation map is the set of M segments, each of them made of A_k pixels, $k = 1, 2, ..., M$. Let N_{conn} be the minimum number of connected pixels in order to consider a segment as a source. The segmentation map includes only segments with $A_k > N_{\text{conn}}$.

I detect LSB galaxies using `photutils.segmentation.detect_sources`[1]. The main input parameters are $I_{i,j}$, which is the VEGAS image of Centaurus cluster in g' band, $N_{\text{conn}} = 600\,\text{pix}$ (0.75 kpc at Centaurus distance), and $I_{\text{thr}} = 2\,\text{ADU}\,\text{pix}^{-1}$. Other available parameters are set to the default options of `photutils` (version 1.5.0). I choose the g'-band image instead of the r' one because it has a more stable background which is a key point for the detection. If the background would be exactly $0\,\text{ADU}\,\text{pix}^{-1}$ everywhere, then the best threshold value would be $I_{\text{thr}} = 0\,\text{ADU}\,\text{pix}^{-1}$. Of course there are sub-regions of the image, where the background is in mean larger/smaller than $0\,\text{ADU}\,\text{pix}^{-1}$ and sub-regions where it is smaller. With the choice of $I_{\text{thr}} = 0\,\text{ADU}\,\text{pix}^{-1}$, all LSB galaxies that have a background value larger than $0\,\text{ADU}\,\text{pix}^{-1}$ would be lost. On the other hand, increasing the threshold value makes A_k decreasing, so increasing the threshold value would also increase the number of objects discarded because $A_k < N_{\text{conn}}$. After several trials, the best compromise in order to maximize the number of LSB galaxies detected is $I_{\text{thr}} = 2\,\text{ADU}\,\text{pix}^{-1}$. To simplify the understanding, I show the segmentation maps of four images for different values of I_{thr} in Fig. 3.2.

Then, I take a single image and I vary both I_{thr} and N_{conn} in Fig. 3.3 in order to justify the choice of $N_{\text{conn}} = 600\,\text{pix}$. Decreasing N_{conn}, the number of segments in the segmentation map increases. For instance, from $N_{\text{conn}} = 10\,\text{pix}$ and $N_{\text{conn}} = 1000\,\text{pix}$ the number of detected segments increases by more than a factor 10. Galaxies are extended objects, so, in principle, one could think that objects that are small enough should be discarded. But the aim is the search of LSB galaxies with a central surface brightness fainter than 23 mag arcsec^{-2} and the adopted threshold value in surface brightness correspond to $I_{\text{thr}} = 2\,\text{ADU}\,\text{pix}^{-1} \simeq 25.4$ mag arcsec^{-2} so N_{conn} should be smaller than the area of the LSB galaxies with surface brightness greater than 25.4 mag arcsec^{-2}. At the same time, N_{conn} cannot be arbitrarily small otherwise the number of segments in the segmentation map would excessively increase and this would lead to an enormous calculus time for the deblending. After several trials, the best compromise in order to maximize the number of detected LSB galaxies keeping a reasonable calculus time turned out to be $N_{\text{conn}} = 600\,\text{pix}$.

3.1.2 Deblending algorithms

The image segmentation algorithm described above, detects both bright and faint objects. As the aim of this thesis is the study of LSB galaxies, I apply a selection criterion based on the maximum surface brightness. Therefore, I extract from the segmentation map only segments having a maximum surface brightness corresponding to $\mu_{\text{max,g}} \in [23.5, 27.0]$ mag arcsec^{-2}. If I do this now I would lose most of the LSB galaxies of the sample. In fact, most of the LSB galaxies in dense environments are superimposed to (or near by) other brighter objects. The detection algorithm based on image segmentation do not distinguish them, so they are considered

---

[1] `https://photutils.readthedocs.io/en/stable/api/photutils.segmentation.detect_sources.html#photutils.segmentation.detect_sources`
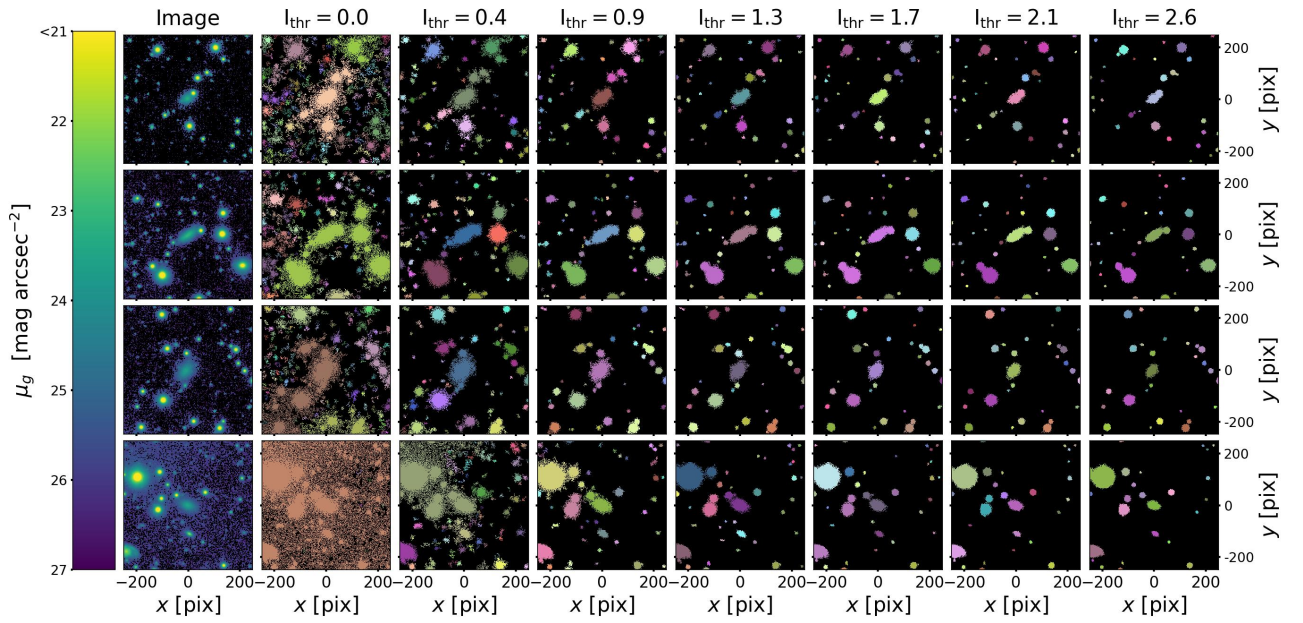
FIGURE 3.2: Detection of four LSB galaxies with different I_{thr} values. The left panels show the images of four LSB galaxies. The other panels are segmentation maps of `detect_sources` according to the input I_{thr} value written at the top. In the segmentation maps different colors are used to highlight different segments.
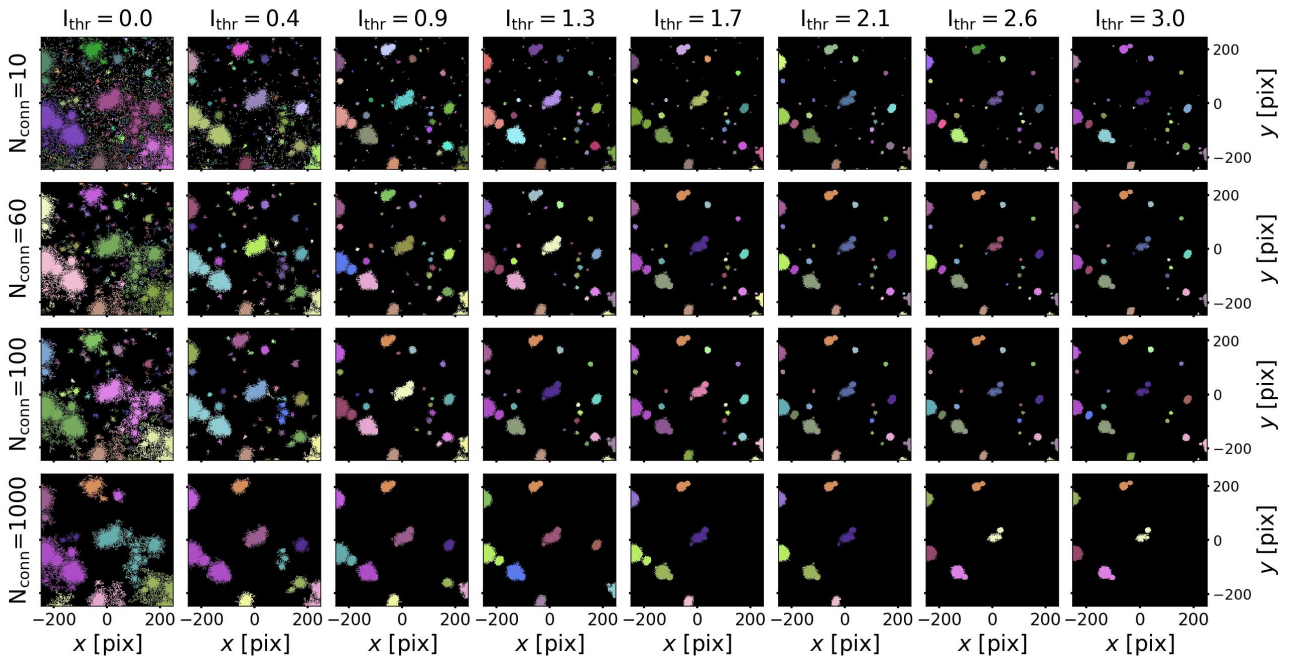
FIGURE 3.3: Detection of LSB100 with different parameters. Each panel of the figure is the segmentation map of `detect_sources` with different N_{conn} and I_{thr}. Different colors are used to highlight different segments.

as a unique source. I show two examples in Fig. 3.4. It is easy to see that the central objects are made by an LSB source and a brighter point like source.

In order to correctly apply the surface brightness selection, first I run a deblending algorithm which is a technique used to separate segments into multiple sub-segments. In a certain sense, deblending could be considered as the segmentation of a segment.

The deblending algorithm that I adopt is `photutils.segmentation.deblend_sources`[2] and it is based on multi-thresholding and watershed segmentation map (Neubert & Protzel 2014)[3]. The input are an image, its

---

[2]`https://photutils.readthedocs.io/en/stable/api/photutils.segmentation.deblend_sources.html`
[3]`https://github.com/scikit-image/scikit-image/blob/v0.19.2/skimage/segmentation/`
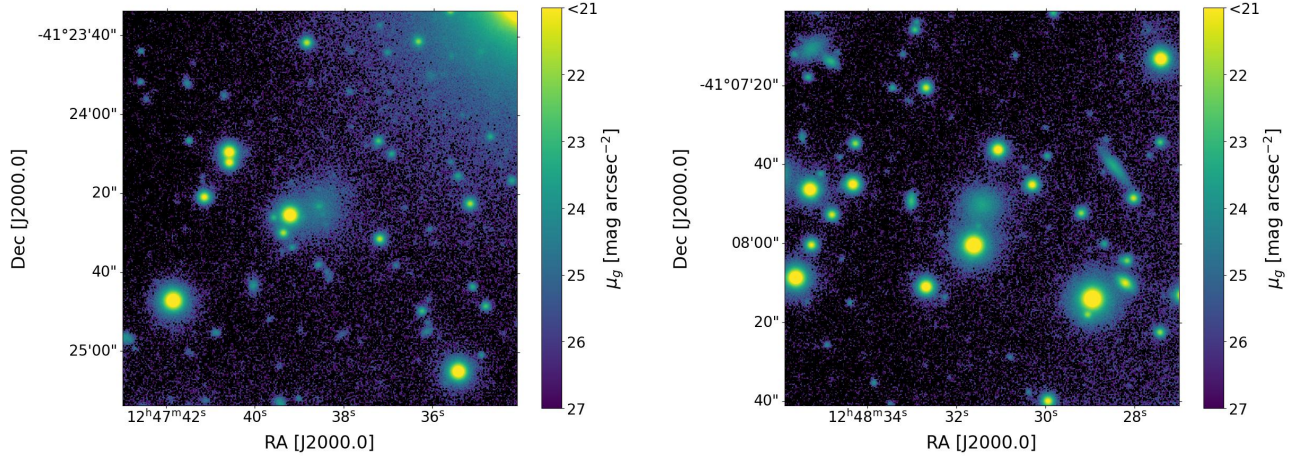
FIGURE 3.4: Examples of LSB galaxies overlapped by brighter sources.
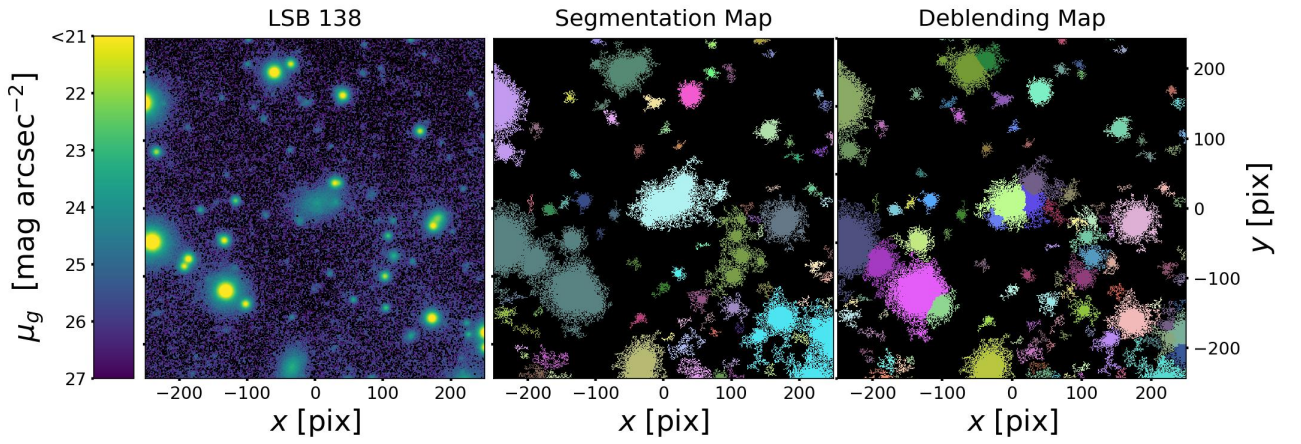
FIGURE 3.5: Detection of LSB100. Left panel: g'-band image of the galaxy LSB100. The black colour is used for bad pixels and for pixels with negative values. Central and right panels: The segmentation and deblending maps with different colors used to highlight different segments.

segmentation map, and a set of parameters that define how to separate sources. The output is a new segmentation map with a larger number of segments than the input one. In Fig. 3.5 I show multiple sources (central panel), which are classified as a single segment by `detect_sources`, disentangled by `deblend_sources` (right panel).

Before the description of `deblend_sources`, I introduce the multi-thresholding and watershed techniques in order to explain how deblending works.

Watershed segmentation map: They are algorithms to segment an image. There are many watershed algorithms and `watershed` from `skimage.segmentation`[3] is implemented in the adopted deblending algorithm. Any gray-scale image can be viewed as a topographic surface where high intensity regions denote peaks whereas low intensity regions denote peaks and hills. We start filling all the isolated peaks (markers) with different color water (different segments). As the water rises, depending on the gradient of the image, water from different peaks starts to merge. To avoid that, we build barriers where water merges. We continue filling water and building barriers until all the valleys are under water. The barriers define the edges of each segment. The main differences between watershed segmentation and `detect_sources` are: i) watershed requires a marker list as input, which can be built from the local maxima of the image; ii) with watershed the whole image domain is covered by segments and there are not void regions; and iii) `detect_sources` defines segments through I_{thr} and N_{conn}, whereas watershed has only the markers as input parameter.

Multi-thresholding This is the core of the adopted deblending algorithm.

23
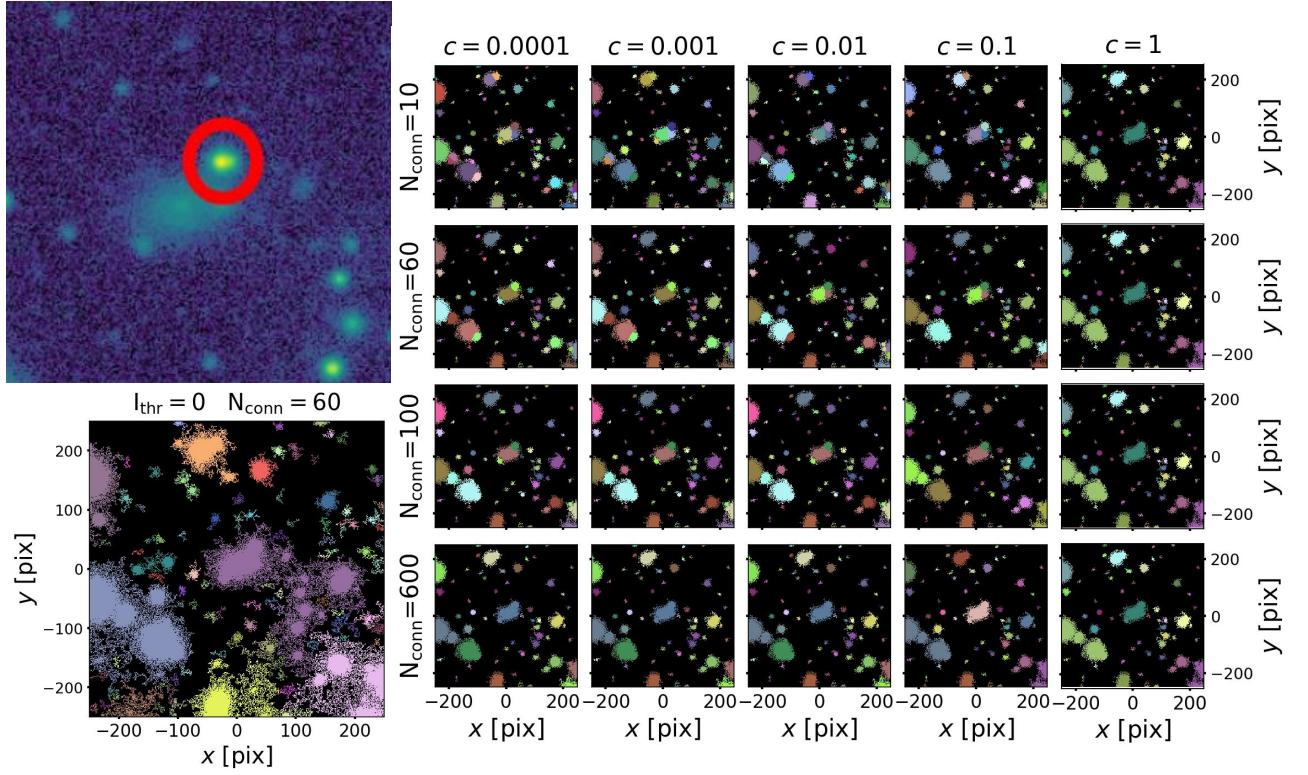
FIGURE 3.6: Detection and deblending with different parameters. Upper-left panel: LSB100. It is the central part of Fig. 3.1. The red circle is the bright source that must be excluded from the LSB segment. Lower-left panel: Segmentation map of LSB100 with $I_{\text{thr}} = 0\,\text{ADU}\,\text{pix}^{-1}$ and $N_{\text{conn}} = 60$. Right panel: Grid of deblended-segmentation maps. Each panel of the grid is obtained with different parameters c and N_{conn} that are reported in the image.

The center of image (COI) of a segment s is the first image moment. Let (x_c, y_c) be the central pixel of the image $I_{i,j}$. It is:

$$COI = \sum_{(i,j) \in s} I_{i,j}(i - x_c, j - y_c) \,.$$

Let I_{max} and I_{min} be the maximum and the minimum value of the image $I_{i,j}$, respectively. If I apply the algorithm `detect_sources` on $I_{i,j}$ with $I_{\text{thr}} = I_{\text{max}}$, then the segmentation map will be void. If otherwise, I apply `detect_sources` on $I_{i,j}$ with $I_{\text{thr}} = I_{\text{min}}$, then the segmentation map will have a single segment that contains the whole image.

Let $I_{\text{thr},n}$, $n = 1, 2, ..., N_{\text{levels}}$ be a set of different thresholds with $I_{\text{thr},n} \in \,]I_{\text{min}}, I_{\text{max}}[$. The idea of multi-thresholding is to first define the brightest sources with an high threshold value and then decrease the threshold to detect iteratively fainter sources. In the `deblend_sources` algorithm, `detect_sources` is applied from the highest to the lowest $I_{\text{thr},n}$. I indicate with the index n the n-th segmentation map output and with the index k the k-th segment of a segmentation map.

For each new detected source (i.e. for each n and each k), the coordinates of the COI are stored in the marker set $m_{k,n}$.

It can be seen in Figs. 3.2 and 3.3 that the brightest sources are always detected even changing $I_{\text{thr},n}$. Hence, there will be duplicates of the same source in $m_{k,n}$. The algorithm removes the duplicates. Let m_j be the marker set without duplicates. It includes all the candidate new sources.

The core of `deblend_sources` is how watershed and multi-thresholding are combined together to give to the algorithm the ability of separating sources. $\mathbb{S} = \{s_1, ..., s_k, ..., s_M\}$ is a segmentation map in the input parameters of `deblend_sources`.

The algorithm iterates over each segment s_k. It means that what follows is applied only to the pixels that belong to s_k. So, for each s_k:

- First, it takes from the set of candidate new sources m_j the markers that belong to s_k and then it uses them as input value of watershed segmentation map. I indicate these new segments as water-segments w_j and watershed-segmentation map as $\mathbb{W}$.

- The output water-segments are iteratively tested: all water-segments with an area $A_j < N_{\text{conn}}$ are discarded and their markers are removed from the set of candidate new sources m_j.

- Let $c_{w_j}^{s_k}$ be the contrast between a segment s_k and a water-segment w_j contained in it. The contrast is calculated as the ratio between the total integrated light of w_j and s_k:

$$c_{w_j}^{s_k} = \frac{\sum_{\vec{x} \in w_j} I(\vec{x})}{\sum_{\vec{x} \in s_j} I(\vec{x})} \ . \tag{3.2}$$

  The contrast value ranges from 0 to 1 because w_j is fully contained in s_k. The contrast $c_{w_j}^{s_k}$ is calculated for each water-segment w_j.

- For each water-segment: if $c_{w_j}^{s_k} < c$, which is an input parameter, then the water-segment is discarded and its marker is removed from the set of candidate new sources.

In summary, there is a segment s_k with a list of coordinates m_j that are candidate sources within s_k. The algorithm iteratively computes the watershed segmentation map and removes the markers from the marker list m_j until both the following conditions are satisfied:

- $A_j < N_{\text{conn}} \quad \forall m_j \in s_k$

- $c_{w_j}^{s_k} > c \qquad \forall w_j \ .$

Then the algorithm moves to the next segment of $\mathbb{S}$.

The water-segment w_j surviving to this process defines the new segmentation map, which is the output of `deblend_sources`.

3.1.3 `deblend_sources` applied to VEGAS data

The main input parameters of `deblend_sources` are the image $I_{i,j}$, its segmentation map, N_{conn}, c, N_{levels}, and `mode`. The last two parameters define how the set of $I_{\text{thr},n}$ is computed. I use the default values $N_{\text{levels}} = 32$ and `mode='exponential'` that define the multi-thresholds as follows:

$$I_{\text{thr},n} = I_{\text{min}} \left(\frac{I_{\text{max}}}{I_{\text{min}}} \right)^{\frac{n}{N_{\text{levels}}+1}} \ . \tag{3.3}$$

I start by applying `deblend_sources` to the whole VEGAS g'-band image and the segmentation map using ARES. It is a supercomputer available at INAF-OACN made of 3 nodes with a total amount of 168 core and 700 Gb of RAM storage. After around 12 hours the algorithm was still running. It is so time consuming because the algorithm defines a huge ensamble m_j of candidate sources and then, when iterates over each segment s_k, it continues to work with m_j searching each time which m_j belongs to s_k. This is the reason why deblending can be applied only to small images in order to have suitable time of calculus.

Therefore, I take the segmentation map and create sub-images for each segment centered on its COI and with a size of 100×100 pixel. Then, I iterate over each segment by applying `deblend_sources` and using as input parameters the sub-image, single segment, $c = 0.001$, and $N_{\text{conn}} = 20$. Other parameters are set to the default options of `photutils` (version 1.5.0).

I note that c and N_{conn} are the parameters that mostly influence the result. I apply `detect_sources` with $N_{\text{conn}} = 600$ and $I_{\text{thr}} = 0 \, \text{ADU pix}^{-1}$ to LSB100. Then I take the output and use it to apply `deblend_sources` with different values of c and N_{conn}. I show the result in the right panel grid of Fig. 3.6.

I choose a smaller value of minimum area $N_{\text{conn}} = 20$ instead of 600 to remove false positives. Consider for instance a false positive region of 600 pixels with values greater than threshold $I_{\text{thr}} = 2 \, \text{ADU pix}^{-1}$, which could

come from a near-by galactic halo or a region where the background is not perfectly subtracted. This would be considered as a unique giant source by both `detct_sources` and `deblend_sources` with $N_{conn} = 600$. If $N_{conn} = 20$, then the markers found by the multi-thresholding process would not be discarded and the false positive giant halo is splitted in many small sub-segments that are removed in the next step. Moreover, keeping small values of N_{conn} allow the bright point-like sources to be deblended from the LSB galaxies. If the LSB galaxy is not deblended (Fig. 3.6 with $N_{conn} = 600$) from the brighter sources, it will be excluded from the sample when I apply the surface brightness selection.

After deblending all the segments, I end up with a list of more than 1000 segmentation maps where each of them is the `deblend_sources` output and then it contains one or more segments.

3.1.4   Preliminary catalog of sources

Resuming previous passages: I apply `detect_sources` (Sec. 3.1) to the VEGAS image and then I apply `deblend_sources` (Secs. 3.1.2 and 3.1.3) to each segment obtaining a list of deblended-segmentation maps. In each deblended-segmentation map I inspect the sample by keeping only the deblended-segments having a maximum surface brightness corresponding to $\mu_{max,g} \in [23.5, 27.0]$ mag arcsec^{-2} and containing at least 400 connected pixels. After rejection, some deblended-segmentation maps contain 0 deblended-segments. This is the case of false positive (Sec. 3.1.3). All the other deblended-segmentation maps contain one or more deblended-segments. LSB galxies are detected by `detect_sources`, whereas `deblend_sources` is fundamental to exclude spurious sources. If after rejection some deblended-segmentation maps contain more than a deblended-segment, it means that the LSB source is divided in multiple deblended-segments (Fig. 3.6). Thus for each deblended-segmentation map that after rejection contains at least one deblended-segment I take the original segment used for deblending. I compute the COI of the segment and I save a 500×500 pixel thumbnail (18×18 kpc^2 at Centaurus distance) in `.fits` format. I write the header of each thumbnail by modifying the header of the VEGAS image. I also store the coordinates of each source in a file. The Fig. 3.1 is an example of these thumbnails.

3.1.5   Visual inspection catalog

Before developing the tool for automatic detection, I begin by looking by eye the VEGAS images to understand the morphology of LSB features in a cluster environment. With DS9 software for image visualization, I set a logarithmic scale between $0\,\text{ADU}\,\text{pix}^{-1}$ and $20\,\text{ADU}\,\text{pix}^{-1}$ and I search for LSB galaxies, in particular for UDGs.

I check the already discovered UDGs at the VEGAS images of Hydra I cluster (Iodice et al. 2020a; La Marca et al. 2022a) to train myself in the morphological identification of a UDG. I save the coordinates of each candidate LSB galaxy and I compile a catalog of 387 candidates for which I save a thumbnail as done for the automatically detected ones.

Finally, I stack the catalog with the visually identified and automatically detected LSB galaxies. I cross match the two catalogs before stacking to avoid duplications and considering a range of 5 arcsec. I end up with a final catalog of 546 thumbnails of LSB galaxies ready to be analysed.

3.2   Cluster membership

The faintest galaxies discovered in the new imaging surveys usually lack accurate distance information, and many of them have such a low surface brightness that obtaining spectroscopic redshifts for a complete sample is not possible with the available instruments. Thus, to assess the cluster memberships of very faint objects, one needs to exploit their photometric properties. One possibility is to address cluster memberships using the known scaling relations for galaxies. In fact, in clusters there are up to thousands of galaxies located at a similar distance, and many of their properties scale with each other. On the other hand, background galaxies are spread over a wide range of distances, so their apparent parameters do not follow any relation. Useful relations commonly used for identifying cluster members are the color-magnitude and the magnitude-surface brightness relations (e.g., Misgeld et al. 2009; La Marca et al. 2022b). Already the work by Binggeli et al. (1985) have
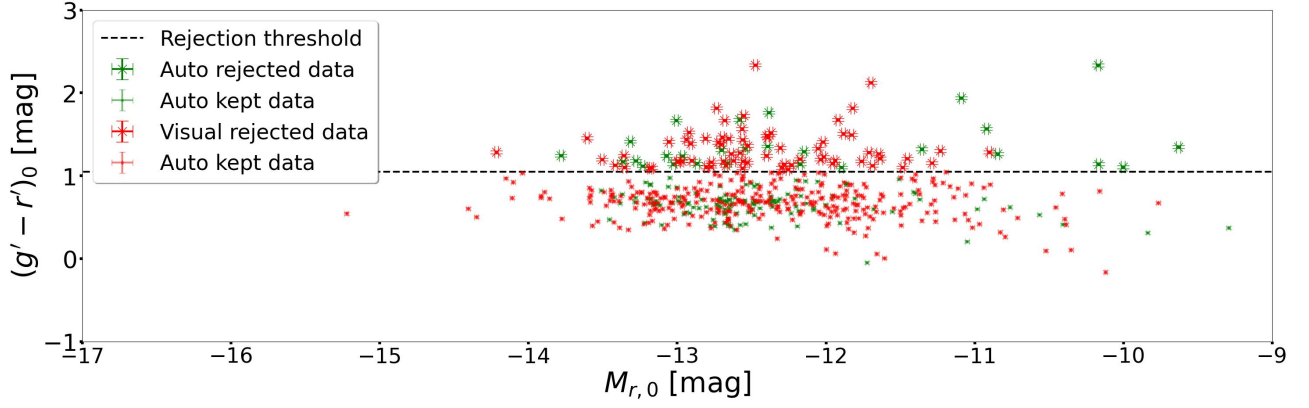
FIGURE 3.7: Colour-magnitude diagram of the candidate LSB galaxies. The visually identified (red points) and automatically detected (green points) galaxies are shown with the rejection threshold (dashed black line). All the galaxies redder than $(g' - r')_0 = 1.05$ mag (crosses) are excluded from the sample.

used colors, the luminosity-surface brightness relation and galaxy morphology to define the membership status in the Virgo cluster. More recently, Venhola et al. (2018, 2019, 2022) have used these scaling relations to construct the FDS dwarf galaxy catalog for the Fornax cluster.

To study LSB galaxies in cluster environment, I apply a color selection to exclude LSB objects that are more distant from us with respect to the Centaurus cluster.

For each source of the catalog, I compute the magnitudes in g' and r' bands integrating the surface brightness within a circular area of $r_{\rm cir} = 25$ pix and subtracting the contribute of the sky ($I_{g,\rm sky}$) integrating the surface brightness within circular annulus of $r_{\rm in} = 25$ pix and $r_{\rm out} = 30$ pix:

$$
\begin{aligned}
g'_0 &= -2.5 \log \left(I_g - I_{g,\rm sky} \right) + zp_g - A_g \\
r'_0 &= -2.5 \log \left(I_r - I_{r,\rm sky} \right) + zp_g - A_g \\
zp_g &= 29.940 \pm 0.008 \, \text{mag} \\
A_g &= 0.368 \pm 0.010 \, \text{mag} \\
zp_r &= 29.890 \pm 0.005 \, \text{mag} \\
A_r &= 0.255 \pm 0.010 \, \text{mag}
\end{aligned}
\tag{3.4}
$$

where zp_g and zp_r are the zero point calculated by VEGAS team in the g' and r' bands, respectively, and A_g and A_r are the corresponding Galactic absorption coefficients (Schlafly & Finkbeiner 2011). I assume a constant value of the Galactic absorption coefficients in the whole FoV, corresponding to the value at NGC 4696 position. I compute the error on the magnitude in g' band as follows:

$$
\sigma_{g'_0} = \sqrt{ \left(\frac{2.5}{\ln(10)} \right)^2 \left[\left(\frac{\sigma_{I_g}}{I_g - I_{g,\rm sky}} \right)^2 + \left(\frac{\sigma_{I_{g,\rm sky}}}{I_g - I_{g,\rm sky}} \right)^2 \right] + \sigma_{zp_g}^2 + \sigma_{A_g}^2 }
\tag{3.5}
$$

where I assume σ_{I_g} to be the Poissonian error on the counts, whereas I assume $I_{g,\rm sky} = 0.5 \, \text{ADU pix}^{-1}$, which is the typical background oscillation observed at the limiting radius (see Sec. 3.3.2). I also compute the error on the magnitude in r' band using Eq. (3.15).

To compute the magnitudes I use the `IRAF` task `apphot`[4]. The BCG NGC 4696 has a color $(g' - r')_0 = 0.778 \pm 0.026$ mag (Misgeld et al. 2009 converted with Eq. 4.1). I exclude all the sources redder than 1.05 mag by assuming that their redness is due to the cosmological redshift effect (Fig. 3.7). Doing so, I am mostly ruling out the large background ETGs and spirals, as their intrinsic color could be similar to the largest cluster members, but their apparent color is significantly redder due to the higher redshift. However, some background spirals with a small or no bulge will be still left in the sample.

---

[4]https://iraf.net/irafdocs/apuser.ps.gz

FIGURE 3.8: Masking spurious sources. Left panel: 500×500 pixel thumbnail of LSB100. Central panel: Segmentation map of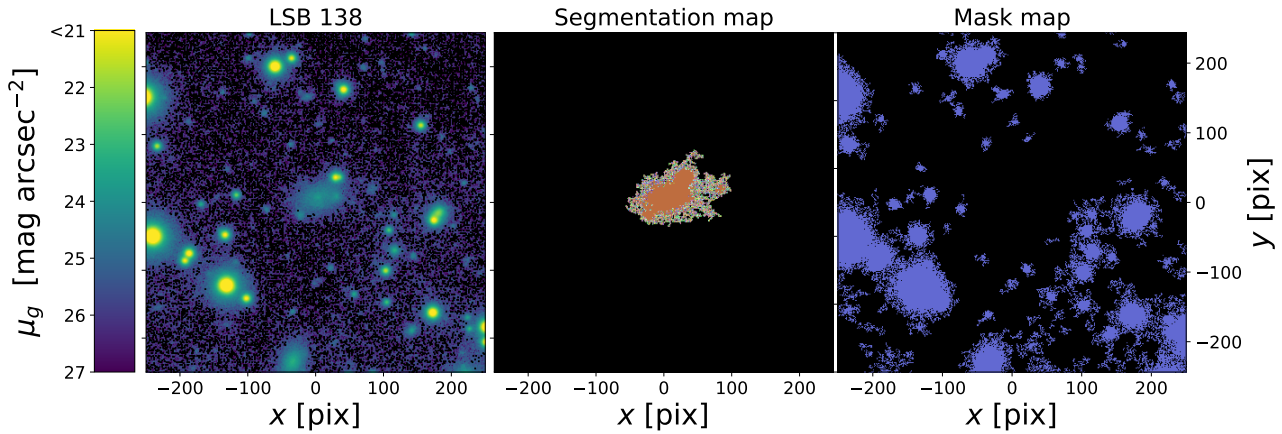 the candidate LSB galaxy. Right panel: Segmentation map of the mask. The purple pixels are masked with a Boolean array.

3.2.1 Masking spurious sources

It is fundamental to mask spurious sources in order to correctly measure the surface brightness distribution of LSB galaxies. This step is crucial due to their LSB nature of the targets and if it is not correctly performed, the analysis tool that I use fails at the step described in Sec. 3.3.2.

I repeat the detection of the LSB sources in all the 500×500 pixel thumbnails with `detect_sources` and starting from $N_{\mathrm{conn}} = 60$ and $I_{\mathrm{thr}} = 0\,\mathrm{ADU\,pix}^{-1}$. The aims of this step are to mask spurious sources and to create a segment of the LSB galaxies which also contains their outskirts. In Fig. 3.2 I note that there is not a unique value of input parameters that for all 4 images gives the segment of the LSB central source with its outskirts and, at the same time, not blended with other sources.

Semi-automatic tool for masking I develop a semi-automatic tool for masking to produce the best possible segment and best mask for each LSB source. The tool iteratively displays images like the one shown in Fig. 3.8 and the user can decide if accept or change it again. There are two things that the user can change: i) I_{thr} to correctly include the outskirts; ii) activate `deblend_sources` to the LSB segment with $N_{\mathrm{conn}} = 60$ and the other input parameters as in Sec. 3.1.3 in order to remove from the LSB segment the spurious sources. After each change of the parameters, the tool displays again the result asking the user to accept or change again. Once accepted, the tool automatically applies the Boolean mask to all the pixels associated with a segment having the COI beyond 100 pix from the center of the image (i.e. which is not the candidate LSB galaxy). I choose to not include in the mask sources inner than 100 pix because these are excluded by the fitting algorithm in Sec. 3.3.2 using a sigma-clipping algorithm. I note that it is fundamental that the mask is Boolean. Some masking tools substitute the value of $0\,\mathrm{ADU\,pix}^{-1}$ to each pixel of the mask, but this changes the statistics and the change is significative in the LSB regime. A Boolean mask, instead, is an array with the same size of the image and with values `True` or `False`. I work with `numpy` package (Harris et al. 2020), which is the state-of-the-art for array operations in `python`. `numpy` implements the possibility to work with masked arrays which are the superposition of an array and a mask. Hereafter each image operation is done with masked arrays, thus before any operation the image array is multiplied by the Boolean mask.

Once the user has set the best parameters for the mask, the semi-automatic tool applies the analysis of Secs. 3.3.1 and 3.3.2 and then it switches to the successive thumbnail of the catalog.

Sigma-cliping Given a set of data, sigma-clipping is a technique used to remove outliers. I use sigma-clipping to exclude bright sources from the surface brightness models of the LSB galaxies. In particular, all the bright sources within 100 pix that are not excluded by the mask. Consider a set of data $x_{j,0}$ with mean $\langle x \rangle_0$ and standard deviation σ_0. Let $x_{j,1}$ be the sub-sample $x_{j,0} \in \left[\langle x \rangle_0 - n_{\mathrm{clip},-} \cdot \sigma_0, \langle x \rangle_0 + n_{\mathrm{clip},+} \cdot \sigma_0 \right]$ with its new mean $\langle x \rangle_1$, and standard deviation σ_1. The sigma-clipping of a set of data is an iterative algorithm that takes as input $x_{j,0}$, $n_{\mathrm{clip},-}$, $n_{\mathrm{clip},+}$ and n_{it}; and it gives back $x_{j,n_{\mathrm{it}}}$ as output.

3.3 Surface brightness profile models

Once identified the LSB galaxies and properly masked the spurious sources, I measure the physical properties of the galaxies, in particular their size, concentration, surface brightness and total luminosity. In principle, one could think that a two-dimensional (2D) model is better than a one-dimensional (1D) one to describe the surface brightness distribution. With a low S/N a 2D model does not properly fit the outskirts of the galaxy and it underestimates its size. Considering that the typical background oscillations are about 0.5 ADU pix^{-1} = 26 mag arcsec^{-2} and I measure surface brightness profiles with a reasonable error up to 0.07 ADU pix^{-1} = 29 mag arcsec^{-2}, it is impossible to apply an accurate 2D model with such a background. In addition, the isophotes of galaxies twist. It means that a galaxy has not elliptical symmetry. Then, for each fitted isophote one should measure the position angle which can change from an isophote to another. The necessity to reproduce the asymmetric surface brightness profile of LSB galaxies (2D model) is apparently incompatible with the necessity to have sufficiently high S/N to reach the depth of 29 mag arcsec^{-2} (1D model).

I develop an automatic tool to model the light profiles of the LSB galaxies that takes into account for 2D asymmetries and that is sufficiently precise to reach the depth of 29 mag arcsec^{-2}. I do it in more steps: first I fits a 2D Sérsic profile, then I use the results to constrain an isophote fit and finally I average the isophotes over the azimuthal angle to obtain 1D surface brightness profile to be fitted.

3.3.1 2D-Sérsic fit

I use the `python` package `statmorph`[5] (Rodriguez-Gomez et al. 2019, 2022) to fit the surface brightness distribution of the galaxies with a 2D-Sérsic model (Sérsic 1968) with elliptical isophotes:

$$
\begin{aligned}
I(x,y) &= I_e \exp\left\{-b_n\left[(z)^{1/n} - 1\right]\right\} \\
z &= \sqrt{\left(\frac{x_{\mathrm{maj}}}{a}\right)^2 + \left(\frac{x_{\mathrm{min}}}{a(1-e)}\right)^2}, \\
x_{\mathrm{maj}} &= (x - x_{\mathrm{2D}})\cos(PA_{\mathrm{2D}}) + (y - y_{\mathrm{2D}})\sin(PA_{\mathrm{2D}}), \\
x_{\mathrm{min}} &= (x - x_{\mathrm{2D}})\sin(PA_{\mathrm{2D}}) + (y - y_{\mathrm{2D}})\cos(PA_{\mathrm{2D}}).
\end{aligned}
\tag{3.6}
$$

where $r_{\mathrm{e,2D}}$ is the semi-major axis of the ellipse that encloses half of the total luminosity, I_e is the surface brightness at the effective radius $r_{\mathrm{e,2D}}$, e_{2D} is the ellipticity, $(x,y)_{\mathrm{2D}}$ the center, PA_{2D} the position angle of the ellipse with respect to x axis evaluated towards the positive direction of y axis, and b_n is the parameter such that R_e encloses half of the total luminosity. b_n is defined as follows:

$$
\begin{aligned}
\Gamma(2n) &= 2\gamma(2n, b_n) \\
\Gamma(2n) &= \int_0^\infty t^{2n-1-t}\mathrm{d}t \\
2\gamma(2n, b_n) &= \int_0^{b_n} t^{2n-1-t}\mathrm{d}t \quad .
\end{aligned}
\tag{3.7}
$$

An approximate solution for b_n, which is valid for $0.5 < n < 10$ is (Ciotti 1991):

$$
b_n = 1.9992n - 0.3271 \quad .
\tag{3.8}
$$

The fitting algorithm computes b_n integrating numerically Eq. (3.7) with `scipy.special.gammainc` (Virtanen et al. 2020). The parameters I_e, $r_{\mathrm{e,2D}}$, n, e_{2D}, $(x,y)_{\mathrm{2D}}$, PA_{2D}, and a are computed with the Levenberg-Marquardt method (Calamai & Moré 1987). It is used to solve non-linear least squares problems and it is implemented in the function `statmorph.source_morphology` from `astropy python` package. I show an example of the fitting result in Fig. 3.9. For each segment (Sec. 3.2.1), the main input parameters of `source_morphology` are the masked image, segment, gain which is used to convert ADU in electron counts in order to have the correct estimation of the Poissonian error. All other parameters are set to the default value (version 0.4.0). The output is a `SourceMorphology` object, which contain a lot of information. First of all the galaxy structural parameters

---

[5]`https://statmorph.readthedocs.io/en/latest/`
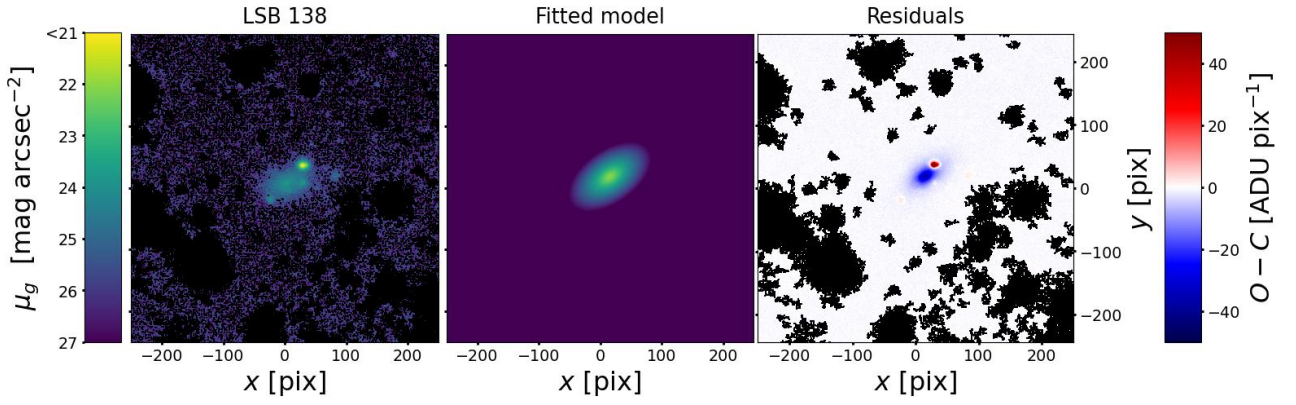
FIGURE 3.9: 2D-Sérsic fit. From left to right: image, model, and residuals. The black pixels are those excluded by the Boolean mask. In the left panel black pixels are also those having negative counts.

I_e, $r_{e,2D}$, and n and the other parameters of the 2D model e_{2D}, $(x, y)_{2D}$, and PA_{2D}. There are also other relevant parameters of the galaxy such as the radii that contain the 20%, 50% and 80% of the total light namely r_{20}, r_{50}, and r_{80} respectively and others. There is also a value of the sky background which is estimated in a small box located in the corner of the image.

3.3.2   Isophotal analysis

I perform the isophotal analysis with the `python` task `photutils.isophote.Ellipse.fit_image`[6], which fits ellipses to the isophotes as described by Jedrzejewski (1987).

Isophote model   Let (R, θ) be a reference frame described in polar coordinates centered in (x_0, y_0) and with position angle PA with respect to the cartesian coordinates (x, y). An ellipse in polar coordinates (R, θ) is described by the function:

$$R_{\text{ell}}(\theta) = a \sqrt{\frac{1 - e^2}{1 - [1 - (1 - e)^2] \cos^2 \theta}} \tag{3.9}$$

where e is the ellipticity, and a the semi-major axis of the ellipse. Let $R_{\text{isof}}(\theta)$ be the isophote in polar coordinates. It is possible to describe the deviations from perfect elliptical shape of the isophotes through Fourier expansion:

$$\delta(\theta) = R_{\text{ell}}(\theta) - R_{\text{isof}}(\theta) = A_0 + \sum_{n=1}^{\infty} A_n \cos(n\theta) + \sum_{n=1}^{\infty} B_n \sin(n\theta) \tag{3.10}$$

where A_n and B_n are the harmonic amplitude that describe deviations from perfect elliptical shape and can be computed exactly by solving the integrals:

$$A_n = \frac{1}{\pi} \int_0^{2\pi} \delta(\theta) \cos(n\theta) \mathrm{d}\theta$$
$$B_n = \frac{1}{\pi} \int_0^{2\pi} \delta(\theta) \sin(n\theta) \mathrm{d}\theta \ . \tag{3.11}$$

Suppose that all harmonics are zero except one. Up to $n = 2$ the shape of the isophote is still an ellipse and each harmonic correspond to a deviation of a single parameter of the ellipse:

- (A_1, B_1) correspond to the center coordinates (x, y);

- A_2 corresponds to the ellipticity;

- B_2 corresponds to the PA;

- A_0 corresponds to a.

If larger harmonics are different from zero the isophote is not anymore a perfect ellipse.

---

[6]`https://photutils.readthedocs.io/en/stable/api/photutils.isophote.Ellipse.html`

First isophote to fit   The first isophote to be fitted can not be too inner (due to bad sampling) or too outer (due to low S/N), but something in between. I use $r_{e,2D}$, e_{2D}, and PA_{2D} from the 2D-Sérsic fit to define the first ellipse (white circle in Fig. 3.10) to be fitted. Using these values, the image is sampled[7] along the elliptical path, producing a 1D function that describes the dependence of surface brightness with azimuthal angle (θ). The function is stored as a 1D `numpy` array. The function is analyzed by least-squares fitting to the function:

$$\delta(\theta) = A_0 + A_1 \sin(\theta) + B_1 \cos(\theta) + A_2 \sin(2\theta) + B_2 \cos(2\theta) \tag{3.12}$$

Each one of the harmonic amplitudes (A_1, B_1, A_2, and B_2) is related to a specific ellipse geometric parameter. The algorithm selects the largest amplitude, computes the corresponding increment in the associated ellipse parameter (center, ellipticity, and position angle) which is updated, and the image is resampled. The fitting algorithm computes A_1, B_1, A_2, and B_2 and resamples the image until any one of the following criterion is met:

1. the largest harmonic amplitude is less than a given fraction of the rms residual of the surface brightness around the harmonic fit;

2. a user-specified maximum number (`maxit`) of iterations is reached;

3. more than a given fraction of the elliptical sample points have no valid data in then, either because they lie outside the image boundaries or because they were flagged out from the fit by sigma-clipping.

In any case, a minimum number (`minit`) of iterations is always performed. If iterations stop because of reasons 2 or 3 above, then those ellipse parameters that generated the lowest absolute values for harmonic amplitudes will be used.

At this point, the image data sample coming from the best-fitting ellipse is analyzed twice by least-squares fitting to the functions:

$$\delta(\theta) = A_0 + A_3 \sin(3\theta) + B_3 \cos(3\theta)$$
$$\delta(\theta) = A_0 + A_4 \sin(4\theta) + B_4 \cos(4\theta) \ . \tag{3.13}$$

The amplitudes A_3, B_3, A_4, and B_4, measure the isophote deviations from perfect elliptical shape. These amplitudes, divided by the semi-major axis are called a_3, b_3, a_4, and b_4 and are part of the output of the algorithm.

Once defined the shape of the isophote, the algorithm then measures the integrated intensity and the number of non-flagged pixels inside the elliptical isophote and inside the corresponding circle with same center and radius equal to the semi-major axis length. These parameters, their errors, other associated parameters, and auxiliary information are part of the output.

Errors in surface brightness and local gradient are obtained directly from the rms scatter of surface brightness data along the fitted ellipse. Ellipse geometry errors are obtained from the errors in the coefficients of the first and second simultaneous harmonic fit. Third and fourth harmonic amplitude errors are obtained in the same way, but only after the first and second harmonics are subtracted from the raw data. The error analysis of this algorithm comes from Busko (1996).

Algorithm of the isophotal analysis   After fitting the first isophote starting from user defined values, the semi-major axis length (*sma*) is incremented following a pre-defined rule. At each step, the starting ellipse parameters are taken from the previously fitted ellipse that has the closest *sma* length to the current one. In low surface brightness regions at large radii, the small values of the image radial gradient can induce large corrections and meaningless values for the ellipse parameters. The algorithm stops increasing the semi-major axis either when *sma* = `maxsma` or when the fitting algorithm fails in the fit of two consecutive isophotes (see fit quality below). Once reached the galaxy outskirt, the algorithm restarts from the first isophote fitted and this time decreases the *sma* leght until it reaches *sma* = `minsma`. `minsma`=0 pix and `maxsma`= None are the default values of these input parameters.

---

[7]The sampling is performed by `photutils.isophote.EllipseSample` using a bilinear integration.

The fitting algorithm provides a sigma clipping algorithm for cleaning deviant sample points at each isophote, thus improving convergence stability against any non-elliptical structure such as stars, spiral arms, HII regions, image defects, etc.

fit_image i/o   I adopt the following input parameters:

- `sma0`: the starting ellipse of the first isophote to be fitted, which is defined by $r_{e,2D}$, e_{2D}, PA_{2D}, and $(x, y)_{2D}$;

- `minsma`= 0 pix and `maxsma`= 250 pix;

- `nclip`= 6 and `sclip`=3.0 which following the notation of Sec. 3.2.1 mean $n_{clip,-} = n_{clip,+} = 3$ and $n_{it} = 6$, respectively;

- all other parameters are left to the default option;

- `fix_center`=variable: I discuss this issue in the next paragraph.

The main output parameters are *sma*, surface brightness *I*, ellipticity *e*, center (x, y), position angle *PA*, $a_{3,4}$ and $b_{3,4}$ Fourier coefficients for the deviations from elliptical shape, and a flag to address if the fit quality is good or not. Except for *sma*, which is analytically computed from the input parameters, all other quantities are the result of a fit and they also have an error which is given as output. These errors on the fit provided by the fitting algorithm itself are calculated via Monte Carlo simulation (Busko 1996). Finally, the output of `fit_image` are the radial profiles of all these quantities. I show in Fig. 3.11 the fitting result and in Fig. 3.12 the radial profile of *e* and *PA*.

Note that both the fitting algorithm and the error estimates are implemented in an `IRAF` task which is called `stsdas.analysis.isphote.ellipse` and the `python` version that I use is very similar to it.

fix_center issue   The algorithm implements the possibility to fix some quantities to the value defined by `sma0`. These parameters are *e*, (x, y), and *PA* and can be fixed by setting the input parameter `fix_quantity=True`. Even if the default values of these three quantities are `False`, the algorithm exploits this option anyway. When for example the S/N is low at large *sma*, the algorithm fixes all the three parameters in order to continue measuring the surface brightness profile. There are cases in which `fit_image` works only if the center is fixed. On the contrary, there are cases in which `fit_image` fails if the center is fixed but works if the center is free to vary. The reason why this happens is that the fitting algorithm has no way to compute the center of the galaxy. In fact, it is given as input parameter from `sma0`. Sometimes the computed center is not correct so the algorithm needs `fix_center=False` in order to adjust it through Fourier analysis. In other cases, when the S/N is low, if the center is left free to vary, the minimization algorithm fails because it has too many free parameters to compute.

In this thesis I set `fix_center=False` and, if `fit_image` fails, I make a second try with `fix_center=True`.

Fit quality   In the analysis of each isophote, the minimization can give as output "not a number" (NaN) to all parameters. This condition occur if one of the following condition is verified:

- the number of masked pixels exceed the 70% of the total number of sampled points;

- the error is too large in the minimization. The exact threshold value is constructed from the input parameter `maxgerr`.

If this happens when fitting the first isophote, the algorithm stops and the entire isophotal analysis fails. For this reason, the success of the algorithm is closely related to the input parameter `sma0` that I compute with the 2D-Sérsic fit.

The S/N decreases, increasing the *sma* length. At some point, the algorithm does not distinguish the galaxy from the sky and the output is a NaN for all parameters. If a NaN occurs in the isophotal analysis, the algorithm does not stop immediately. There are different things that the algorithm tries to do in order to push further the analysis:

- first, it tries to fit the successive isophote to see if it is just a local problem. This is for example the case of HII-like regions in the galaxy which introduce a local fluctuation;

- if it is not a local problem, the parameters e, PA, and (x, y) are fixed to the value of the nearest isophote which was successfully fitted;

- if the above conditions have been already tried and the algorithm continues to fail, then the algorithm stops to increase *sma*.

For this reason, the surface brightness profile $I(sma)$ has some NaN at large *sma*. I define the limit radius R_{lim} as the first *sma* with a NaN value of $I(sma)$ and I exclude all the isophotes at $sma > R_{\text{lim}}$.

sma0 issue This fit is extremely precise and accurate, but it is very sensible to the initial parameters, in particular to the first isophote to be fitted defined by `sma0` input parameter. In most cases I define it with $r_{e,2D}$, e_{2D}, PA_{2D}, and $(x, y)_{2D}$. After several trials, I note that do not exist a universal choice to define `sma0` for all the LSB galaxies. `Statmorph` package provides a flag as output which is 0 if the fit is good and 1 if it is bad. I define `sma0` with e_{2D}, PA_{2D}, $(x, y)_{2D}$, and the semi-major axis of the ellipse in the following way:

- if flag=0: $r_{e,2D}$;

- if flag=1: the minimum between $r_{e,2D}$ and r_{80}.

After several trials to construct a `sma0` from the output parameters of `statmorph` I note that this choice minimizes the number of galaxies for which the algorithm fails.

Overlapping sources In some even worse cases the LSB galaxy is overlapped with some other source (Fig. 3.4). I prefer to exclude these cases because the automated analysis fails.

Before excluding them I tried to do, without success, the following things:

- First, I realize that there is no way to fit them without excluding the bright source.

- Masking them with the segmentation maps. This does not work because this procedure removes too many pixels from the LSB galaxy and the first isophote fit fails.

- Using the sigma-clipping in the isophotal analysis. This does not work for the same reason. I note that sigma-clipping is a very powerful technique, but it works only with small objects such as the GCs.

- Making a catalogue of sources inside the masked image and subtract the spurious ones. After subtraction the isophotal analysis does not fail. So apparently this works and can be implemented in the automated analysis. I do not include this in the analysis and I prefer to exclude these overlapping cases because it is a very delicate procedure. If it is not performed correctly it can change the background level and the measured properties of the LSB galaxy. So I do not include the subtraction of spurious sources in this thesis in order to not include a unconstrained source of systematic error in the data.

3.3.3 1D-Sérsic fit

Before fitting I compute the I_{sky} level on $I(sma)$ knowing that at large radii the profile has a plateau. Thus the I_{sky} is the value such that the plateau at large radii of $I(sma) - I_{\text{sky}}$ has a value compatible with $0\,\text{ADU}\,\text{pix}^{-1}$. The plateau has fluctuations due to the sum of the background and some residual sources. In addition, $I(sma) \geq 0\,\text{ADU}\,\text{pix}^{-1}$ because `fit_image` is tuned to substitute NaN to all negative values of $I(sma)$.

The surface brightness radial profile then has fluctuation that are not symmetric and the method that I use to compute the sky takes it into account. The aim is to keep only points in $I(sma)$ associated with the background fluctuation. I compute the $I_{\text{sky}} \pm \sigma_{I_{\text{sky}}}$ as the mean and standard deviation of $I(sma)$ at $sma \in [r_{80}, R_{\text{lim}}]$ with an asymmetric sigma-clipping ($n_{\text{clip},-} = 0$, $n_{\text{clip},+} = 1$ and $n_{\text{it}} = 300$). This atypical number of $n_{\text{it}} = 300$ iterations assure to remove all the sources from the background level and then assure to have a reliable I_{sky} estimate.
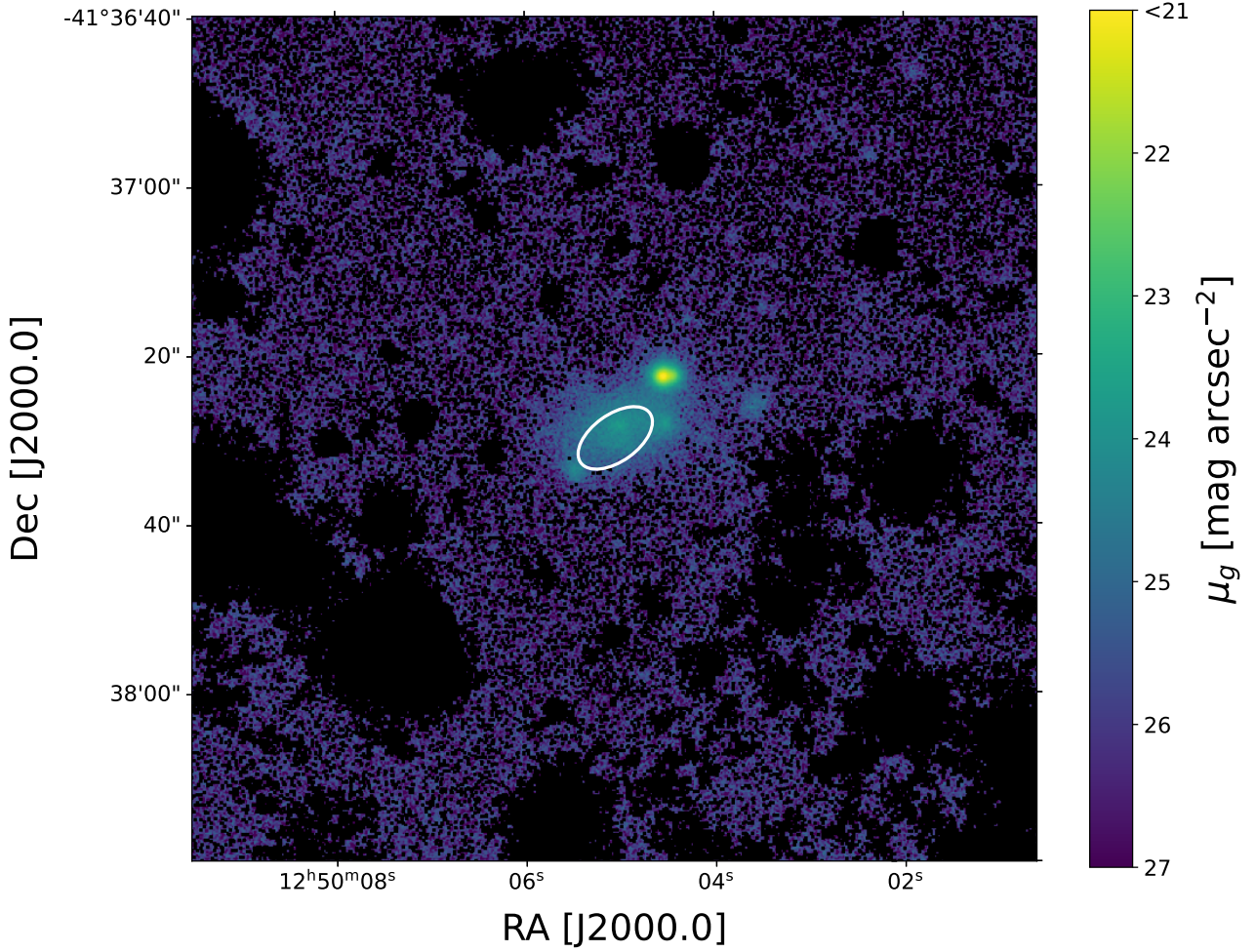
FIGURE 3.10: Starting ellipse of the isophotal analysis of LSB100. The ellipse defined by the input parameter `sma0` is shown in white.

I convert $I(sma)$ from ADU pix^{-1} into mag arcsec^{-2} as follows:

$$\mu_g(sma) = -2.5 \log_{10}((I(sma) - I_{sky})/scale) + zp_g - A_g$$
$$scale = 0.20 \text{ arcsec pix}^{-1}$$
$$zp_g = 29.940 \pm 0.008 \text{ mag}$$
$$A_g = 0.368 \pm 0.010 \text{ mag}$$

$$(3.14)$$

where $scale$ is the angular scale stored in the header, zp_g is the zero point calculated by VEGAS team, and A_g is the Galactic absorption in g' band calculated by Schlafly & Finkbeiner (2011).

I obtain the error $\sigma_{\mu_g}(sma)$ associated to $\mu_g(sma)$ by taking into account for the errors of each quantity.

$$\sigma_{\mu_g}(sma) = \sqrt{\left(\frac{2.5}{\ln(10)}\right)^2 \left[\left(\frac{\sigma_{I(sma)}}{I(sma) - I_{sky}}\right)^2 + \left(\frac{\sigma_{Isky}}{I(sma) - I_{sky}}\right)^2\right] + \sigma_{zp_g}^2 + \sigma_{A_g}^2} \ . \qquad (3.15)$$

Finally, I fit the surface brightness radial profile $I(sma)$ with a 1D-Sérsic model. The Sérsic model is a surface brightness profile:

$$I(r) = I_e \exp\left\{-b_n \left[\left(\frac{R}{R_e}\right)^{1/n} - 1\right]\right\} \ . \qquad (3.16)$$

To this purpose I use `iminuit`[8] (Dembinski & et al. 2020) which is the `python` version of `Minuit2` C++

---

[8]`https://iminuit.readthedocs.io/en/stable/`
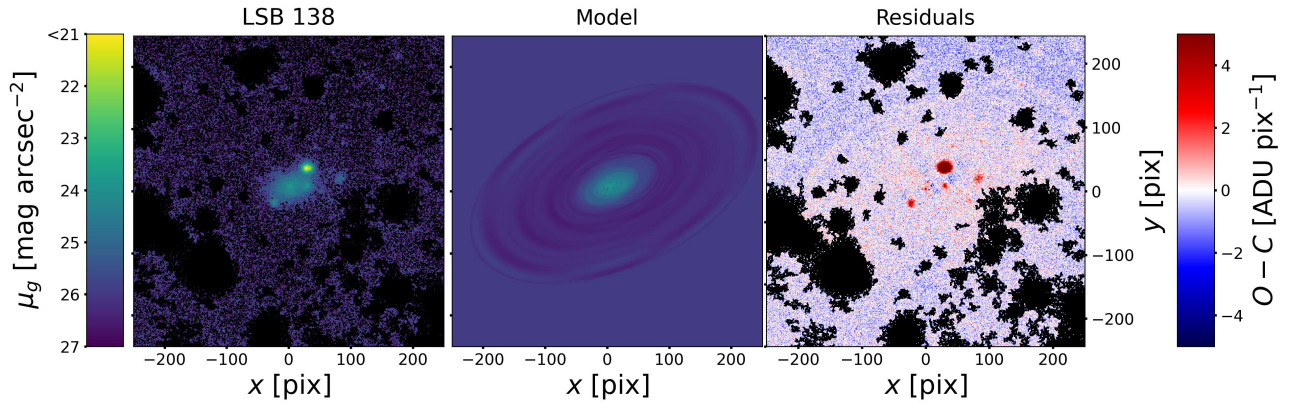
FIGURE 3.11: Example of isophote fit. From left to right: image, model, and residuals. Black pixels are those having either NaN or False values. In the left panel black pixels are also those having negative counts.
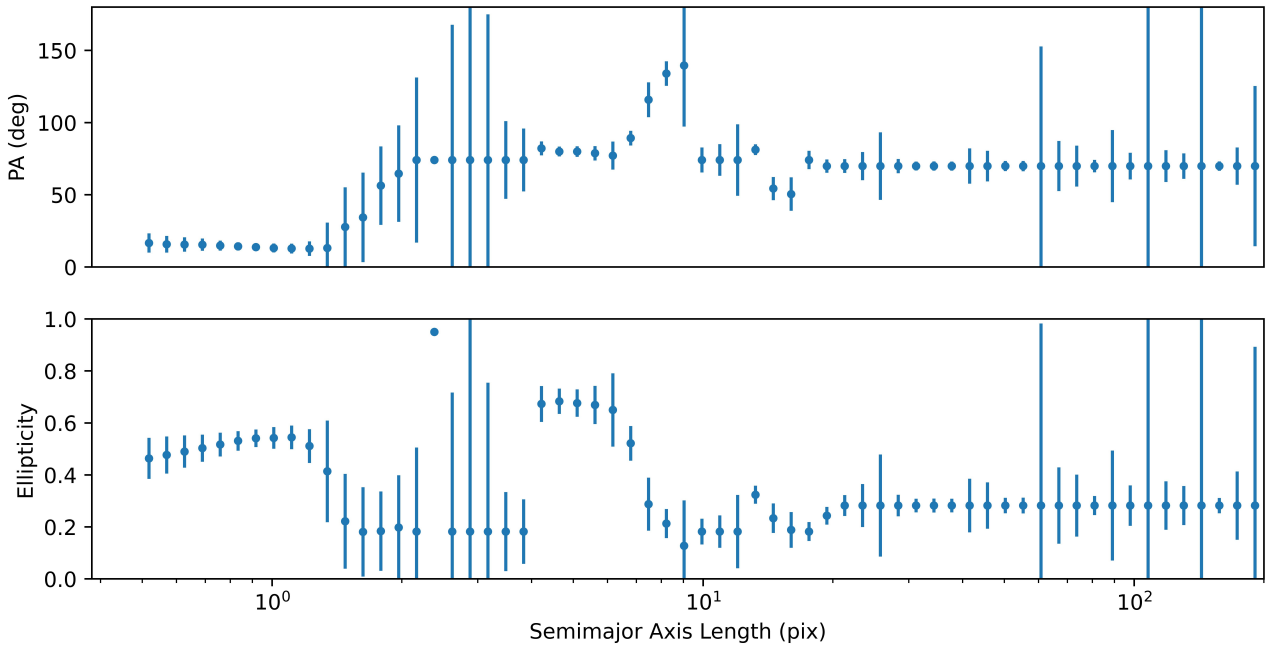
FIGURE 3.12: Position angle (top panel) and ellipticity (bottom panel) radial profiles of LSB100.

library maintained by CERN's ROOT team (James & Roos 1975), by applying a weighted least squares fit, where the weights are the inverse square of the errors. I show the fitting result in Fig. 3.13.

3.4   Growth curve

The growth curve is the radial profile of the total integrated luminosity. It is used to calculate the total magnitude of a source. In principle, a growth curve should appear with a steep rise and a plateau at large radii. I note that the accuracy of the total magnitude estimation is strictly related to the value of the background. In order to keep the total magnitude estimation stable against background inaccuracy I compute the total magnitude of each galaxy as the median value of the growth curve between r_{80} and $R_{\lim}$ paying the prize of a higher error. Indeed, the error is bigger with respect of using the corresponding value of the growth curve at $R_{\lim}$ because the growth curve is not constant in the range between r_{80} and $R_{\lim}$ and then the error on the median is biger than the error on the single value. Then, I convert the median into magnitudes and I propagate the error with `uncertainties`, a `Python` package for calculations with uncertainties[9].

---

[9]Eric O. LEBIGOT, http://pythonhosted.org/uncertainties/
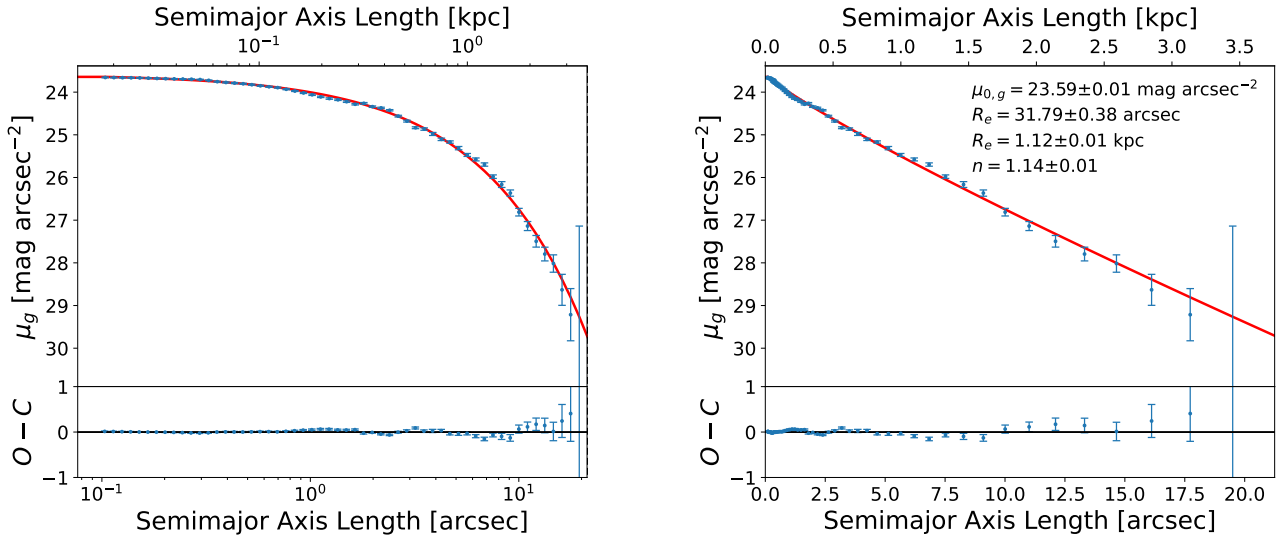
FIGURE 3.13: 1D-Sérsic fit of the surface-brightness radial profile. Both panels show the same fit (red line) to the same data (blue points) but with different radial scale.
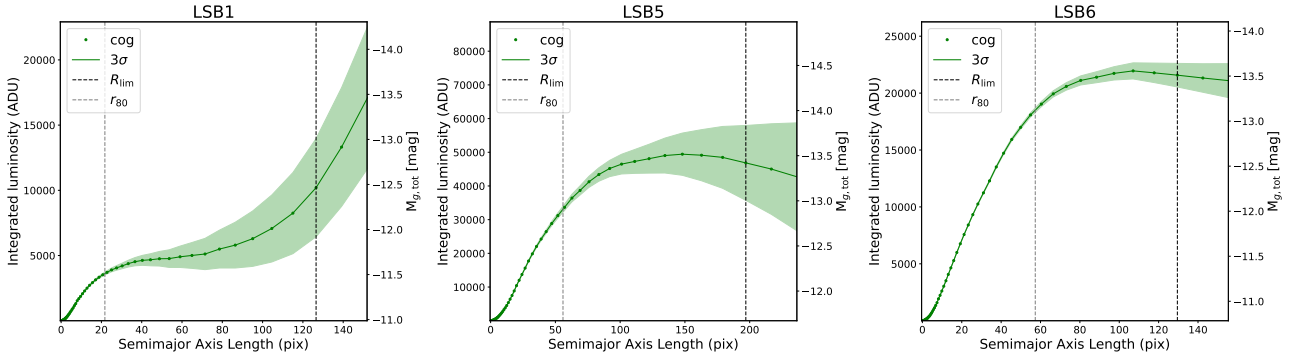
FIGURE 3.14: Growth curve for three LSB galaxies. The green shadowed area correspond to the 3σ error of the total integrated light. The dark and grey dashed lines are r_{80} and R_{lim}, respectively.

Growth curve issues   Growth curves in the LSB regime are very sensible to I_{sky} estimation and the growth curve analysis has still to be improved. The choice to use the median value of the curve of growth between r_{80} and R_{lim} as the estimate of the total magnitude comes from the following considerations:

- R_{lim} is computed as the first NaN of the isophote analysis, then it is not always related to the physical radius of the LSB galaxy.

- No matter which sky background I use, there are always galaxies with an inaccurate sky estimate that do not show a plateau in the growth curve.

In Fig. 3.14 I show an example of growth curve with a plateau (good case) and two examples of growth curve without a plateau (bad cases). In the bad cases often is involved a background which is not flat. The choice of using I_{sky} (Sec. 3.3.3) works only if the background fluctuation is homogeneous. The inaccurate sky background is then mainly due to the presence of global gradients in the background that needs to be subtracted before performing the isophotal analysis.

Chapter 4

Results

In this chapter I discuss the physical properties of the LSB galaxies that I found in the Centaurus cluster. I compare my new catalog of dwarf galaxies with another catalog available in the literature in Sec. 4.1. Then, I present the spatial distribution of the sample of LSB galaxies in Sec. 4.2 and their scaling relations in Secs. 4.3 and 4.4. I introduce the UDGs in Sec. 4.5 and discuss their abundance in Sec. 4.6. Finally, I discuss the trends of the properties of the LSB galaxies with cluster-centric distance in Sec. 4.7. I summarize the results in Sec. 4.8.

4.1 Catalog of LSB galaxies in the Centaurus cluster

The final catalog of LSB galaxies in the Centaurus cluster is made of 136 objects. The range of the total absolute magnitudes in g' band is $M_{g,\text{tot}} \in [-17.6, -14.5]$ mag. The errors on each parameter are described in the previous chapter. The error on the effective radius in kpc also includes the distance uncertainty. I show some examples of the LSB galaxies of my sample in Fig. 4.1. The main measured properties of the whole sample are reported in Tab. A.

I match my sample with Misgeld et al. (2009) catalog of early-type dwarf galaxies in the Centaurus cluster. I assume that two objects match if their projected distance is smaller than 5 arcsec.

Of the 136 galaxies, 6 LSB galaxies are also present in the Misgeld et al. (2009) catalog, so I report the discovery of 130, previously unknown LSB galaxies in the central region of the Centaurus cluster. The objects that match are: LSB43, LSB34, LSB52, LSB57, LSB93, and LSB119. The images of these galaxies, as well as the images of the whole sample of LSB galaxies are shown in the appendix (Fig. A.1).

4.2 Spatial distribution of the sample LSB galaxies

From the 2MASS catalog I retrieve a sample of bright galaxies ($-20.5 < M_B < -15$) in the central region of Centaurus cluster. The cluster membership is defined through the redshift. I compare the spatial distributions of LSB and bright galaxies in Fig. 4.2, where I also plot the location of the ETGs of Misgeld et al. (2009).

To better understand how the projected galaxy density changes going outward from the cluster center, I derive the fraction of the sample LSB galaxies enclosed in circular areas and I compare it with that of the 2MASS bright galaxies. I count the number of galaxies enclosed in circular areas centered in NGC 4696, I increase the radius with a step of 5.6 arcmin in radius (corresponding to 60 kpc at the distance of Centaurus cluster), and then divide that number by the total number of galaxies in the sample to have the cumulative fraction. I assume for all the cluster members the distance of the cluster (Fig. 4.2). I choose the bin step for being consistent with the work of La Marca et al. (2022b) on dwarf galaxies in Hydra I cluster (see Fig 9 of their paper). They find that the giant galaxies are more concentrated toward the center with respect to dwarf galaxies. On the contrary, I find that there is no substantial variation in the central concentration between the bright galaxies of 2MASS and my LSB galaxies. The catalog by Misgeld et al. (2009) is obtained with seven fields with a FoV of 7×7 arcmin^2 which are not symmetrically distributed. Hence, I do not compare the central concentration with it.
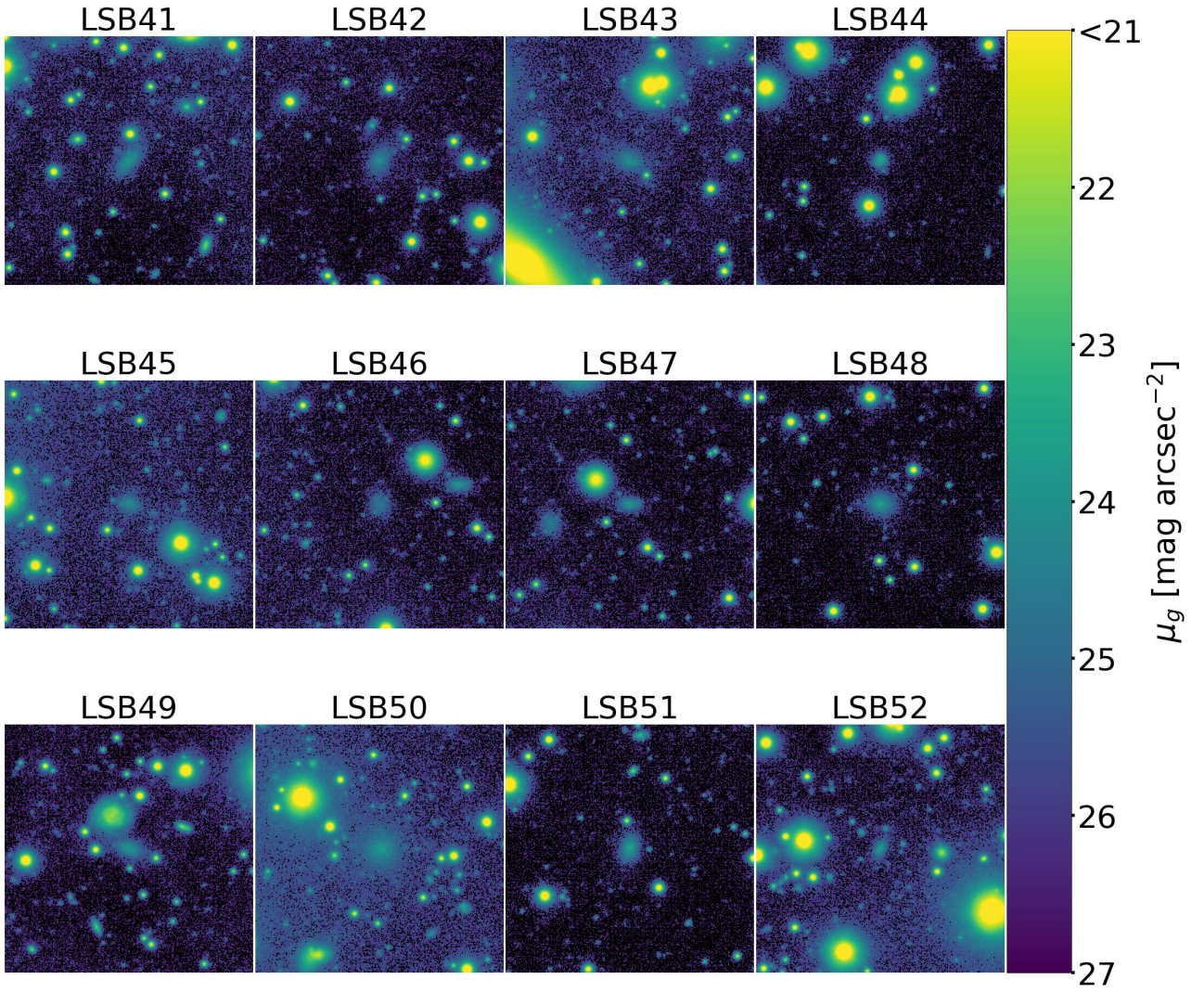
FIGURE 4.1: Examples of sample LSB galaxies. The FoV of each image is 1.7×1.7 arcmin^2 with north up and east left.

4.3 Color-magnitude relation of the sample LSB galaxies

In Fig. 4.3 I compare the color-magnitude relation (CMR) of my sample with that of Misgeld et al. (2009). I convert the g' and r' magnitudes using the transformations by Kostov & Bonev (2018) because Misgeld et al. (2009) computed the Johnson V and I magnitudes:

$$V = r' - 0.017 + 0.492(g' - r') \ ,$$
$$V - I = 0.27 + 1.26(g' - r') \ . \tag{4.1}$$

I compare the slope of the CMR obtained for my sample of LSB galaxies with that of Misgeld et al. (2009):

$$(g' - r')_0 = -0.06(\pm 0.02)M_{r,0} - (0.07 \pm 0.26) \qquad \text{this thesis}$$
$$(g' - r')_0 = -0.032(\pm 0.001)M_{r,0} + 0.047(\pm 0.02) \quad \text{Misgeld et al. (2009)} \tag{4.2}$$

I find that they are in agreement at 2σ confidence level. I note that my sample covers a shorter range of magnitudes with respect to that of Misgeld et al. (2009) (Fig. 4.3). Moreover, they searched for early-type dwarf galaxies, whereas I search for LSB galaxies in general.
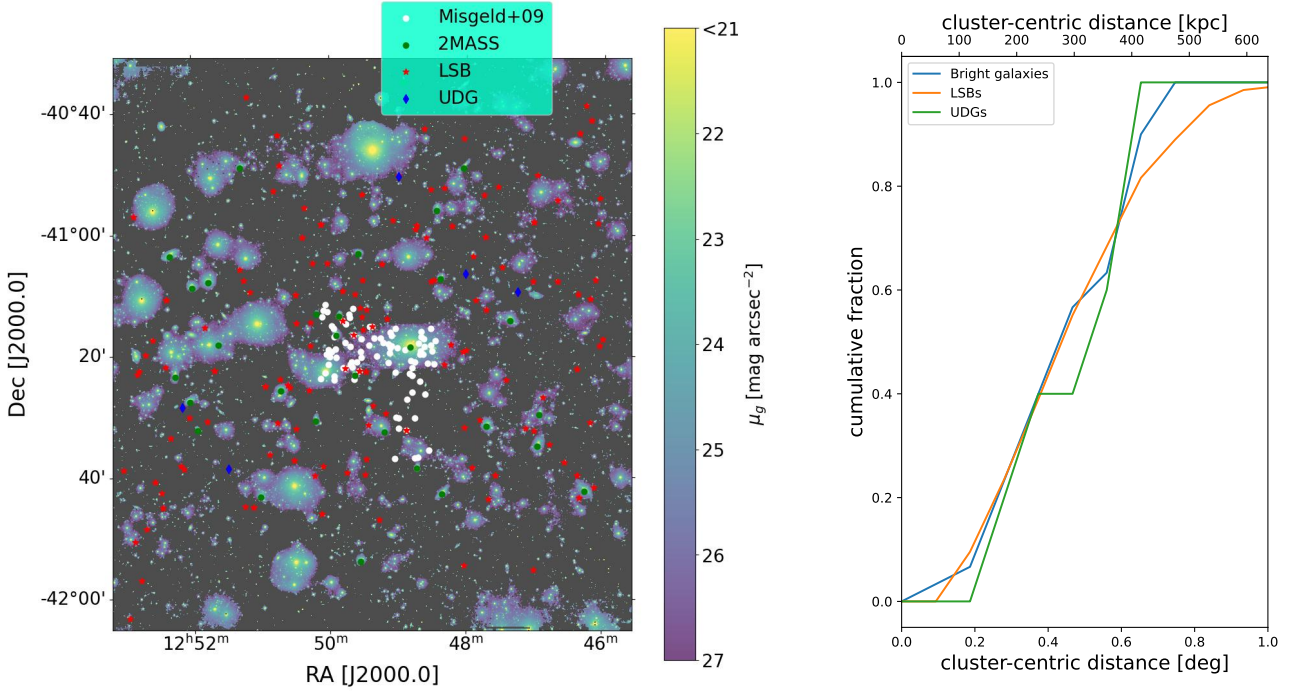
FIGURE 4.2: Spatial distribution of the sample UDGs and LSB galaxies. Left panel: g'-band VEGAS image of Centaurus cluster. The red stars are the 131 sample LSB galaxies, blue diamonds are the 5 sample UDGs, green dots are the bright galaxies from 2MASS catalogue and white circles are the ETGs from Misgeld et al. (2009). Right panel: Cumulative fraction of the galaxies with respect to the cluster-centric distance. The orange and green lines show the LSB galaxies and UDGs, respectively. The blue line marks the bright galaxies from 2MASS.

4.4 Correlations between properties and effective radius of the sample LSB galaxies

I search for correlations between the effective radius R_e of the sample of LSB galaxies and their total absolute magnitude in g'-band $M_{g,\text{tot}}$, Sérsic index n, color $(g' - r')_0$, central and effective surface brightness in g'-band $\mu_{g,0}$ and $\mu_{g,e}$, respectively (Fig. 4.4).

I perform a least-squares linear fit to my data:

$$
\begin{aligned}
(g' - r')_0 &= 0.02(\pm0.02)R_e + 0.69(\pm0.02) \\
n &= 0.36(\pm0.03)R_e + 0.55(\pm0.04) \\
M_{g,\text{tot}} &= -1.12(\pm0.11)R_e - 12.40(\pm0.13) \\
\mu_{g,0} &= -0.14(\pm0.10)R_e + 23.67(\pm0.12) \\
\mu_{g,e} &= -0.64(\pm0.09)R_e + 24.54(\pm0.10) \; .
\end{aligned}
\tag{4.3}
$$

I assume the error on the parameters to be the square root of the diagonal elements of the covariance matrix. I find that $\mu_{g,0}$ and $(g' - r')_0$ do not depend on R_e, whereas n, $\mu_{g,e}$, and $M_{g,\text{tot}}$ correlate with R_e.

The parameters in the Sérsic model R_e, n, and $\mu_{g,e}$ are not independent. Indeed, the value $1/n$ is a measure of the galaxy light concentration. Given a certain central surface brightness, larger objects are less concentrated so they have a larger Sérsic index. My selection criterion is based on the central surface brightness and this is the reason why larger LSB galaxies show larger n. In addition, given a fixed range of central surface brightness, the surface brightness at the effective radius is expected to be fainter increasing the effective radius (Kormendy 1977). A similar correlation is well known in literature (Ferrarese et al. 2020; La Marca et al. 2022b). The correlation with $M_{g,\text{tot}}$ is well known too (La Marca et al. 2022b). I considered such an obvious correlation with the other ones involving $(g' - r')_0$, n, $\mu_{g,0}$ and $\mu_{g,e}$ as a double check of my data.
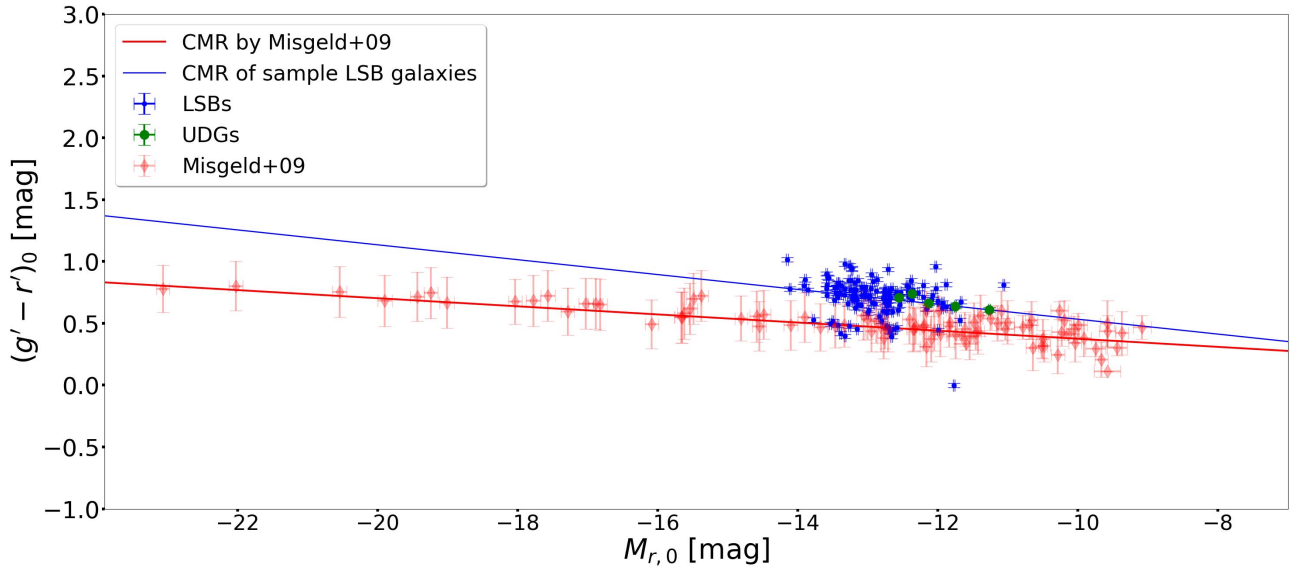
FIGURE 4.3: Color-magnitude diagram for the sample UDGs and LSB galaxies. The red line is the CMR by Misgeld et al. (2009) obtained from early-type dwarf galaxies (red diamonds). The blue stars and green circles are the sample LSB galaxies and UDGs, respectively. The blue line is the CMR obtained from my sample of LSB galaxies.

4.5   Detection of ultra diffuse galaxies

All LSB galaxies with $R_e \geq 1.5\,\text{kpc}$ and $\mu_{g,0} \geq 24$ mag arcsec^{-2} are defined UDGs. According to this definition I discover 5 UDGs in Centaurus cluster that I show in Fig. 4.5. I adopted the empirical definition from van Dokkum et al. (2015) to define the UDGs from my LSB sample (Fig. 4.6). I note that UDG1, UDG2, UDG4 and UDG5 have the same morphology of other UDG found in the literature (La Marca et al. 2022a), whereas the detection algorithm overestimates the effective radius of UDG3. This overestimation is due to the presence of an excessive number of spurious sources which are not removed by the sigma-clipping algorithm.

Based on the average colors, it seems that there are two populations of UDGs in clusters of galaxies: the red and quenched UDGs, which lie on the red sequence, and a blue population of UDGs, which are mostly in the field (e.g., Román & Trujillo 2017b). The UDGs shown in Fig. 4.3 follow the CMR of Misgeld et al. (2009), which is a red sequence of ETGs. Thus, the 5 newly discovered UDGs are red and quenched. I note that the UDGs are systematically redder than the CMR.

Lim et al. (2020) proposed to identify the UDGs in a different approach. Their idea is to define UDGs as outliers of the scaling relations. They do this with the Virgo galaxies of the NGVS. They studied the three scaling relations of $M_{g,\text{tot}}$ as function of $\mu_{g,e}$, medium surface brightness within the effective radius $\langle\mu\rangle_{g,e}$, and R_e. They best-fitted the three scaling relations with a fourth order polynomial taking into account for the completeness of their sample. Then they defined two classes of UDGs:

- Primary UDGs: outliers at 2.5σ confidence level of all three scaling relations.

- Secondary UDGs: outliers at 2.5σ confidence level of at least one of the three scaling relations.

Following their idea, I plot $M_{g,\text{tot}}$ as a function of $\mu_{g,e}$ and R_e in Fig. 4.7. The black lines are the scaling relations and their confidence regions $\pm2.5\sigma$ found by Lim et al. (2020). Not all the 5 newly discovered UDGs are outliers of these scaling relations. Two of them are secondary UDGs according to Lim et al. (2020). The 2.5σ outliers of the scaling relations are showed in Fig. 4.7. I note that LSB113 is probably an UDG too, but the algorithm underestimates its size because of the brighter overlapped spot which is included in the Boolean mask. I note that the structural parameters of some LSB galaxies change with different constraints in the 1D-Sérsic fit of Sec. 3.3.3. LSB90 and LSB113 are not UDGs according to the constraints I adopted, but I note that they were previously classified as UDGs with different constraints in fitting the 1D Sérsic model.

In addition, there are some other LSB galaxies that are morphologically similar to the UDGs of my sample.

- UDG1 and UDG2 are similar to LSB22, LSB23, and LSB76;
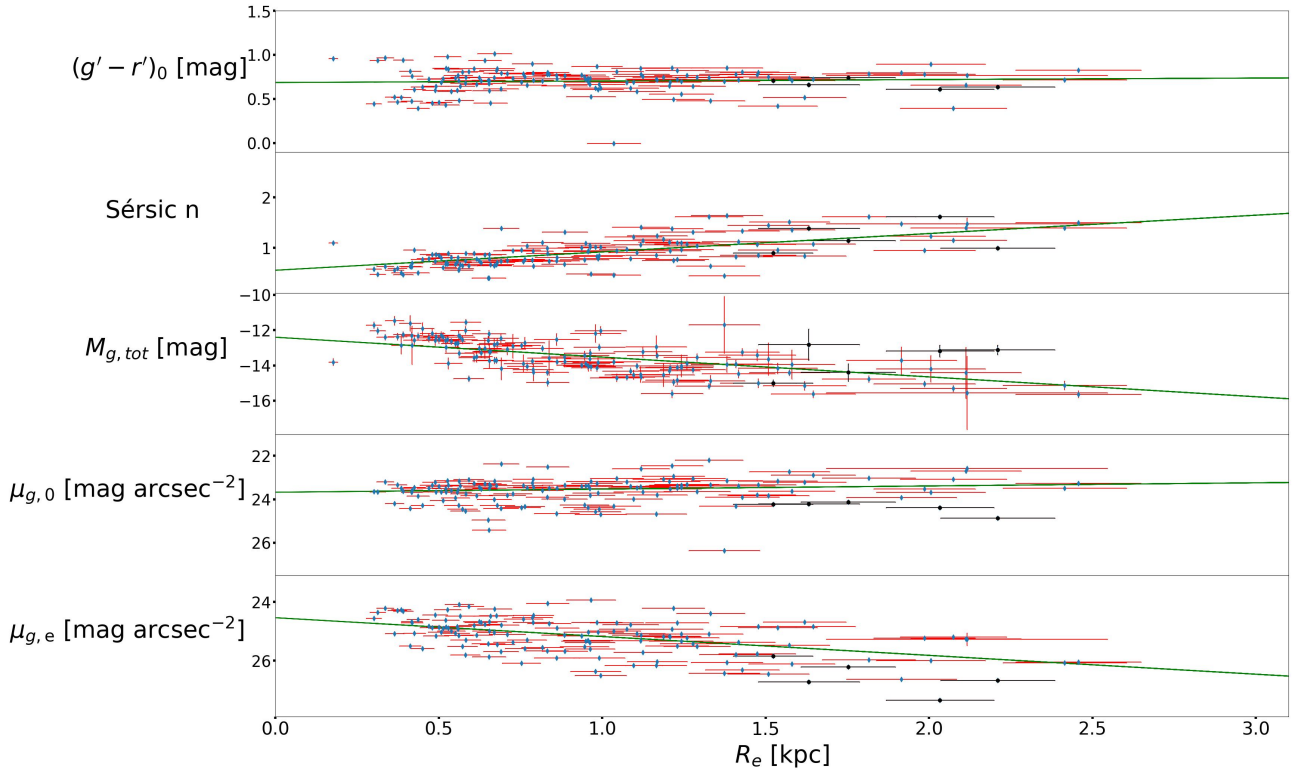
FIGURE 4.4: Scaling relations for the sample UDGs and LSB galaxies. From top to bottom: $(g' - r')_0$, n, $M_{g,tot}$, $\mu_{g,0}$, and $\mu_{0,e}$ as function of the effective radius R_e. Blue and black diamonds are the sample LSB galaxies and UDGs, respectively. The green lines are the linear fits to the data.
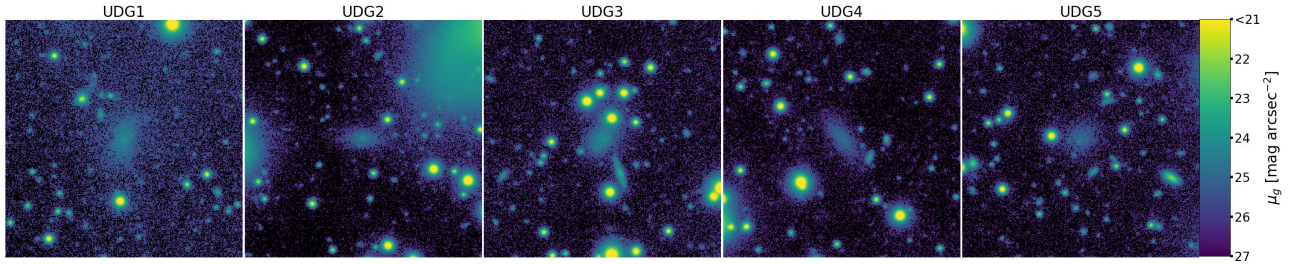
FIGURE 4.5: The sample UDGs. The FoV of each image is 1.7×1.7 arcmin^2 with north up and east left.

- UDG4 is similar to LSB23;

- UDG5 is similar to LSB13 and LSB96.

This evidence suggests that might exist LSB galaxies with a morphology similar to UDGs. The quantitative classification must be done by measuring the structural parameters. From visual inspection it is not possible to appreciate structures fainter than 27 mag arcsec^{-2}. It is possible to distinguish them only after averaging the surface brightness over the azimuthal angle and performing a 1D-Sérsic fit. Despite some LSB galaxies appear morphologically similar to UDGs and despite there is not an unambiguous definition for UDG, I name these targets as LSB galaxies, except for those which follow the van Dokkum et al. (2015) definition. In addition, the choice of how analysing the data changes the number of detected UDGs. For instance, Lim et al. (2020) applied a parametric fit of the 1D surface brightness profile using one- or two-component Sérsic models with the possible inclusion of a central point source for nucleated galaxies. In addition, before fitting they subtract the surface brightness of near by sources. Then they took the structural parameters from the brightest Sérsic model in the case of two-component targets. With this choice LSB123 and LSB113 (Fig. A.1), as well as LSB13, LSB50, LSB56, LSB76, LSB86, LSB101, LSB107, LSB109, LSB113, and LSB118 could be UDGs. In fact, they have $R_e > 1.5$ kpc but a too bright surface brightness because they are nucleated galaxies and so they have a cusp in the center which should be fitted with the model of a central point source. Similar UDGs are found in literature (e.g., La Marca et al. 2022a; see their UDG14 and UDG17).
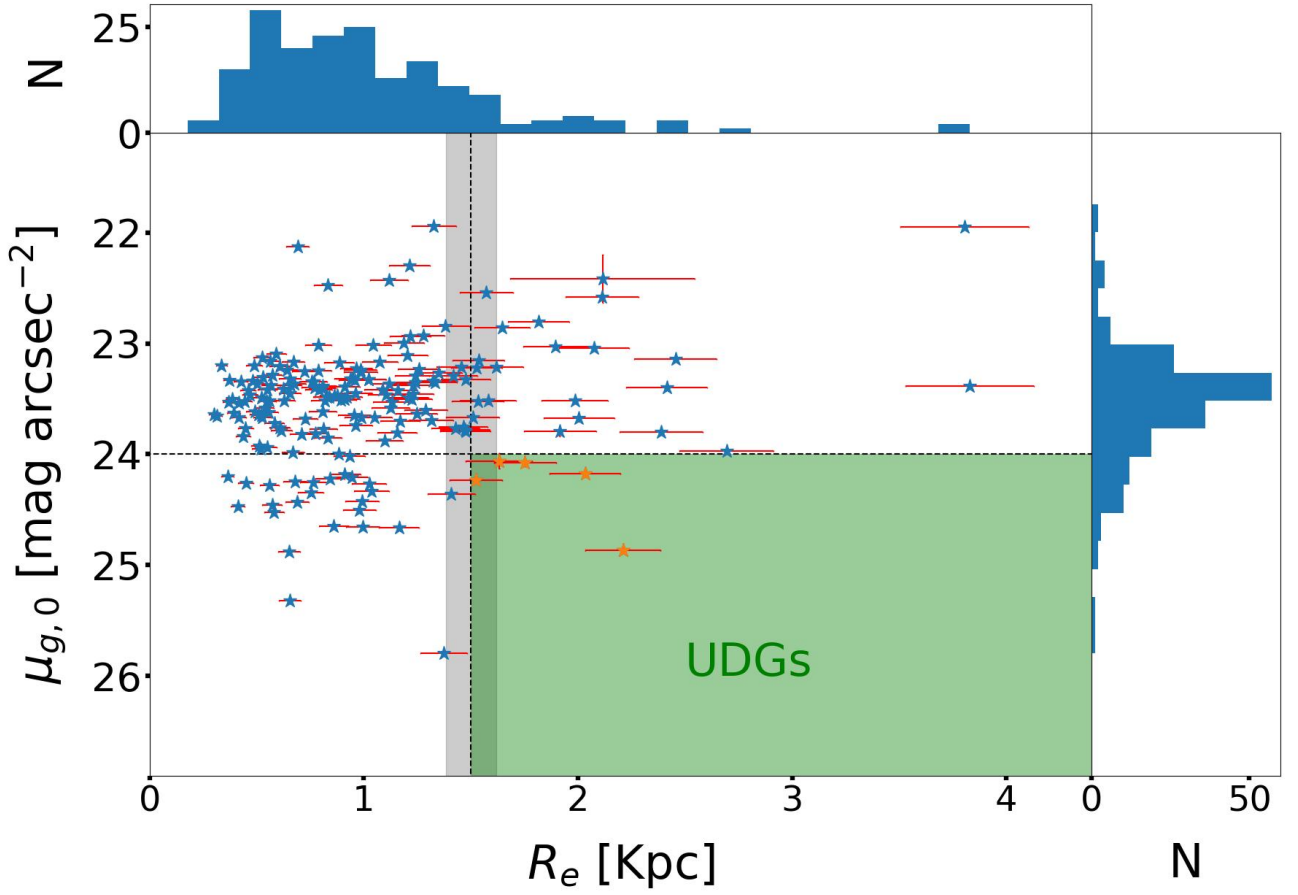
FIGURE 4.6: Central surface brightness and effective radius of the sample UDGs and LSB galaxies. Blue stars with red errorbars are my 131 LSB galaxies, while orange stars are the 5 UDGs. The green area delimited by the two black dashed lines is region at $R_e > 1.5$ kpc and $\mu_{g,0} > 24$ mag arcsec^{-2}. The grey shadowed area around the vertical dashed line is the 1σ error of the distance. The two histograms are the distribution of the two parameters in the plot, where N is the number of galaxies per bin. Each bin is 0.66 kpc wide.

Despite the whole discussion of which sample LSB galaxy could be or not a UDG, I decide to follow the van Dokkum et al. (2015) definition. I make this choice for being consistent in the comparison of the number of UDGs with the majority of the other works in literature.

4.6 Abundance of ultra-diffuse galaxies

I find $N_{VST} = 5$ previously unknown UDGs according to van Dokkum et al. (2015) definition.

In literature, there is an empirical relation called UDG-abundance-halo mass relation found by van der Burg et al. (2017) and Janssens et al. (2017). It is a power law between the total number of UDGs whithin the virial radius R_{vir} of a galaxy cluster and its total mass M_{200}. More massive clusters contain more UDGs. I scale N_{VST} up to $1R_{vir}$ in order to compare my result with this relation by assuming $h = 0.7$ and $R_{200} = R_{vir}$. For simplicity, I symmetrize the errors on the virial radius and masses: $R_{vir} = 0.935^{+0.020}_{-0.015} \, h^{-1}$ Mpc$= 0.655 \pm 0.014$ Mpc and $M_{200} = 1.89^{+0.12}_{-0.09} \times 10^{14} \, h^{-1} \, M_{\odot} = 1.32 \pm 0.08 \times 10^{14} \, M_{\odot}$. I assume the Einasto (1965) profile fitted by van der Burg et al. (2016) as radial number density distribution. The Einasto profile provides a better description of the UDG radial density distribution than the Navarro-Frenk-White profile (Navarro et al. 1997). The number density radial profile that I use is:

$$\rho(r) = \rho(R_{vir}) e^{-\frac{c}{a}\left[\left(\frac{r}{R_{vir}}\right)^a - 1\right]} \tag{4.4}$$

Where $c = 1.83$ and $a = 0.92$ are the parameters fitted by van der Burg et al. (2016). I have $N_{VST} = 5$ UDGs within a circular area of $R_{VST} = 0.76R_{vir}$ which is the maximum circular area enclosed in the VEGAS image of the Centaurus cluster (Fig. 2.4). I get the total number of UDGs N_{UDG} within R_{vir} as follows:
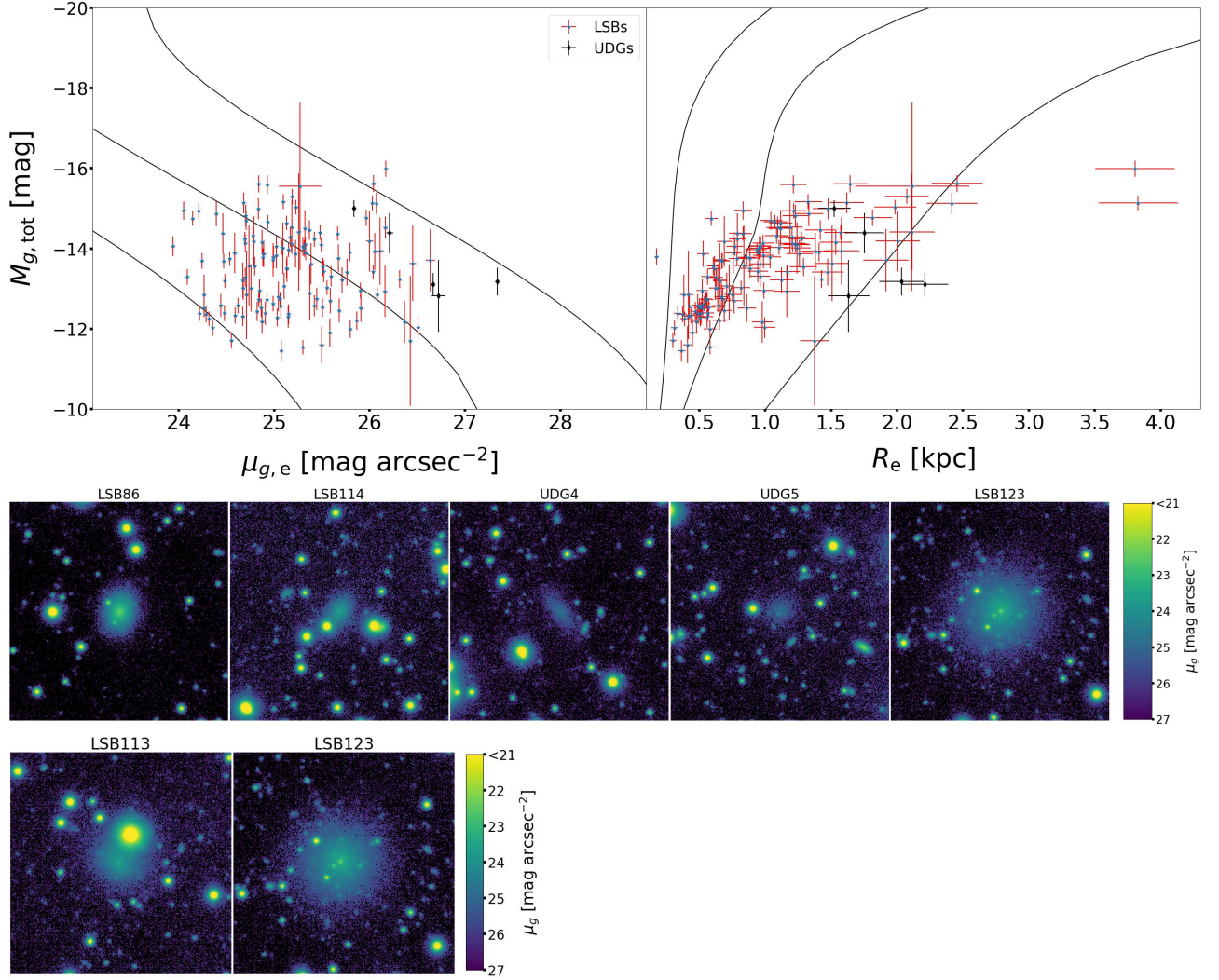
FIGURE 4.7: Scaling relations to select UDGs from Lim et al. (2020). Left panel: $M_{g,\text{tot}}$-$\mu_{g,\text{e}}$ relation. Right panel: $M_{g,\text{tot}}$-R_{e} relation. The solid black lines mark the relations and their $\pm 2.5\sigma$ confidence limits. The blue stars and black diamonds are the sample LSB galaxies and UDGs according to the selection criteria by van Dokkum et al. (2015). Bottom images: Selected UDGs according to the selection criteria by Lim et al. (2020). The FoV of each image is 1.7×1.7 arcmin^2 with north up and east left. LSB113 and LSB123 are selected from the $M_{g,\text{tot}}$-$\mu_{g,\text{e}}$ relation, whereas LSB86, LSB114, UDG4, UDG5, and LSB123 are selected from the $M_{g,\text{tot}}$-R_{e} relation.

$$\begin{cases} \frac{N_{\text{VST}}}{\frac{4}{3}\pi r_{\text{VST}}^3} = \rho(R_{\text{vir}}) \int_0^{R_{\text{VST}}} 2\pi r\rho(r)\mathrm{d}r \\ \frac{N_{\text{UDG}}}{\frac{4}{3}\pi R_{\text{vir}}^3} = \rho(R_{\text{vir}}) \int_0^{R_{\text{vir}}} 2\pi r\rho(r)\mathrm{d}r \end{cases} \tag{4.5}$$

and making the ratio of the two equations to simplify $\rho(R_{\text{vir}})$:

$$N_{\text{UDG}} = N_{\text{VST}} \frac{R_{\text{vir}}^3}{R_{\text{VST}}^3} \frac{\int_0^{R_{\text{vir}}} 2\pi r\rho(r)\mathrm{d}r}{\int_0^{R_{\text{VST}}} 2\pi r\rho(r)\mathrm{d}r} \quad . \tag{4.6}$$

Therefore, I obtain $N_{\text{UDG}} = 20 \pm 8$ UDGs for the Centaurus cluster, where the error is calculated by propagating the Poissonian error on the UDG counts $N_{\text{VST}} = 5 \pm 2$ and error on R_{vir}. In Fig. 4.8 I compare N_{UDG} with the literature concluding that I find a number of UDGs that is in agreement with similar works. I use the UDG abundance-halo mass relation:

$$N_{\text{UDG}} \propto M_{200}^{1.11 \pm 0.07} \tag{4.7}$$

to compute as a double check the expected number of UDGs within R_{VST}. The error is obtained propagating the errors on the exponent and the error on M_{200}. It is:

$$N_{\text{VST,expected}} = 8 \pm 1 \tag{4.8}$$
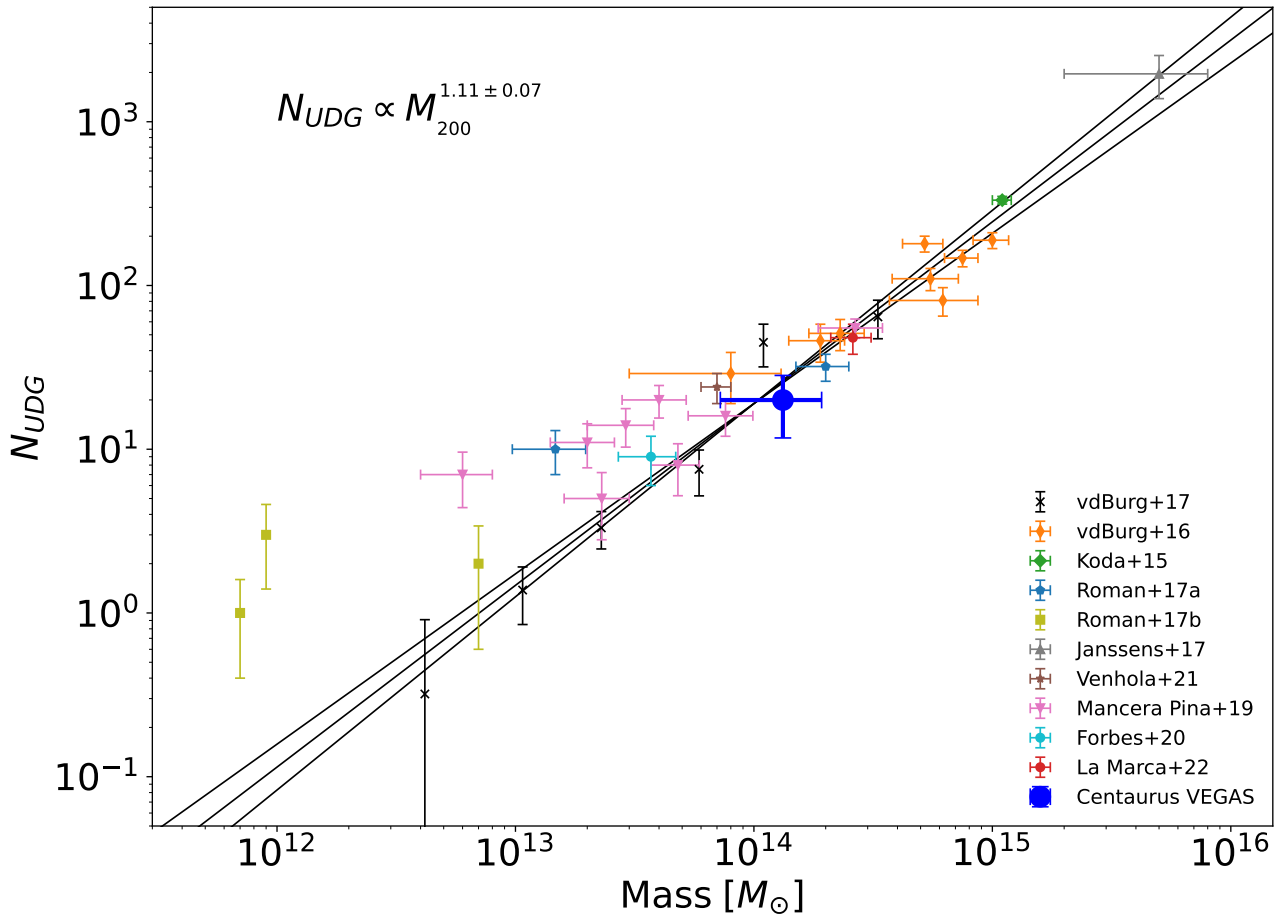
FIGURE 4.8: Abundance of UDGs as a function of the halo mass. The available data by Koda et al. (2015), van der Burg et al. (2016, 2017), Román & Trujillo (2017a,b), Janssens et al. (2017), Mancera Piña et al. (2019), Forbes et al. (2019, 2020), Venhola et al. (2022), and La Marca et al. (2022a) are shown. The black line represents the relation fitted by van der Burg et al. (2017). The blue dot is my result for the UDGs in the Centaurus cluster.

which is consistent with $N_{\rm VST} = 5 \pm 2$.

The UDG abundance-halo mass relation is one of the most important outcome of the last years in the study of UDGs. Because of the small number of UDGs, the scatter of the points of the plot increases with the decreasing of the halo mass at $M_{200} < 10^{14}$ $M_\odot$. Interestingly, the UDG abundance-halo mass relation holds for a wide range of masses covering massive and low-mass galaxy clusters, galaxy groups, and compact galaxy groups. This relation can give an insight on the formation scenarios of UDGs putting constraints in the cosmological-hydrodynamical simulations. Indeed, cosmological-hydrodynamical simulations have to be able to reproduce the UDG abundance-halo mass relation for being consistent with observations. In addition, this relation could be used as a new and completely independent method to estimate the virial mass of the cluster/group from the abundance of UDGs.

4.7   Cluster-centric properties of the sample LSB galaxies

In Fig. 4.9 I show the properties derived for the sample of LSB galaxies as function of their projected cluster-centric distance r_{BCG}, which I calculate as the distance on the image between the BCG coordinates and the center coordinates of each LSB galaxy. There is not a clear cluster-centric trend for the investigated parameters of LSB galaxies and UDGs.

I apply a least-squares linear fit to the LSB data for each parameter. As done in Sec. 4.4, the error on the fit
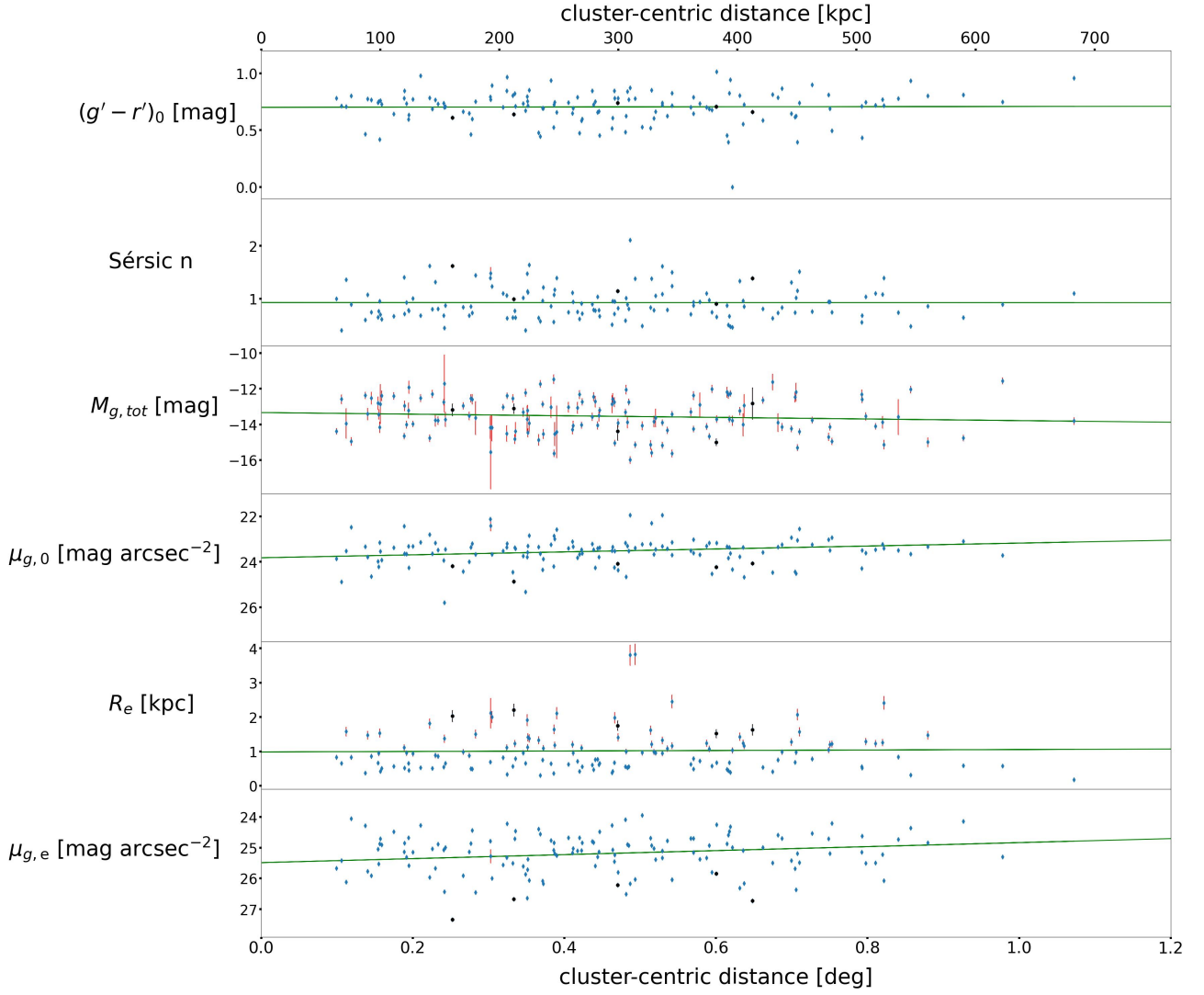
FIGURE 4.9: Galaxy parameters as a function of cluster-centric distance for the sample UDGs and LSB galaxies. From top to bottom: $(g'-r')_0$, n, $M_{g,\mathrm{tot}}$, $\mu_{g,0}$, R_e and $\mu_{g,\mathrm{e}}$ of the sample LSB galaxies (blue diamonds) and UDGs (black circles) as a function of their projected distance from the BCG located at RA $= 12^\mathrm{h}48^\mathrm{m}49.25^\mathrm{s}$, DEC $= -41°18'40.0''$ (J2000.0). Errorbars smaller than symbols are not plotted.

parameters is the square root of the diagonal elements of the covariance matrix. I find:

$$(g' - r')_0 = -0.01(\pm 0.06)r_\mathrm{BCG} + 0.70(\pm 0.03)$$
$$n = 0.00(\pm 0.13)r_\mathrm{BCG} + 0.93(\pm 0.06)$$
$$M_{g,\mathrm{tot}} = -0.45(\pm 0.41)r_\mathrm{BCG} - 13.34(\pm 0.21)$$
$$\mu_{g,0} = -0.64(\pm 0.28)r_\mathrm{BCG} + 23.82(\pm 0.14)$$
$$R_\mathrm{e} = 0.07(\pm 0.24)r_\mathrm{BCG} + 0.98(\pm 0.12)$$
$$\mu_{g,\mathrm{e}} = -0.65(\pm 0.29)r_\mathrm{BCG} + 25.49(\pm 0.15) \ .$$

(4.9)

There is only a weak correlation with $\mu_{g,0}$ and $\mu_{g,\mathrm{e}}$. The central surface brightness of the sample tends to increase toward the center, which is in contrast with La Marca et al. (2022b). The background of regions at larger r_BCG have on average fainter surface brightness because there are less bright galaxies. The detection efficiency is larger in regions where the background is fainter. Thus, I expected that increasing r_BCG the detection algorithm for LSB galaxies is able to find fainter objects, but this is not the case. So I conclude that it is likely that such a correlation is a physical effect.

4.8   Summary of the results

I analysed the g' band VEGAS image of the Centaurus cluster. I identified 136 LSB galaxies in the inner 1.4×1.6 deg^2 (1 Mpc^2) region centered on NGC4696. I measured the structural parameters of all the sample galaxies and I derived:

- the colour-magnitude relation (Eq. 4.2);

- the number of UDGs (Sec. 4.6);

- the relations between the structural parameters and effective radius (Eq. 4.3);

- the correlation between cluster-centric distance and surface brigtness (Eq. 4.9).

Chapter 5

Discussion and conclusions

I this chapter I discuss my results and present my conclusions. I compare the properties of the LSB galaxies in the Centaurus with the LSB populations of other clusters in Secs. 5.2 and 5.3. Then, I discuss the implication of the number of detected UDGs and I compare two different definitions of UDGs in Sec. 5.4. Finally, I give my conclusions and future perspectives in Secs. 5.5 and 5.6, respectively.

5.1 LSB galaxies in the Centaurus cluster

I presented a new catalog of 136 LSB galaxies in the Centaurus cluster based on VEGAS deep g'-band imaging that covers the cluster out to $0.76R_{\rm vir}$. The sample LSB galaxies have a central surface brightness $21.8 < \mu_{g,0} < 26$ mag arcsec^{-2} , effective radius $0.15 < R_{\rm e} < 4$ kpc, effective surface brightness $23.8 < \mu_{g,e} < 27.5$ mag arcsec^{-2}, total absolute magnitude $-16.5 < M_{g,\rm tot} < -11.5$ mag, and color index $-0.5 < (g' - r')_0 < 1.05$ mag.

I compare the sample LSB galaxies with the sample collected by Misgeld et al. (2009). They studied seven fields of Centaurus cluster of 7×7 arcmin^2 each with FORS1 at VLT. All these fields are covered by the VEGAS image (Fig. 2.4). Their aim was to study the CMR for early-type dwarf galaxies and they analysed ETGs in a wide range of luminosities in the Johnson V and I filters. Their detection strategy was a combination of visual inspection and SExtractor detection. They studied a sample of 132 galaxies with total magnitudes in the range $10 < M_V < 24$ mag.

I have only 10 objects in common with Misgeld et al. (2009). The main reason for such a weak match between the two catalogs is the different classes of objects which were considered: I search for LSB galaxies with a particular interest for large and diffuse galaxies, whereas Misgeld et al. (2009) searched for ETGs with a particular interest for dwarf elliptical (dE) galaxies which are brighter and more compact. Indeed, only 17 objects from Misgeld et al. (2009) match the magnitude range of my sample LSB galaxies (Fig. 4.3), of which 10 objects are present in both catalogs. I check the VEGAS image to investigate the origin of the mismatch of the other 7 early-type dwarf galaxies.

Misgeld et al. (2009) modelled and subtracted the surface brightness distribution of the BCG and other bright galaxies before searching for the dwarf galaxies. Because of the surface brightness selection, the galaxies marked by white points in Fig. 4.2 that fall inside the halo of the bright galaxies are excluded from my sample. The other galaxies of the sample are all visible, but most of them are faint enough to appear smaller than $A = 400$ pix in the image. They are excluded by the selection criterion that I applied to obtain the sample LSB galaxies.

5.2 Spatial distribution of the sample LSB galaxies and UDGs

In Fig. 4.2 I show that the spatial distribution of sample LSB galaxies does not differ from that of the bright galaxies of 2MASS. This is in disagreement with previous results (e.g., Lee et al. 2020; La Marca et al. 2022b), which generally accepted the scenario in which the LSB and dwarf galaxies, are shaped by tidal interactions and/or RPS (e.g., Popesso et al. 2006, and references therein). Hence, the sample LSB galaxies were expected
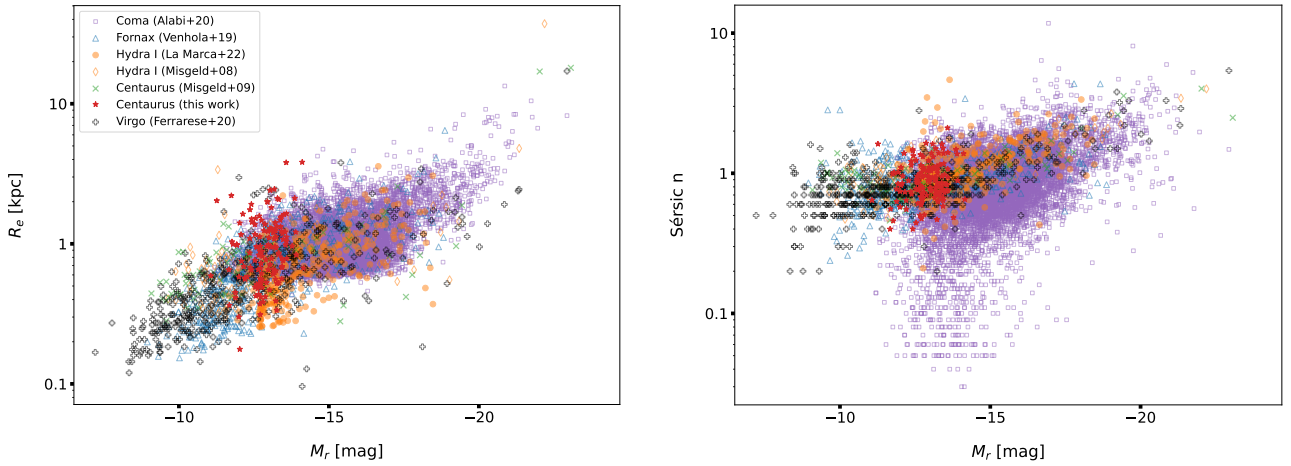
FIGURE 5.1: Scaling relations for different clusters in r'-band. Left panel: R_e-M_r relation. Right panel: n-M_r relation. The LSB galaxies are marked by red stars.

to be less concentrated near the center of Centaurus cluster with respect to giant galaxies because RPS and tidal forces are stronger.

On the other hand, to what was thought based on previous studies (e.g., Mancera Piña et al. 2018), Lim et al. (2020) found that the UDGs are more clustered near the cluster center than other dwarf galaxies, in agreement with simulation predictions. In fact, recent IllustrisTNG cosmological hydrodynamical simulations suggested that two classes of UDGs might exist (e.g., Sales et al. 2020): one located in the field and the other one dominating near the cluster center. The former class is defined by "genuine" UDGs, whereas the large size and LSB of the latter ones, named as "tidal" UDGs, have been shaped by the cluster tides. These tidal UDGs are characterised by lower velocity dispersion, higher metallicity, and lower DM content than the genuine UDGs, and they have an enhanced concentration at the cluster center. I found 5 ± 2 UDGs within $0.76 R_{\mathrm{vir}}$. This number is too small to evaluate their spatial distribution. In addition, I ruled out the possibility to find more tidal UDGs without subtracting the surface brightness of the BGC NGC 4696.

5.3 Scaling relations of the sample LSB galaxies

Correlations among global parameters of galaxies provide insight into the physical processes that impact the formation and evolution mechanisms of these galaxies. In bright ETGs and in spheroids of LTGs, luminosity, color, size, surface brightness, light concentration, and central velocity dispersion are related to each other (e.g., D'Onofrio et al. 2021, and references therein).

The fundamental plane, CMR, and luminosity-surface brightness relation link the physical properties of the galactic stellar population and global structural properties with the galaxy mass. Investigating these scaling relations in multiple environments sets constraints for galaxy evolutionary models. Interestingly, since the observed properties of galaxies reflect their evolution, it is possible to infer how they reached the actual configuration, and what were the main processes responsible for their evolution.

In Fig. 5.1 I compare the scaling relations of the LSB galaxies in the Centaurus cluster with the analogous relations from other clusters in the Local Universe. They are the Virgo (Ferrarese et al. 2020), Fornax (Venhola et al. 2019), Hydra I (Misgeld et al. 2008; La Marca et al. 2022b), Centaurus (Misgeld et al. 2009), and Coma (Alabi et al. 2020) clusters.

In Sec. 4.4 I studied the correlations between galaxy parameters of the sample LSB galaxies. I conclude that the scaling relations investigated for LSB galaxies are comparable with those of LSB and dwarf galaxies of other clusters.

In dense environments, such as galaxy clusters, the dwarf galaxies can experience various environmental processes. RPS is a process affecting the interstellar matter in galaxies: when a galaxy falls into a cluster, its cold gas component interacts with the hot gas of the cluster and the pressure between the two gas components

removes the cold gas from the galaxy potential well (Gunn & Gott 1972). If not all the gas of the galaxy is removed at once, it is likely that a small gas fraction is retained in the center of the potential well, where it may have become over-pressurized leading to star formation. Indeed, there are dwarf galaxies in clusters (such as LSB168 in Fig. 4.7) with blue centers, which are indicative of a recent star formation episode (e.g., Lisker et al. 2006; Hamraz et al. 2019). These cases are often referred to as partial ram-pressure stripping. The ram-pressure stripping depends on the temperature of the hot intracluster medium (HIM) which is visible in the X-rays. The gas of a galaxy experiencing RPS is removed and the star formation drops. Then the evolution of the galaxy follows the evolution of the pre-existing stellar population becoming redder with time. The RPS is a formation channel for red dwarf galaxies.

If LSB galaxies are formed after RPS, I expect a spatial correlation between over-densities of LSB galaxies and over-density of HIM which emits in the X-rays through thermal-bremsstrahlung. Unfortunately, the Xray emission of the BCG of the Centaurus cluster is such intense that this effect is not visible.

LSB galaxies formed after RPS have an old and metal-poor stellar population and therefore they appear in the red sequence in the color-magnitude diagram. The sample LSB galaxies studied share a similar CMR to the Misgeld et al. (2009) red sequence, thus I conclude that RPS is a possible formation scenario.

In Sec. 4.7 I studied the correlations between the parameters of the sample LSB galaxies and their cluster-centric distance. I find a weak correlation with the surface brightness. This evidence is in agreement with the ex-situ formation scenario of LSB galaxies. Dwarf LSB galaxies could form from dwarf galaxies with higher surface brightness affected by RPS and harassment during their infall into the cluster (Tremmel et al. 2020). If so, the observed correlation is a consequence of the brightness-age relation predicted by simulations (Tremmel et al. 2020) and well known age-cluster-centric distance relation, which is caused by dynamical friction experienced by galaxies infalling into the cluster.

The brightness-age relation is the consequence of the fading of the stellar population after the star formation quenching caused by external processes. Another consequence of star formation quenching is the reddening of the stellar population.

Alabi et al. (2020) show that Coma LSB galaxies and UDGs appear bluer increasing the distance from the center of the cluster. A similar colour-r_{BCG} trend is also observed by Kadowaki et al. (2021). However, my analysis extends up to $0.76R_{\mathrm{vir}}$, whereas they reached the virial radius. Then it is possible that such a trend exists and a sample of LSB galaxies that covers a wider FoV is needed to investigate in further detail the colour-r_{BCG} relation. I note that it is likely that multiple formation scenarios for LSB galaxies are in act. In addition, some sample LSB galaxies are probably dEs as they are in the dE CMR by Misgeld et al. (2009) (Fig. 4.3).

5.4 Morphology of UDGs in the Centaurus cluster

In Sec. 4.5 I present 5 newly discovered UDGs with $R_{\mathrm{e}} \geq 1.5\,\mathrm{kpc}$ and $\mu_{g,0} \geq 24\,\mathrm{mag\,arcsec}^{-2}$ according to van Dokkum et al. (2015) definition. I compare their morphology with other LSB galaxies that are considered UDGs according to the different definition by Lim et al. (2020). In the left panel of Fig. 4.7 the 2.5σ confidence-level outliers do not include any of the 5 UDGs. This is in contrast with Lim et al. (2020) who aim at extending the UDG definition to more objects without excluding any UDG based on the van Dokkum et al. (2015) definition.

The method to compute the surface brightness radial profiles by Lim et al. (2020) differs from the one I adopt. Then, there is a systematic error in the comparison between the effective surface brightness and total magnitude of galaxies of two samples. I conclude that this systematic error is the reason why none of the 5 UDGs are 2.5σ confidence-level outliers in the scaling relations by Lim et al. (2020). I choose a smaller threshold than the 2.5σ confidence-level to define the outliers of the distribution. In particular, I choose a cut that includes 3 UDGs (orange line in Fig. 5.2). I show the thumbnails corresponding to the galaxies with a total magnitude smaller than the cut in Fig. 5.2.

The typical UDG morphology in literature (e.g., van Dokkum et al. 2015; La Marca et al. 2022a) consists of a diffuse object with irregular shape. Some of them also show a central concentration. I note that there is a large variety of LSB galaxies with similar UDG morphology. It is clear that the morphology of the UDG does not change using the scaling relations instead of the van Dokkum et al. (2015) definition to find UDGs. They
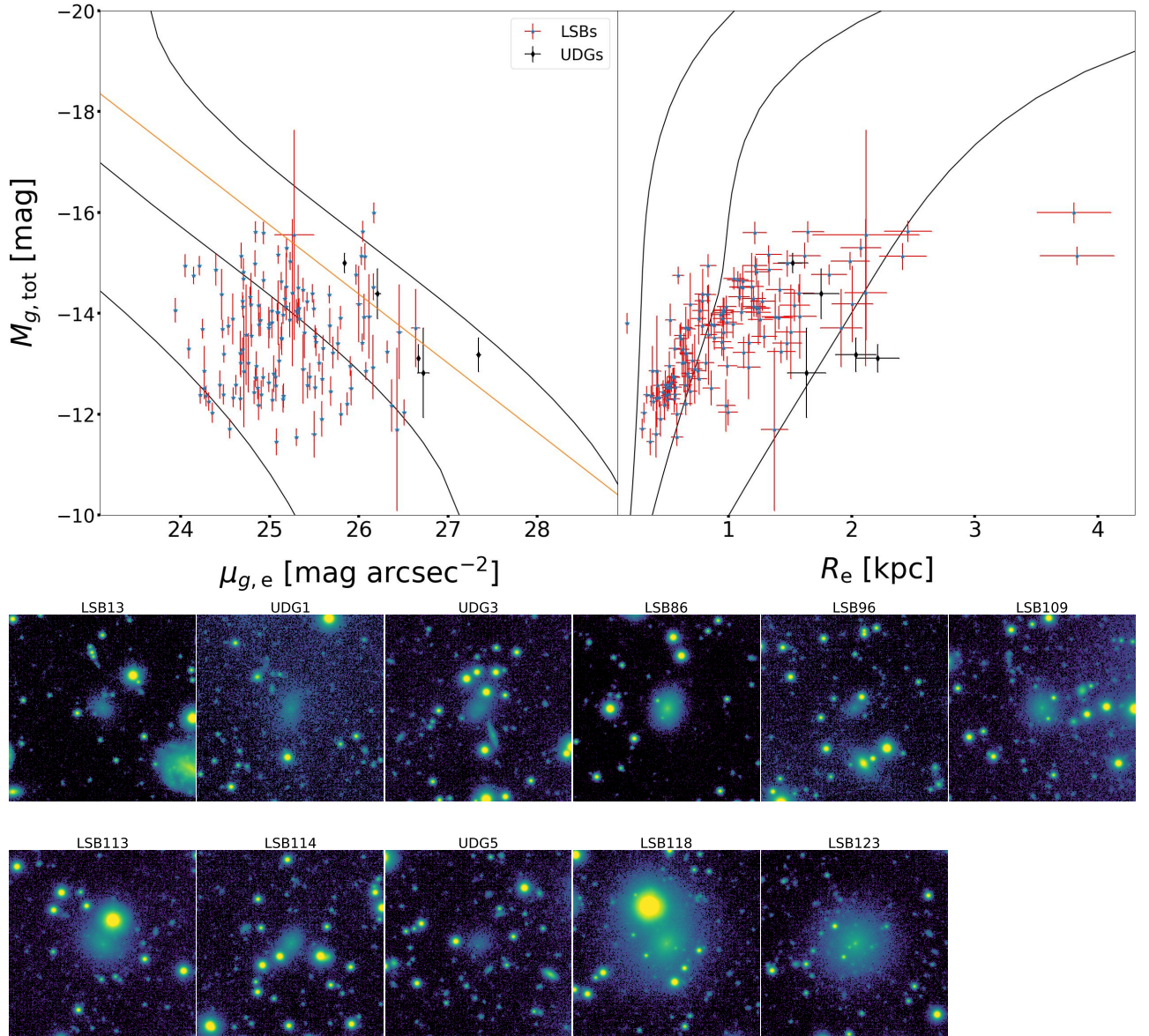
FIGURE 5.2: Definition of UDGs. Top panels: same as Fig. 4.7 but with my proposal for identifying UDGs in the M_g, tot-$\mu_{g,e}$ relation. Bottom panels: images of the UDGs identified following the above definition. The FoV of each image is 1.7×1.7 arcmin^2 with north up and east left.

are still faint and diffuse objects without a well-defined structure. The Lim et al. (2020) definition is more inclusive than the van Dokkum et al. (2015) one, so I conclude that a UDG classification based on the physical parameters of galaxies based on the scaling relations is physically more significant than a classification based on an empirical cut in size and surface brightness, which does not take into account for the physical properties of the whole sample LSB galaxies.

Comparing the morphologies of the sample UDGs and LSB galaxies I conclude that exist objects of the two samples with similar morphologies in agreement with other studies (e.g., Mancera Piña et al. 2019).

In the search for LSB galaxies, the detection algorithm does not distinguish LSB galaxies from large background galaxies. To this aim I apply a color selection to remove background galaxies at higher redshift. Large background galaxies can have structures, such as spiral arms or bars, while their angular size is comparable to the size of the sample LSB galaxies. These features are unlikely to be shown by small dwarf galaxies (Janz et al. 2014), although they can be present in the brightest dwarf galaxies which is not the case of UDGs. None of the sample UDGs show evidence of structures. There is evidence of spiral structure in LSB147 and of bar in LSB62. There are other doubtful cases, such as LSB2, LSB4, and LSB5.

In Sec. 4.6 I compute the expected number of UDGs enclosed in the virial radius of the Centaurus cluster by

assuming an Einasto number density profile. The result is compatible with the expected number of UDGs from the UDG abundance-halo mass relation. The slope value of the UDG abundance-halo mass relation is still discussed due to the large scatter of points in the low-mass regime.

Measuring the so-called mass-richness relation was the subject of several studies (e.g., Andreon & Hurn 2010, and references therein). They consistently measured a relation $N \propto M_{200}^{\alpha}$, where $\alpha < 1.0$ and N is the total number of galaxies. The value of the slope tells that the stellar mass fraction increases from clusters to group-mass halos (van der Burg 2014). Consequently, observations showing that the UDG abundance-halo mass relation has a slope larger than 1 would be a strong argument favouring the preferential (in-situ) formation of UDGs in clusters of galaxies. This is in agreement with recent cosmological hydrodynamical simulation which predict the existence of the tidal UDGs (Sales et al. 2020).

5.5 Conclusions

In the era of deep and wide observational surveys, the LSB universe represents an important frontier in the study of galaxy evolution. I identify a sample of 136 LSB galaxies in the Centaurus cluster. After the comparison with the literature, I conclude that:

- the sample LSB galaxies are on average redder than dEs galaxies and have a comparable slope of the CMR;

- the Kormedy relation is valid in the LSB regime too;

- the correlations between cluster-centric distance and surface brightnesses are in favour of an ex-situ formation of LSB galaxies;

- the number of UDGs, which is in agreement with the UDG abundance-halo mass relation, is in favour of the in-situ formation scenario.

5.6 Future perspectives

I will use the expertise gained in this thesis to improve the detection tool that I adopted. The improvements I will make to the program are the following:

- implement the local sky subtraction in each thumbnail using a second order polynomial;

- implement the subtraction of the surface brightness distribution of the BCG to increase the detection efficiency near the cluster center;

- test new detection algorithms such as `MTO`;

- use `DeepScan` to detect GCs;

- improve the isophotal analysis algorithm reducing the number of LSB galaxies for which the algorithm gives NaN as output;

- improve the analysis of the sample LSB galaxies by identifying different morphological classes (dE, dSph, UDG) to be studied separately;

- adopt convolution using different kernel equations to maximize the detection of a specific kind of object;

- improve the masking algorithm by adding the possibility to subtract the surface brightness distribution of near-by sources;

- Use already existing simulations of LSB galaxies to retrieve the detection efficiency and more reliable measurements of the errors. The use of mock galaxies instead of real data also allow to know in which cases the galaxy is not detected and this can be also exploited to improve the detection efficiency.

I am going to be a PhD student at the University of Padova starting from October 2022. The PhD project aims at identifying and studying UDGs in the 55 groups and clusters mapped by VEGAS. I plan to:

- Build a detection tool to find and analyse LSB galaxies in order to have a statistically significant sample of newly discovered UDGs.

- Study the structure of UDGs (e.g., size, luminosity, color) as function of environment to provide stringent constraints on the formation scenarios and their role in the mass assembly process.

- Interpret the results of the photometric analysis in the general context of galaxy formation and evolution by performing a comparison with the predictions of cosmological simulations (e.g., EAGLE, Illustris).

- Select a subsample of UDGs suitable for spectroscopic follow-ups to constrain the DM content and stellar populations.

The PhD project will be developed within the VEGAS collaboration and will allow to transfer to Padova specific technical expertise for the analysis of very faint galaxy structures in large-field images. They will be useful to tackle several open questions about the formation and evolution of nearby galaxies in general.

Bibliography

Abell, G. O., Corwin, Harold G., J., & Olowin, R. P. 1989, ApJS, 70, 1

Akhlaghi, M. & Ichikawa, T. 2015, ApJS, 220, 1

Alabi, A. B., Romanowsky, A. J., Forbes, D. A., Brodie, J. P., & Okabe, N. 2020, MNRAS, 496, 3182

Alam, S., Albareti, F. D., Allende Prieto, C., et al. 2015, ApJS, 219, 12

Amorisco, N. C. 2018, MNRAS, 475, L116

Amorisco, N. C. & Loeb, A. 2016, MNRAS, 459, L51

Anderson, J. 2020, Supplemental Dither Patterns for WFC3/UVIS, Instrument Science Report WFC3 2020-7 (STScI Baltimore, MD)

Andreon, S. & Hurn, M. A. 2010, MNRAS, 404, 1922

Arnaboldi, M., Capaccioli, M., Mancini, D., et al. 1998, The Messenger, 93, 30

Bautz, L. P. & Morgan, W. W. 1970, ApJ, 162, L149

Begeman, K., Belikov, A. N., Dijkstra, F., et al. 2013, Exp. Ast., 35, 355

Bertin, E. 2006, in V2.0.4, Astronomical Society of the Pacific Conf. Ser., Vol. 351, Astronomical Data Analysis Software and Systems XV, ed. C. Gabriel, C. Arviset, D. Ponz, & S. Enrique (Astronomical Society of the Pacific, San Francisco), 112

Bertin, E. 2010, SWarp: Resampling and Co-adding FITS Images Together, v2.17.6, ascl:10068B

Bertin, E. & Arnouts, S. 1996, A&AS, 117, 393

Binggeli, B., Sandage, A., & Tammann, G. A. 1985, AJ, 90, 1681

Bortoletto, F., Bonoli, C., Fantinel, D., Gardiol, D., & Pernechele, C. 1999, Rev. Sc. Ins., 70, 2856

Bradley, L., Sipőcz, B., Robitaille, T., et al. 2020, astropy/photutils: v1.0.0, doi: `10.5281/zenodo.4044744`

Busko, I. C. 1996, in Astronomical Society of the Pacific Conf. Ser., Vol. 101, Astronomical Data Analysis Software and Systems V, ed. G. H. Jacoby & J. Barnes (Astronomical Society of the Pacific, San Francisco), 139

Calamai, P. H. & Moré, J. J. 1987, SIAM Journal on Numerical Analysis, 24, 1434

Cantiello, M., Venhola, A., Grado, A., et al. 2020, A&A, 639, A136

Capaccioli, M., Spavone, M., Grado, A., et al. 2015, A&A, 581, A10

Chilingarian, I. V., Afanasiev, A. V., Grishin, K. A., Fabricant, D., & Moran, S. 2019, ApJ, 884, 79

Churazov, E., Gilfanov, M., Forman, W., & Jones, C. 1999, ApJ, 520, 105

Ciotti, L. 1991, A&A, 249, 99

Clauwens, B., Schaye, J., Franx, M., & Bower, R. G. 2018, MNRAS, 478, 3994

Contini, E., De Lucia, G., Villalobos, Á., & Borgani, S. 2014, MNRAS, 437, 3787

Cui, W., Murante, G., Monaco, P., et al. 2014, MNRAS, 437, 816

Dali Ali, W., Ziad, A., Berdja, A., et al. 2010, A&A, 524, A73

de Jong, J. T. A., Kuijken, K., Applegate, D., et al. 2013, The Messenger, 154, 44

Dembinski, H. & et al., P. O. 2020

Disney, M. J. 1976, Nature, 263, 573

D'Onofrio, M., Fasano, G., Varela, J., et al. 2008, ApJ, 685, 875

D'Onofrio, M., Marziani, P., & Chiosi, C. 2021, FA&SS, 8, 157

Dressler, A. 1980, ApJ, 236, 351

Drew, J. E., Gonzalez-Solares, E., Greimel, R., et al. 2014, MNRAS, 440, 2036

Drinkwater, M. J., Gregg, M. D., Hilker, M., et al. 2003, Nature, 423, 519

Duc, P. A., Braine, J., Lisenfeld, U., Brinks, E., & Boquien, M. 2007, A&A, 475, 187

Duc, P.-A., Paudel, S., McDermid, R. M., et al. 2014, MNRAS, 440, 1458

Edge, A., Sutherland, W., Kuijken, K., et al. 2013, The Messenger, 154, 32

Einasto, J. 1965, Trudy Astrof. Inst. Alma-Ata, 5, 87

Emsellem, E., van der Burg, R. F. J., Fensch, J., et al. 2019, A&A, 625, A76

Fattahi, A., Navarro, J. F., & Frenk, C. S. 2020, MNRAS, 493, 2596

Fensch, J., van der Burg, R. F. J., Jeřábková, T., et al. 2019, A&A, 625, A77

Ferrarese, L., Côté, P., Cuillandre, J.-C., et al. 2012, ApJS, 200, 4

Ferrarese, L., Côté, P., MacArthur, L. A., et al. 2020, ApJ, 890, 128

Forbes, D. A., Dullo, B. T., Gannon, J., et al. 2020, MNRAS, 494, 5293

Forbes, D. A., Gannon, J., Couch, W. J., et al. 2019, A&A, 626, A66

Fukazawa, Y., Ohashi, T., Fabian, A. C., et al. 1994, PASJ, 46, L55

Fukushima, K., Kobayashi, S. B., & Matsushita, K. 2022, MNRAS, 514, 4222

Furusho, T., Yamasaki, N. Y., Ohashi, T., et al. 2001, PASJ, 53, 421

Grado, A., Capaccioli, M., Limatola, L., & Getman, F. 2012, Mem. Soc. Ast. It. Sup., 19, 362

Gunn, J. E. & Gott, J. Richard, I. 1972, ApJ, 176, 1

Haigh, C., Chamba, N., Venhola, A., et al. 2021, A&A, 645, A107

Hammer, D., Verdoes Kleijn, G., Hoyos, C., et al. 2010, ApJS, 191, 143

Hamraz, E., Peletier, R. F., Khosroshahi, H. G., et al. 2019, A&A, 625, A94

Harris, C. R., Millman, K. J., van der Walt, S. J., et al. 2020, Nature, 585, 357

Ikebe, Y., Makishima, K., Fukazawa, Y., et al. 1999, ApJ, 525, 58

Impey, C. & Bothun, G. 1997, ARA&A, 35, 267

Iodice, E., Cantiello, M., Hilker, M., et al. 2020a, A&A, 642, A48

Iodice, E., Capaccioli, M., Grado, A., et al. 2016, ApJ, 820, 42

Iodice, E., Spavone, M., Capaccioli, M., et al. 2021a, The Messenger, 183, 25

Iodice, E., Spavone, M., Cattapan, A., et al. 2020b, A&A, 635, A3

Iodice, E., Spavone, M., Raj, M. A., et al. 2021b, A&A, in press (arXiv:2102.04950)

Ivezić, Ž., Kahn, S. M., Tyson, J. A., et al. 2019, ApJ, 873, 111

James, F. & Roos, M. 1975, Comput. Phys. Commun., 10, 343

Janssens, S., Abraham, R., Brodie, J., et al. 2017, ApJ, 839, L17

Janz, J., Laurikainen, E., Lisker, T., et al. 2014, ApJ, 786, 105

Jedrzejewski, R. I. 1987, MNRAS, 226, 747

Kadowaki, J., Zaritsky, D., Donnerstein, R. L., et al. 2021, ApJ, 923, 257

Koch, A., Burkert, A., Rich, R. M., et al. 2012, ApJ, 755, L13

Koda, J., Yagi, M., Yamanoi, H., & Komiyama, Y. 2015, ApJ, 807, L2

Kormendy, J. 1977, ApJ, 218, 333

Kostov, A. & Bonev, T. 2018, Bulg. Astron., 28, 3

Kuijken, K. 2011, The Messenger, 146, 8

Kuijken, K., Bender, R., Cappellaro, E., et al. 2002, The Messenger, 110, 15

Kuijken, K., Heymans, C., Dvornik, A., et al. 2019, A&A, 625, A2

La Marca, A., Iodice, E., Cantiello, M., et al. 2022a, A&A, in press (arXiv:2206.07385)

La Marca, A., Peletier, R., Iodice, E., et al. 2022b, A&A, 659, A92

Landolt, A. U. 1992, AJ, 104, 340

Laureijs, R., Gondoin, P., Duvet, L., et al. 2012, in Society of Photo-Optical Instrumentation Engineers Conf. Ser., Vol. 8442, Space Telescopes and Instrumentation 2012: Optical, Infrared, and Millimeter Wave, ed. M. C. Clampin, G. G. Fazio, H. A. MacEwen, & J. Oschmann, Jacobus M. (Society of Photo-Optical Instrumentation Engineers, San Francisco), 84420T

Lee, J. H., Kang, J., Lee, M. G., & Jang, I. S. 2020, ApJ, 894, 75

Lim, S., Côté, P., Peng, E. W., et al. 2020, ApJ, 899, 69

Lisker, T., Grebel, E. K., & Binggeli, B. 2006, AJ, 132, 497

Lucey, J. R., Currie, M. J., & Dickens, R. J. 1986, MNRAS, 221, 453

Mancera Piña, P. E., Aguerri, J. A. L., Peletier, R. F., et al. 2019, MNRAS, 485, 1036

Mancera Piña, P. E., Peletier, R. F., Aguerri, J. A. L., et al. 2018, MNRAS, 481, 4381

Marconi, M., Musella, I., Di Criscienzo, M., et al. 2014, MNRAS, 444, 3809

Martín-Navarro, I., Romanowsky, A. J., Brodie, J. P., et al. 2019, MNRAS, 484, 3425

Mastropietro, C., Moore, B., Mayer, L., et al. 2005, MNRAS, 364, 607

McFarland, J. P., Helmich, E. M., & Valentijn, E. A. 2013a, Exp. Ast., 35, 79

McFarland, J. P., Verdoes-Kleijn, G., Sikkema, G., et al. 2013b, Exp. Ast., 35, 45

McGaugh, S. S. & Bothun, G. D. 1994, AJ, 107, 530

McMahon, R. G., Banerji, M., Gonzalez, E., et al. 2013, The Messenger, 154, 35

Merluzzi, P., Mercurio, A., Haines, C. P., et al. 2010, MNRAS, 402, 753

Misgeld, I., Hilker, M., & Mieske, S. 2009, A&A, 496, 683

Misgeld, I., Mieske, S., & Hilker, M. 2008, A&A, 486, 697

Montes, M., Infante-Sainz, R., Madrigal-Aguado, A., et al. 2020, ApJ, 904, 114

Moore, B., Lake, G., & Katz, N. 1998, ApJ, 495, 139

Muñoz, R. P., Eigenthaler, P., Puzia, T. H., et al. 2015, ApJ, 813, L15

Müller, O. & Jerjen, H. 2020, A&A, 644, A91

Navarro, J. F., Frenk, C. S., & White, S. D. M. 1997, ApJ, 490, 493

Neubert, P. & Protzel, P. 2014, in 2014 22nd International Conference on Pattern Recognition (Institute of Electrical and Electronical Engineers, Piscataway, NJ), 996

Noethe, L. 2002, Progess in Optics, 43, 1

Ostriker, J. P. & Tremaine, S. D. 1975, ApJ, 202, L113

Peletier, R., Iodice, E., Venhola, A., et al. 2020, arXiv e-prints (arXiv:2008.12633)

Pérez-Montaño, L. E., Rodriguez-Gomez, V., Cervantes Sodi, B., et al. 2022, MNRAS, 514, 5840

Pillepich, A., Nelson, D., Hernquist, L., et al. 2018, MNRAS, 475, 648

Popesso, P., Biviano, A., Böhringer, H., & Romaniello, M. 2006, A&A, 445, 29

Ragusa, R., Mirabile, M., Spavone, M., et al. 2022, FA&SS, 9, 852810

Ragusa, R., Spavone, M., Iodice, E., et al. 2021, A&A, 651, A39

Reiprich, T. H. 2001, PhD thesis, Max-Planck-Institute for Extraterrestrial Physics, Garching

Ripepi, V., Cignoni, M., Tosi, M., et al. 2014, MNRAS, 442, 1897

Robotham, A. S. G., Davies, L. J. M., Driver, S. P., et al. 2018, MNRAS, 476, 3137

Rodriguez-Gomez, V., Lotz, J., & Snyder, G. 2022, statmorph: Non-parametric morphological diagnostics of galaxy images, v0.4.0, Astrophysics Source Code Library, ascl:2201.010

Rodriguez-Gomez, V., Snyder, G. F., Lotz, J. M., et al. 2019, MNRAS, 483, 4140

Román, J. & Trujillo, I. 2017a, MNRAS, 468, 703

Román, J. & Trujillo, I. 2017b, MNRAS, 468, 4039

Ruiz-Lara, T., Beasley, M. A., Falcón-Barroso, J., et al. 2018, MNRAS, 478, 2034

Sales, L. V., Navarro, J. F., Peñafiel, L., et al. 2020, MNRAS, 494, 1848

Sandage, A. & Binggeli, B. 1984, AJ, 89, 919

Schipani, P., Brescia, M., Marty, L., & Perrotta, F. 2006, Mem. Soc. Ast. It. Sup., 9, 469

Schipani, P., Farinato, J., Arcidiacono, C., et al. 2010, in Society of Photo-Optical Instrumentation Engineers Conf. Ser., Vol. 7739, Modern Technologies in Space- and Ground-based Telescopes and Instrumentation, ed. E. Atad-Ettedgui & D. Lemke (Society of Photo-Optical Instrumentation Engineers, San Francisco), 773948

Schipani, P., Noethe, L., Arcidiacono, C., et al. 2012, J. Opt. Soc. Am., 29, 1359

Schlafly, E. F. & Finkbeiner, D. P. 2011, ApJ, 737, 103

Schombert, J. M. & Bothun, G. D. 1988, AJ, 95, 1389

Shanks, T., Belokurov, V., Chehade, B., et al. 2013, The Messenger, 154, 38

Skrutskie, M. F., Cutri, R. M., Stiening, R., et al. 2006, AJ, 131, 1163

Smith, R., Sánchez-Janssen, R., Beasley, M. A., et al. 2015, MNRAS, 454, 2502

Spavone, M., Iodice, E., Capaccioli, M., et al. 2018, ApJ, 864, 149

Spavone, M., Iodice, E., van de Ven, G., et al. 2020, A&A, 639, A14

Sutherland, W., Emerson, J., Dalton, G., et al. 2015, A&A, 575, A25

Sérsic, J. L. 1968, Atlas de Galaxias Australes (Observatorio Astronomico Córdoba, Córdoba)

Teeninga, P., Moschini, U., Trager, S. C., & Wilkinson, M. H. 2015, in International Symposium on Mathematical Morphology and Its Applications to Signal and Image Processing (Springer, Heidelberg), 157

Tremmel, M., Quinn, T. R., Ricarte, A., et al. 2019, MNRAS, 483, 3336

Tremmel, M., Wright, A. C., Brooks, A. M., et al. 2020, MNRAS, 497, 2786

Trujillo, I., Rom'an, J., Filho, M., & Almeida, J. S. 2017, AJ, 836

Tully, R. B., Courtois, H. M., & Sorce, J. G. 2016, AJ, 152, 50

Valentijn, E. A. & Kuijken, K. 2004, in Toward an International Virtual Observatory, ed. P. J. Quinn & K. M. Górski (Springer, Heidelberg), 19

van der Burg, R. F. J. 2014, PhD thesis, Leiden Observatory

van der Burg, R. F. J., Hoekstra, H., Muzzin, A., et al. 2017, A&A, 607, A79

van der Burg, R. F. J., Muzzin, A., & Hoekstra, H. 2016, A&A, 590, A20

van der Walt, S., Schönberger, J. L., Nunez-Iglesias, J., et al. 2014, PeerJ, 2, e453

van Dokkum, P. G., Romanowsky, A. J., Abraham, R., et al. 2015, ApJ, 804, L26

Vandame, B. 2001, in Mining the Sky, ed. A. J. Banday, S. Zaroubi, & M. Bartelmann (Springer, Garching), 595

Venhola, A., Peletier, R., Laurikainen, E., et al. 2018, A&A, 620, A165

Venhola, A., Peletier, R., Laurikainen, E., et al. 2019, A&A, 625, A143

Venhola, A., Peletier, R. F., Salo, H., et al. 2022, A&A, 662, A43

Verdoes Kleijn, G. A., Kuijken, K. H., Valentijn, E. A., et al. 2013, Exp. Ast., 35, 103

Virtanen, P., Gommers, R., Oliphant, T. E., et al. 2020, Nature Methods, 17, 261

Yi, Z., Li, J., Du, W., et al. 2022, MNRAS, 513, 3972

Appendix A

Images and properties of the sample LSB galaxies

The images and photometric properties of the sample LSB galaxies that I successfully analyse in this thesis are reported in this appendix. All the images of the sample LSB galaxies are 500×500 pixel (corresponding to 1.7×1.7 arcmin^2 and 18×18 kpc^2) thumbnails of the reduced g'-band VEGAS image. I add $0.8\,\mathrm{ADU\,pix}^{-1}$ for displaying purposes. The colorbar is the same of Fig. 4.1.

I list the coordinates RA and DEC (J2000.0), absolute magnitude in r' -band $M_{r,0}$, color $(g'-r')_0$, total absolute magnitude in g'-band $M_{g,\mathrm{tot}}$, central and effective surface brightness in g' band $\mu_{g,0}$ and $\mu_{g,e}$, respectively, effective radius R_e, and Sérsic index n of the sample LSB galaxies in Table A. The column A/V of the table tells if the detection method is based on the automatic algorithm (A) or visual inspection (V). I compute $M_{g,\mathrm{tot}}$ with the growth curve (Sec. 3.4) and $M_{r,0}$ with aperture photometry (Sec. 3.2).

name	RA [J2000.0]	DEC [J2000.0]	A/V	$M_{r,0}$ [mag]	$(g'-r')_0$ [mag]	$M_{g,\text{tot}}$ [mag]	$\mu_{g,e}$ [mag arcsec^{-2}]	$\mu_{g,0}$ [mag arcsec^{-2}]	R_e [kpc]	n
LSB1	192.11865	-41.12792	A	-12.65 ± 0.01	0.59 ± 0.02	-13.22 ± 0.44	24.67 ± 0.01	23.32 ± 0.01	0.65 ± 0.05	0.78 ± 0.01
LSB2	192.37796	-41.12654	A	-12.69 ± 0.01	0.69 ± 0.02	-12.29 ± 0.22	25.03 ± 0.01	23.64 ± 0.01	0.51 ± 0.04	0.80 ± 0.01
LSB3	191.86936	-41.09078	A	-13.43 ± 0.01	0.71 ± 0.02	-14.38 ± 0.50	24.46 ± 0.01	23.42 ± 0.01	0.79 ± 0.06	0.64 ± 0.01
LSB4	192.30857	-41.08224	A	-12.53 ± 0.01	0.70 ± 0.02	-11.70 ± 1.61	26.43 ± 0.00	25.79 ± 0.00	1.37 ± 0.11	0.44 ± 0.00
LSB5	191.93087	-41.00900	A	-13.26 ± 0.01	0.48 ± 0.02	-14.87 ± 0.31	24.39 ± 0.01	23.35 ± 0.01	1.33 ± 0.10	0.64 ± 0.00
LSB6	192.59832	-41.00924	A	-13.00 ± 0.01	0.58 ± 0.02	-14.03 ± 0.18	25.08 ± 0.01	23.46 ± 0.01	1.11 ± 0.09	0.91 ± 0.00
LSB7	192.18577	-40.98700	A	-13.26 ± 0.01	0.97 ± 0.02	-12.39 ± 0.17	24.22 ± 0.01	23.20 ± 0.01	0.34 ± 0.03	0.63 ± 0.00
LSB8	192.05187	-40.97937	A	-12.69 ± 0.01	0.76 ± 0.02	-13.22 ± 0.31	25.71 ± 0.01	23.59 ± 0.01	1.12 ± 0.09	1.14 ± 0.01
LSB9	192.18052	-40.97697	A	-13.42 ± 0.01	0.82 ± 0.02	-14.82 ± 0.26	24.70 ± 0.01	23.38 ± 0.01	1.23 ± 0.10	0.77 ± 0.00
LSB10	192.53167	-40.97397	A	-13.04 ± 0.01	0.79 ± 0.02	-13.07 ± 0.32	25.11 ± 0.01	23.82 ± 0.01	0.71 ± 0.06	0.75 ± 0.01
LSB11	191.52002	-40.96892	A	-13.23 ± 0.01	0.94 ± 0.02	-12.25 ± 0.18	24.32 ± 0.01	23.63 ± 0.01	0.39 ± 0.03	0.47 ± 0.00
LSB12	191.75402	-40.96770	A	-12.92 ± 0.01	0.84 ± 0.02	-13.87 ± 0.32	24.89 ± 0.02	23.31 ± 0.02	0.53 ± 0.04	0.89 ± 0.01
LSB13	192.26846	-40.96351	A	-12.42 ± 0.01	0.80 ± 0.02	-13.71 ± 0.77	26.63 ± 0.05	23.79 ± 0.05	1.92 ± 0.17	1.47 ± 0.03
LSB14	193.21267	-40.94936	A	-13.33 ± 0.01	0.78 ± 0.02	-13.58 ± 0.99	24.74 ± 0.01	23.49 ± 0.01	0.84 ± 0.07	0.73 ± 0.01
LSB15	191.51540	-40.90119	A	-12.73 ± 0.01	0.59 ± 0.02	-12.63 ± 0.19	24.99 ± 0.01	23.58 ± 0.01	0.54 ± 0.04	0.81 ± 0.00
LSB16	191.93527	-40.89447	A	-12.57 ± 0.01	0.61 ± 0.02	-12.57 ± 0.31	25.07 ± 0.01	23.35 ± 0.01	0.43 ± 0.03	0.95 ± 0.01
LSB17	192.37950	-40.89266	A	-13.02 ± 0.01	0.73 ± 0.02	-12.44 ± 0.23	24.82 ± 0.01	23.46 ± 0.01	0.47 ± 0.04	0.79 ± 0.01
LSB18	192.70316	-40.88150	A	-12.54 ± 0.01	0.65 ± 0.02	-12.37 ± 0.24	25.15 ± 0.02	23.62 ± 0.02	0.49 ± 0.04	0.87 ± 0.01
LSB19	192.08052	-40.87446	A	-13.15 ± 0.01	0.45 ± 0.02	-13.20 ± 0.17	24.49 ± 0.01	23.38 ± 0.01	0.66 ± 0.05	0.67 ± 0.00
UDG1	192.24801	-40.84171	A	-12.37 ± 0.01	0.74 ± 0.02	-14.39 ± 0.50	26.21 ± 0.03	24.08 ± 0.03	1.75 ± 0.14	1.14 ± 0.02
LSB20	192.68142	-40.81209	A	-12.62 ± 0.01	0.45 ± 0.02	-12.18 ± 0.30	24.87 ± 0.02	23.34 ± 0.02	0.48 ± 0.04	0.87 ± 0.01
LSB21	192.68848	-40.72864	A	-13.56 ± 0.01	0.87 ± 0.02	-14.14 ± 0.21	24.70 ± 0.01	23.24 ± 0.01	0.98 ± 0.08	0.83 ± 0.00
LSB22	191.58928	-40.72213	A	-13.16 ± 0.01	0.69 ± 0.02	-14.13 ± 0.19	25.18 ± 0.01	23.49 ± 0.01	1.21 ± 0.09	0.94 ± 0.00
LSB23	191.54630	-40.68713	A	-13.04 ± 0.01	0.74 ± 0.02	-13.54 ± 0.22	25.51 ± 0.01	23.60 ± 0.01	1.29 ± 0.10	1.04 ± 0.01
LSB24	192.52880	-41.76887	A	-12.98 ± 0.01	0.61 ± 0.02	-13.83 ± 0.32	25.02 ± 0.01	23.67 ± 0.01	0.99 ± 0.08	0.78 ± 0.01
LSB25	193.11522	-41.74978	A	-12.97 ± 0.01	0.72 ± 0.02	-14.10 ± 0.17	25.49 ± 0.02	23.46 ± 0.02	1.23 ± 0.10	1.10 ± 0.01
LSB26	192.78144	-41.75074	A	-12.66 ± 0.01	0.39 ± 0.02	-12.34 ± 0.19	24.59 ± 0.01	23.84 ± 0.01	0.44 ± 0.03	0.50 ± 0.01
LSB27	191.58508	-41.72363	A	-11.77 ± 0.01	-0.00 ± 0.02	-13.79 ± 0.27	24.99 ± 0.02	24.33 ± 0.02	1.04 ± 0.08	0.46 ± 0.01
LSB28	193.14229	-41.67940	A	-12.68 ± 0.01	0.43 ± 0.02	-12.59 ± 0.19	24.62 ± 0.01	23.49 ± 0.01	0.52 ± 0.04	0.68 ± 0.01
LSB29	192.55514	-41.66517	A	-12.53 ± 0.01	0.75 ± 0.02	-12.71 ± 0.31	25.59 ± 0.02	24.25 ± 0.02	0.76 ± 0.06	0.77 ± 0.01
LSB30	191.89242	-41.66353	A	-12.72 ± 0.01	0.60 ± 0.02	-12.73 ± 0.18	24.84 ± 0.01	23.62 ± 0.01	0.56 ± 0.04	0.72 ± 0.01
LSB31	191.59107	-41.66164	A	-12.74 ± 0.01	0.74 ± 0.02	-12.90 ± 0.68	25.38 ± 0.03	23.68 ± 0.03	0.73 ± 0.06	0.94 ± 0.01
LSB32	192.52368	-41.63802	A	-13.19 ± 0.01	0.74 ± 0.02	-13.02 ± 0.28	24.68 ± 0.02	23.41 ± 0.02	0.62 ± 0.05	0.74 ± 0.01
LSB33	192.63076	-41.62178	A	-12.75 ± 0.01	0.67 ± 0.02	-13.50 ± 0.31	25.13 ± 0.01	23.79 ± 0.01	0.62 ± 0.05	0.78 ± 0.01

name	RA [J2000.0]	DEC [J2000.0]	A/V	$M_{r,0}$ [mag]	$(g'-r')_0$ [mag]	$M_{g,\mathrm{tot}}$ [mag]	$\mu_{g,e}$ [mag arcsec^{-2}]	$\mu_{g,0}$ [mag arcsec^{-2}]	R_e [kpc]	n
LSB34	192.21893	-41.54018	A	-12.76 ± 0.01	0.77 ± 0.02	-13.76 ± 0.34	25.67 ± 0.02	23.17 ± 0.02	0.89 ± 0.07	1.31 ± 0.01
LSB35	192.35833	-41.52485	A	-12.98 ± 0.01	0.71 ± 0.02	-13.72 ± 0.41	24.99 ± 0.01	23.45 ± 0.01	0.65 ± 0.05	0.87 ± 0.01
LSB36	192.69122	-41.51871	A	-12.73 ± 0.01	0.48 ± 0.02	-12.32 ± 0.23	24.67 ± 0.02	23.67 ± 0.02	0.42 ± 0.03	0.62 ± 0.01
LSB37	191.95054	-41.51058	A	-12.59 ± 0.01	0.46 ± 0.02	-12.53 ± 0.22	24.86 ± 0.01	23.36 ± 0.01	0.50 ± 0.04	0.85 ± 0.01
UDG2	193.04092	-41.47424	A	-12.13 ± 0.01	0.66 ± 0.02	-12.82 ± 0.89	26.72 ± 0.07	24.06 ± 0.07	1.63 ± 0.16	1.39 ± 0.04
LSB38	192.73484	-41.41749	A	-13.21 ± 0.01	0.69 ± 0.02	-14.06 ± 0.26	25.02 ± 0.01	23.33 ± 0.01	0.96 ± 0.08	0.94 ± 0.01
LSB39	192.65294	-41.41406	A	-13.21 ± 0.01	0.72 ± 0.02	-14.47 ± 0.23	25.37 ± 0.02	23.30 ± 0.02	1.42 ± 0.11	1.12 ± 0.01
LSB40	191.85462	-41.40066	A	-12.78 ± 0.01	0.60 ± 0.02	-12.59 ± 0.27	24.44 ± 0.01	23.20 ± 0.01	0.49 ± 0.04	0.73 ± 0.01
LSB41	192.36864	-41.37875	A	-12.76 ± 0.01	0.78 ± 0.02	-13.41 ± 0.32	25.76 ± 0.02	23.79 ± 0.02	1.47 ± 0.12	1.07 ± 0.01
LSB42	192.92184	-41.37458	A	-12.54 ± 0.01	0.72 ± 0.02	-13.42 ± 0.17	26.04 ± 0.01	23.70 ± 0.01	1.17 ± 0.09	1.24 ± 0.01
LSB43	192.39187	-41.37682	A	-12.59 ± 0.01	0.75 ± 0.02	-13.44 ± 0.27	25.52 ± 0.01	24.21 ± 0.01	0.95 ± 0.07	0.76 ± 0.01
LSB44	191.59425	-41.37007	A	-12.80 ± 0.01	0.52 ± 0.02	-12.86 ± 0.49	24.27 ± 0.01	23.51 ± 0.01	0.38 ± 0.03	0.50 ± 0.00
LSB45	192.07936	-41.35818	A	-12.42 ± 0.01	0.71 ± 0.02	-12.58 ± 0.26	25.42 ± 0.00	24.88 ± 0.00	0.65 ± 0.05	0.40 ± 0.00
LSB46	192.01281	-41.32301	A	-12.36 ± 0.01	0.77 ± 0.02	-12.52 ± 0.34	25.91 ± 0.02	24.65 ± 0.02	0.86 ± 0.07	0.74 ± 0.01
LSB47	192.00094	-41.32079	A	-12.72 ± 0.01	0.74 ± 0.02	-12.81 ± 0.36	25.05 ± 0.01	23.98 ± 0.01	0.67 ± 0.05	0.65 ± 0.01
LSB48	191.51248	-41.30586	A	-12.94 ± 0.01	0.66 ± 0.02	-13.62 ± 0.51	25.39 ± 0.02	23.45 ± 0.02	0.96 ± 0.08	1.05 ± 0.01
LSB49	192.57022	-41.30728	A	-12.70 ± 0.01	0.65 ± 0.02	-13.51 ± 0.23	25.13 ± 0.01	24.00 ± 0.01	0.88 ± 0.07	0.68 ± 0.00
LSB50	192.05642	-41.30387	A	-12.68 ± 0.01	0.71 ± 0.02	-13.94 ± 0.83	26.11 ± 0.03	23.51 ± 0.03	1.58 ± 0.13	1.36 ± 0.02
LSB51	191.50157	-41.28845	A	-13.08 ± 0.01	0.72 ± 0.02	-13.90 ± 0.17	25.33 ± 0.01	23.32 ± 0.01	0.95 ± 0.07	1.09 ± 0.00
LSB52	192.41161	-41.27775	A	-12.59 ± 0.01	0.73 ± 0.02	-12.39 ± 0.28	24.91 ± 0.01	23.92 ± 0.01	0.51 ± 0.04	0.61 ± 0.01
LSB53	192.37671	-41.26347	A	-12.70 ± 0.01	0.47 ± 0.02	-12.37 ± 0.20	24.29 ± 0.01	23.33 ± 0.01	0.37 ± 0.03	0.60 ± 0.00
LSB54	192.95565	-41.25592	A	-13.18 ± 0.01	0.70 ± 0.02	-13.29 ± 0.23	24.70 ± 0.01	23.51 ± 0.01	0.63 ± 0.05	0.70 ± 0.01
LSB55	192.62090	-41.24591	A	-12.78 ± 0.01	0.70 ± 0.02	-13.03 ± 0.17	25.55 ± 0.00	23.52 ± 0.00	0.82 ± 0.06	1.10 ± 0.00
LSB56	192.57027	-41.24269	A	-12.42 ± 0.01	0.75 ± 0.02	-13.63 ± 0.93	26.45 ± 0.03	23.67 ± 0.03	1.51 ± 0.12	1.45 ± 0.02
LSB57	192.45296	-41.23848	A	-13.24 ± 0.01	0.77 ± 0.02	-13.97 ± 0.17	25.15 ± 0.01	23.32 ± 0.01	0.94 ± 0.07	1.00 ± 0.00
LSB58	192.28873	-41.23426	A	-12.66 ± 0.01	0.78 ± 0.02	-14.38 ± 0.17	25.67 ± 0.01	23.86 ± 0.01	0.83 ± 0.07	0.99 ± 0.00
LSB59	192.36461	-41.20913	A	-12.88 ± 0.01	0.76 ± 0.02	-12.85 ± 1.10	24.71 ± 0.02	23.54 ± 0.02	0.42 ± 0.03	0.70 ± 0.01
LSB60	191.92657	-41.20832	A	-13.33 ± 0.01	0.73 ± 0.02	-13.78 ± 0.23	24.88 ± 0.01	23.47 ± 0.01	0.86 ± 0.07	0.81 ± 0.00
LSB61	192.38791	-41.20297	A	-12.72 ± 0.01	0.64 ± 0.02	-12.40 ± 0.19	24.48 ± 0.00	23.38 ± 0.00	0.57 ± 0.04	0.66 ± 0.00
LSB62	193.09477	-41.17935	A	-13.47 ± 0.01	0.79 ± 0.02	-13.89 ± 0.50	24.59 ± 0.01	23.35 ± 0.01	0.76 ± 0.06	0.73 ± 0.00
LSB63	191.54608	-41.17630	A	-13.50 ± 0.01	0.52 ± 0.02	-15.14 ± 0.25	24.68 ± 0.01	23.22 ± 0.01	1.62 ± 0.13	0.84 ± 0.00
LSB64	192.62336	-41.16736	A	-12.71 ± 0.01	0.73 ± 0.02	-13.31 ± 0.25	25.60 ± 0.01	23.74 ± 0.01	0.96 ± 0.08	1.02 ± 0.01
LSB65	191.59062	-41.16459	A	-13.22 ± 0.01	0.77 ± 0.02	-12.74 ± 0.18	24.92 ± 0.01	23.52 ± 0.01	0.56 ± 0.04	0.81 ± 0.00
LSB66	192.45160	-41.15758	A	-12.76 ± 0.01	0.74 ± 0.02	-12.75 ± 0.17	25.06 ± 0.00	23.94 ± 0.00	0.55 ± 0.04	0.68 ± 0.00

name	RA [J2000.0]	DEC [J2000.0]	A/V	$M_{r,0}$ [mag]	$(g'-r')_0$ [mag]	$M_{g,\mathrm{tot}}$ [mag]	$\mu_{g,e}$ [mag arcsec^{-2}]	$\mu_{g,0}$ [mag arcsec^{-2}]	R_e [kpc]	n
LSB67	191.66689	-41.12944	A	-12.90 ± 0.01	0.66 ± 0.02	-14.05 ± 0.22	25.30 ± 0.00	23.40 ± 0.00	0.77 ± 0.06	1.04 ± 0.00
LSB68	191.75731	-41.12996	A	-13.23 ± 0.01	0.94 ± 0.02	-13.02 ± 0.58	24.76 ± 0.01	23.24 ± 0.01	0.64 ± 0.05	0.86 ± 0.00
LSB69	193.10062	-41.36408	V	-11.88 ± 0.01	0.81 ± 0.02	-11.61 ± 0.45	25.50 ± 0.03	24.47 ± 0.03	0.41 ± 0.03	0.63 ± 0.01
LSB70	192.43622	-41.65542	V	-11.68 ± 0.01	0.52 ± 0.02	-11.46 ± 0.26	25.08 ± 0.01	24.20 ± 0.01	0.36 ± 0.03	0.56 ± 0.01
LSB71	192.36653	-41.61987	V	-12.20 ± 0.01	0.81 ± 0.02	-12.54 ± 0.23	25.51 ± 0.02	24.46 ± 0.02	0.57 ± 0.05	0.64 ± 0.01
LSB72	192.29485	-41.49343	V	-11.88 ± 0.01	0.63 ± 0.02	-11.91 ± 0.34	25.59 ± 0.01	24.26 ± 0.01	0.45 ± 0.04	0.77 ± 0.01
LSB73	192.34174	-41.47286	V	-12.58 ± 0.01	0.73 ± 0.02	-14.01 ± 0.21	25.31 ± 0.01	23.65 ± 0.01	0.96 ± 0.08	0.93 ± 0.01
LSB74	192.68152	-41.39811	V	-12.00 ± 0.01	0.44 ± 0.02	-11.72 ± 0.19	24.55 ± 0.01	23.64 ± 0.01	0.30 ± 0.02	0.57 ± 0.00
LSB75	192.64496	-41.42249	V	-11.67 ± 0.01	0.67 ± 0.02	-12.21 ± 0.22	25.87 ± 0.00	25.32 ± 0.00	0.65 ± 0.05	0.40 ± 0.00
LSB76	193.04793	-41.63500	V	-13.43 ± 0.01	0.74 ± 0.02	-14.40 ± 0.17	25.48 ± 0.00	22.55 ± 0.00	1.57 ± 0.12	1.51 ± 0.00
LSB77	193.03538	-41.64402	V	-11.94 ± 0.01	0.62 ± 0.02	-12.17 ± 0.51	26.37 ± 0.01	24.51 ± 0.01	0.98 ± 0.08	1.02 ± 0.01
LSB78	192.95030	-41.51399	V	-12.00 ± 0.01	0.68 ± 0.02	-12.00 ± 0.21	25.80 ± 0.01	24.53 ± 0.01	0.58 ± 0.05	0.74 ± 0.00
LSB79	193.01492	-41.50304	V	-12.07 ± 0.01	0.73 ± 0.02	-12.94 ± 0.63	26.16 ± 0.02	24.66 ± 0.02	1.16 ± 0.09	0.85 ± 0.01
LSB80	192.81312	-41.74819	V	-12.44 ± 0.01	0.81 ± 0.02	-13.24 ± 0.22	26.31 ± 0.02	23.77 ± 0.02	1.43 ± 0.11	1.33 ± 0.01
UDG3	192.87263	-41.64295	V	-12.56 ± 0.01	0.71 ± 0.02	-15.00 ± 0.20	25.84 ± 0.02	24.23 ± 0.02	1.52 ± 0.12	0.90 ± 0.01
LSB81	193.14641	-41.28991	V	-13.33 ± 0.01	0.40 ± 0.02	-15.30 ± 0.18	25.19 ± 0.01	23.04 ± 0.01	2.07 ± 0.16	1.15 ± 0.00
LSB82	193.17263	-41.33079	V	-13.59 ± 0.01	0.90 ± 0.02	-13.75 ± 0.18	24.54 ± 0.01	23.25 ± 0.01	0.79 ± 0.06	0.75 ± 0.00
LSB83	193.19836	-41.37494	V	-13.58 ± 0.01	0.81 ± 0.02	-14.70 ± 0.22	24.71 ± 0.01	23.02 ± 0.01	1.04 ± 0.08	0.94 ± 0.00
LSB84	193.20347	-41.38283	V	-13.54 ± 0.01	0.50 ± 0.02	-14.95 ± 0.19	24.21 ± 0.01	22.94 ± 0.01	1.22 ± 0.10	0.74 ± 0.00
LSB85	192.82803	-41.09737	V	-13.89 ± 0.01	0.85 ± 0.02	-15.60 ± 0.22	24.93 ± 0.01	22.30 ± 0.01	1.21 ± 0.10	1.38 ± 0.00
LSB86	192.81408	-41.12817	V	-14.11 ± 0.01	0.78 ± 0.02	-15.14 ± 0.17	26.03 ± 0.00	23.38 ± 0.00	3.83 ± 0.30	1.38 ± 0.00
LSB87	192.79109	-41.15935	V	-12.38 ± 0.01	0.85 ± 0.02	-12.75 ± 0.27	25.45 ± 0.01	24.25 ± 0.01	0.68 ± 0.05	0.71 ± 0.00
LSB88	192.59128	-40.92846	V	-13.43 ± 0.01	0.48 ± 0.02	-13.30 ± 0.19	24.09 ± 0.00	23.16 ± 0.00	0.56 ± 0.04	0.58 ± 0.00
LSB89	192.56076	-41.08002	V	-12.87 ± 0.01	0.85 ± 0.02	-13.93 ± 0.45	26.06 ± 0.02	22.85 ± 0.02	1.38 ± 0.11	1.64 ± 0.01
LSB90	192.50798	-41.08096	V	-13.24 ± 0.01	0.85 ± 0.02	-14.51 ± 0.45	25.32 ± 0.01	23.37 ± 0.01	1.12 ± 0.09	1.06 ± 0.01
LSB91	192.40692	-41.16573	V	-13.33 ± 0.01	0.98 ± 0.02	-12.52 ± 0.21	24.27 ± 0.01	23.13 ± 0.01	0.53 ± 0.04	0.68 ± 0.00
LSB92	192.38063	-41.22765	V	-13.39 ± 0.01	0.42 ± 0.02	-14.16 ± 0.31	24.88 ± 0.01	23.15 ± 0.01	1.54 ± 0.12	0.95 ± 0.00
LSB93	192.44402	-41.36867	V	-13.59 ± 0.01	0.78 ± 0.02	-14.64 ± 0.17	25.13 ± 0.01	22.43 ± 0.01	1.12 ± 0.09	1.41 ± 0.00
LSB94	192.00843	-41.91060	V	-13.43 ± 0.01	0.82 ± 0.02	-13.70 ± 0.17	24.47 ± 0.00	23.37 ± 0.00	0.68 ± 0.05	0.67 ± 0.00
LSB95	191.91703	-41.72912	V	-12.02 ± 0.01	0.78 ± 0.02	-13.92 ± 0.22	25.79 ± 0.02	24.36 ± 0.02	1.41 ± 0.11	0.82 ± 0.01
LSB96	191.97760	-41.64146	V	-12.37 ± 0.01	0.69 ± 0.02	-14.53 ± 0.26	26.16 ± 0.02	23.88 ± 0.02	1.10 ± 0.09	1.21 ± 0.01
LSB97	191.78261	-41.53311	V	-13.45 ± 0.01	0.75 ± 0.02	-14.54 ± 0.66	25.19 ± 0.02	22.99 ± 0.02	1.19 ± 0.09	1.17 ± 0.01
LSB98	191.75132	-41.54045	V	-13.14 ± 0.01	0.65 ± 0.02	-14.29 ± 0.24	25.17 ± 0.01	23.11 ± 0.01	1.20 ± 0.09	1.11 ± 0.00
LSB99	191.75197	-41.92265	V	-13.10 ± 0.01	0.65 ± 0.02	-14.24 ± 0.18	25.42 ± 0.01	22.93 ± 0.01	1.28 ± 0.10	1.31 ± 0.00

| name	RA [J2000.0]	DEC [J2000.0]	A/V	$M_{r,0}$ [mag]	$(g'-r')_0$ [mag]	$M_{g,tot}$ [mag]	$\mu_{g,e}$ [mag arcsec^{-2}]	$\mu_{g,0}$ [mag arcsec^{-2}]	R_e [kpc]	n
LSB100	192.50209	-41.62530	V	-9.51 ± 0.11	0.76 ± 0.02	-15.04 ± 0.17	25.23 ± 0.01	23.52 ± 0.01	1.99 ± 0.16	0.95 ± 0.00
LSB101	191.71882	-41.44783	V	-13.28 ± 0.01	0.66 ± 0.02	-14.41 ± 1.45	25.26 ± 0.02	22.58 ± 0.02	2.11 ± 0.17	1.39 ± 0.01
LSB102	191.54587	-41.51706	V	-13.18 ± 0.01	0.62 ± 0.02	-14.33 ± 0.20	24.78 ± 0.01	23.42 ± 0.01	1.09 ± 0.09	0.79 ± 0.00
LSB103	191.63836	-41.62658	V	-13.39 ± 0.01	0.74 ± 0.02	-15.17 ± 0.18	25.10 ± 0.00	21.94 ± 0.00	1.33 ± 0.10	1.62 ± 0.00
LSB104	191.52919	-41.69554	V	-12.84 ± 0.01	0.55 ± 0.02	-14.02 ± 0.63	25.09 ± 0.02	23.35 ± 0.02	1.24 ± 0.10	0.96 ± 0.01
LSB105	192.15396	-40.71123	V	-14.15 ± 0.01	1.02 ± 0.02	-13.70 ± 0.19	24.25 ± 0.01	23.17 ± 0.01	0.67 ± 0.05	0.65 ± 0.00
LSB106	192.00826	-40.73893	V	-13.48 ± 0.01	0.69 ± 0.02	-14.66 ± 0.17	24.93 ± 0.01	23.17 ± 0.01	1.08 ± 0.08	0.97 ± 0.00
LSB107	192.14653	-41.00977	V	-12.95 ± 0.01	0.89 ± 0.02	-14.19 ± 0.75	26.00 ± 0.03	23.67 ± 0.03	2.00 ± 0.17	1.23 ± 0.02
LSB108	192.13069	-41.13041	V	-13.27 ± 0.01	0.85 ± 0.02	-12.96 ± 0.28	24.85 ± 0.01	23.65 ± 0.01	0.52 ± 0.04	0.71 ± 0.00
LSB109	191.96458	-41.18181	V	-13.08 ± 0.01	0.78 ± 0.02	-14.77 ± 0.20	25.97 ± 0.01	22.81 ± 0.01	1.82 ± 0.14	1.62 ± 0.01
LSB110	191.88454	-40.87023	V	-13.78 ± 0.01	0.53 ± 0.02	-14.07 ± 0.24	23.94 ± 0.00	23.22 ± 0.00	0.96 ± 0.08	0.48 ± 0.00
LSB111	191.74188	-40.83832	V	-13.22 ± 0.01	0.70 ± 0.02	-14.11 ± 0.18	25.33 ± 0.00	23.29 ± 0.00	1.24 ± 0.10	1.10 ± 0.00
LSB112	191.66983	-40.90769	V	-13.09 ± 0.01	0.79 ± 0.02	-14.25 ± 0.17	24.69 ± 0.00	23.02 ± 0.00	0.79 ± 0.06	0.93 ± 0.00
LSB113	191.52866	-41.12530	V	-13.18 ± 0.01	0.83 ± 0.02	-15.63 ± 0.20	26.04 ± 0.00	23.14 ± 0.00	2.46 ± 0.19	1.50 ± 0.00
LSB114	191.56503	-40.64655	V	-13.04 ± 0.01	0.72 ± 0.02	-15.13 ± 0.26	26.07 ± 0.00	23.40 ± 0.00	2.41 ± 0.19	1.39 ± 0.00
UDG4	191.81174	-41.15836	V	-11.75 ± 0.01	0.64 ± 0.02	-13.11 ± 0.27	26.67 ± 0.01	24.87 ± 0.01	2.21 ± 0.17	0.99 ± 0.01
LSB115	193.08426	-41.55913	V	-12.16 ± 0.01	0.62 ± 0.02	-12.46 ± 0.29	25.68 ± 0.01	24.43 ± 0.01	0.69 ± 0.05	0.74 ± 0.01
LSB116	193.17472	-41.80785	V	-13.38 ± 0.01	0.80 ± 0.02	-14.99 ± 0.26	24.84 ± 0.01	23.33 ± 0.01	1.48 ± 0.12	0.86 ± 0.00
LSB117	192.12958	-40.87778	V	-13.14 ± 0.01	0.85 ± 0.02	-13.56 ± 0.22	24.80 ± 0.01	23.21 ± 0.01	0.61 ± 0.05	0.89 ± 0.00
UDG5	192.00305	-41.11000	V	-11.26 ± 0.01	0.61 ± 0.02	-13.18 ± 0.34	27.34 ± 0.02	24.18 ± 0.02	2.03 ± 0.17	1.62 ± 0.01
LSB118	191.97593	-41.06237	V	-13.86 ± 0.01	0.77 ± 0.02	-15.56 ± 2.08	25.27 ± 0.22	22.42 ± 0.22	2.12 ± 0.43	1.48 ± 0.12
LSB119	192.34463	-41.25507	V	-13.92 ± 0.01	0.80 ± 0.02	-14.95 ± 0.22	24.05 ± 0.00	22.47 ± 0.00	0.83 ± 0.07	0.89 ± 0.00
LSB120	192.00725	-41.53191	V	-11.93 ± 0.01	0.67 ± 0.02	-12.96 ± 0.19	25.90 ± 0.02	24.42 ± 0.02	0.99 ± 0.08	0.84 ± 0.01
LSB121	192.57524	-41.42979	V	-13.44 ± 0.01	0.79 ± 0.02	-14.18 ± 0.62	24.79 ± 0.01	22.13 ± 0.01	0.69 ± 0.05	1.39 ± 0.00
LSB122	192.62380	-41.53557	V	-13.58 ± 0.01	0.73 ± 0.02	-15.62 ± 0.20	24.84 ± 0.01	22.86 ± 0.01	1.65 ± 0.13	1.07 ± 0.00
LSB123	192.72114	-41.60603	V	-13.58 ± 0.01	0.87 ± 0.02	-15.99 ± 0.20	26.17 ± 0.01	21.95 ± 0.01	3.80 ± 0.30	2.11 ± 0.01
LSB124	193.25738	-41.64646	V	-12.71 ± 0.01	0.94 ± 0.02	-12.03 ± 0.20	24.36 ± 0.01	23.66 ± 0.01	0.31 ± 0.02	0.47 ± 0.00
LSB125	192.79836	-40.62430	V	-13.17 ± 0.01	0.77 ± 0.02	-13.88 ± 0.34	25.22 ± 0.01	23.23 ± 0.01	1.26 ± 0.10	1.08 ± 0.00
LSB126	193.12011	-41.70893	V	-12.21 ± 0.01	0.71 ± 0.02	-12.31 ± 0.27	25.15 ± 0.01	24.28 ± 0.01	0.56 ± 0.04	0.55 ± 0.00
LSB127	193.21798	-41.84367	V	-11.06 ± 0.01	0.81 ± 0.02	-14.75 ± 0.17	24.15 ± 0.01	23.09 ± 0.01	0.59 ± 0.05	0.64 ± 0.00
LSB128	193.19640	-41.94973	V	-12.28 ± 0.01	0.75 ± 0.02	-11.55 ± 0.17	25.30 ± 0.01	23.72 ± 0.01	0.58 ± 0.05	0.89 ± 0.00
LSB129	193.24142	-42.05335	V	-12.03 ± 0.01	0.96 ± 0.02	-13.81 ± 0.20	21.50 ± 0.00	19.47 ± 0.00	0.18 ± 0.01	1.10 ± 0.00
LSB130	192.31857	-41.78454	V	-11.80 ± 0.01	0.62 ± 0.02	-12.04 ± 0.25	26.51 ± 0.02	24.66 ± 0.02	1.00 ± 0.08	1.01 ± 0.01
LSB131	192.36967	-41.66084	V	-12.09 ± 0.01	0.69 ± 0.02	-12.86 ± 0.17	26.08 ± 0.01	24.35 ± 0.01	0.75 ± 0.06	0.96 ± 0.00
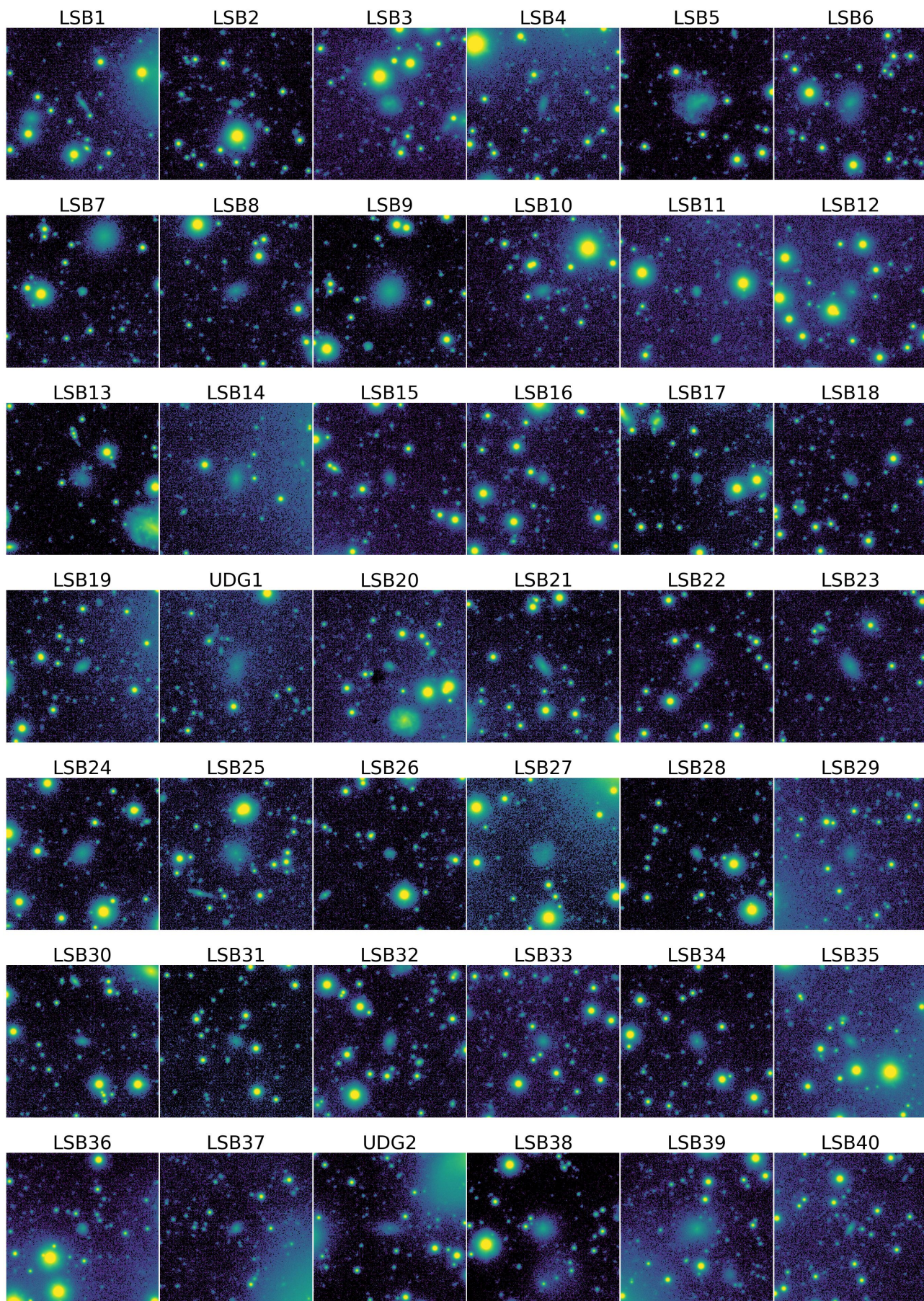
Figure A.1: Sample LSB galaxies. The FoV of each image is $1.7 \times 1.7 \, \text{arcmin}^2$ ($18 \times 18 \, \text{kpc}^2$) with north up and east left.
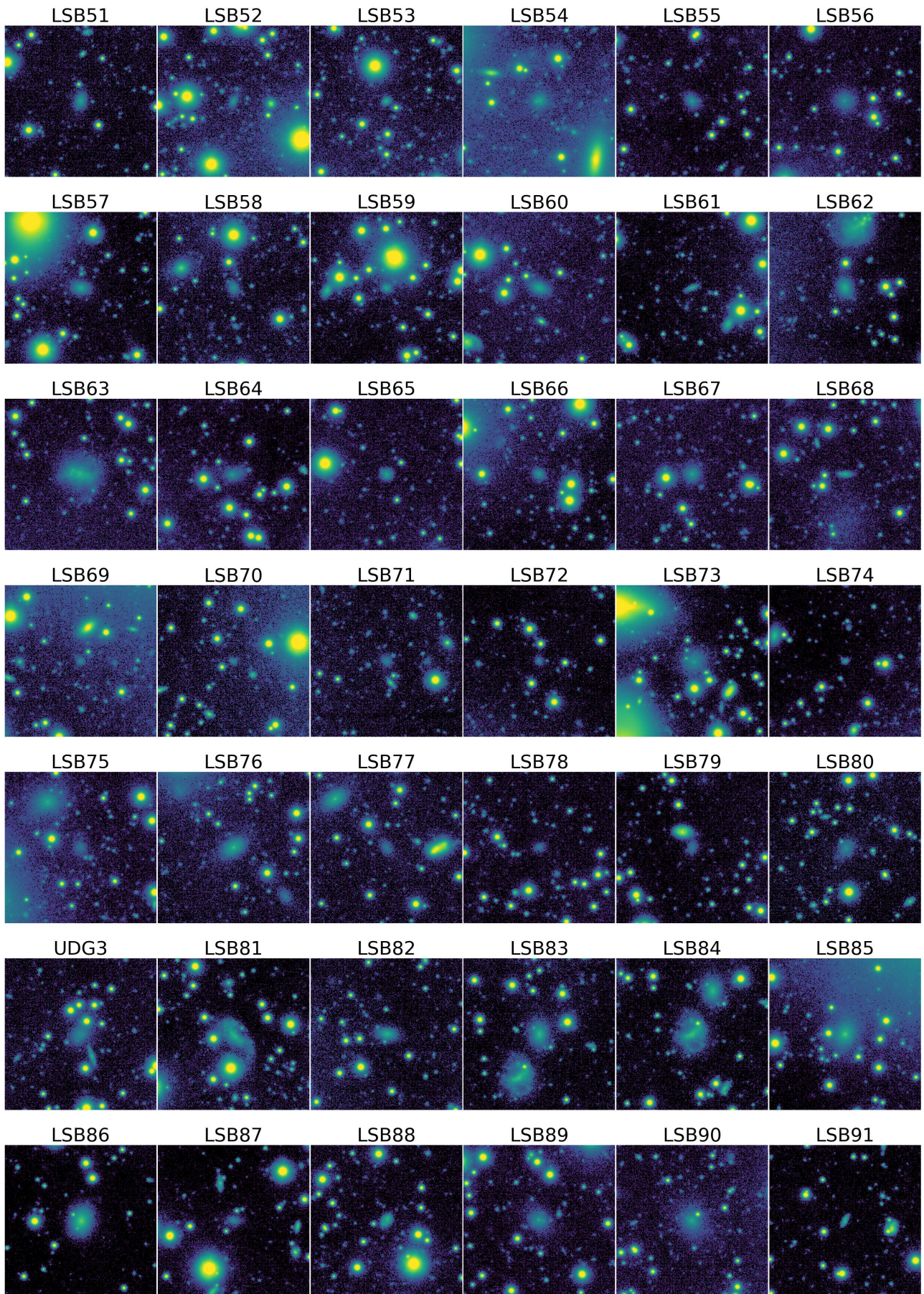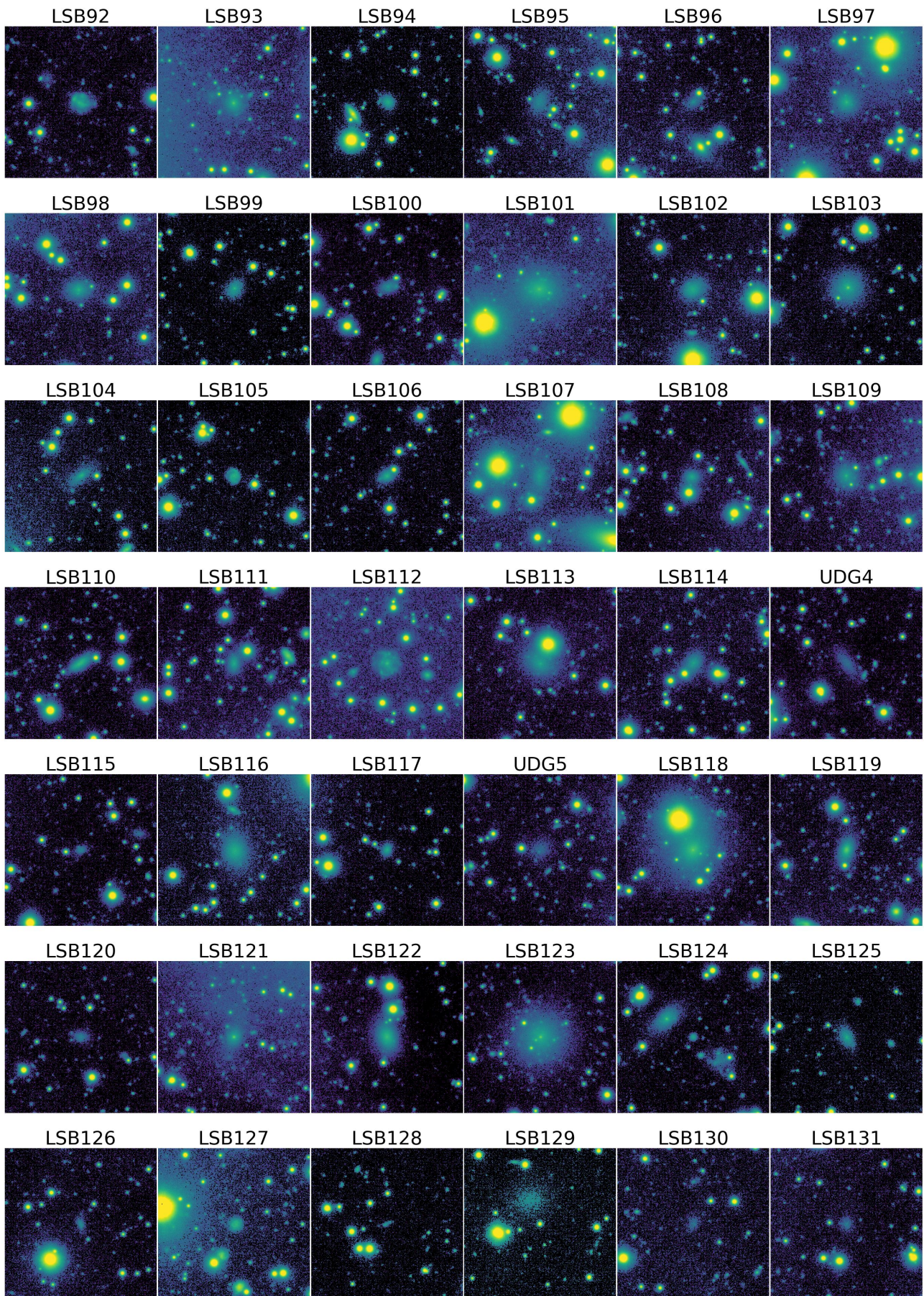
FIGURE A.1: (continued)

LSB92   LSB93   LSB94   LSB95   LSB96   LSB97

LSB98   LSB99   LSB100   LSB101   LSB102   LSB103

LSB104   LSB105   LSB106   LSB107   LSB108   LSB109

LSB110   LSB111   LSB112   LSB113   LSB114   UDG4

LSB115   LSB116   LSB117   UDG5   LSB118   LSB119

LSB120   LSB121   LSB122   LSB123   LSB124   LSB125

LSB126   LSB127   LSB128   LSB129   LSB130   LSB131

FIGURE A.1: (continued)

66